AGU ADVANCING EARTH AND SPACE SCIENCE

Reviews of Geophysics

REVIEW ARTICLE
10.1029/2022RG000792

Key Points:

- International Reference Ionosphere (IRI): Scientific background and mathematical formalism
- Description of the latest version of the model: IRI-2022
- IRI Achievements and plans for the future

Correspondence to:

D. Bilitza,
dbilitza@gmu.edu

Citation:

Bilitza, D., Pezzopane, M., Truhlik, V., Altadill, D., Reinisch, B. W., & Pignalberi, A. (2022). The International Reference Ionosphere model: A review and description of an ionospheric benchmark. *Reviews of Geophysics*, *60*, e2022RG000792. https://doi.org/10.1029/2022RG000792

Received 16 JUN 2022
Accepted 13 SEP 2022

Author Contributions:

Conceptualization: Dieter Bilitza, Michael Pezzopane
Formal analysis: Vladimir Truhlik, Alessio Pignalberi
Methodology: Dieter Bilitza
Visualization: Vladimir Truhlik, Alessio Pignalberi
Writing – original draft: Dieter Bilitza, Michael Pezzopane
Writing – review & editing: Dieter Bilitza, Michael Pezzopane, Vladimir Truhlik, David Altadill, Bodo W. Reinisch, Alessio Pignalberi

The International Reference Ionosphere Model: A Review and Description of an Ionospheric Benchmark

Dieter Bilitza[1,2], Michael Pezzopane[3], Vladimir Truhlik[4], David Altadill[5], Bodo W. Reinisch[6,7], and Alessio Pignalberi[3]

[1]Department of Physics and Astronomy, George Mason University, Fairfax, VA, USA, [2]Heliospheric Laboratory, NASA Goddard Space Flight Center, Greenbelt, MD, USA, [3]Istituto Nazionale di Geofisica e Vulcanologia, Roma, Italy, [4]Institute of Atmospheric Physics of the Czech Academy of Sciences, Prague, Czech Republic, [5]Observatori de l'Ebre, CSIC, Universitat Ramon Llull, Roquetes, Spain, [6]Lowell Digisonde International, Lowell, MA, USA, [7]Space Science Laboratory, University of Massachusetts, Lowell, MA, USA

Abstract This paper is a review of the International Reference Ionosphere (IRI) project and model. IRI is recognized as the official standard for the Earth's ionosphere by the International Standardization Organization, the International Union of Radio Science, the Committee on Space Research, and the European Cooperation for Space Standardization. As requested by these organizations, IRI is an empirical (data-based) model representing the primary ionospheric parameters based on the long data record that exists from ground and space observations of the ionosphere. The core model describes monthly averages of the electron density, electron temperature, ion temperature, and ion composition globally in the altitude range from 60 to 2,000 km. Over time additional parameters were added in response to requests from the user community, this includes the equatorial ion drift, the occurrence probability of spread-F and of an F1 layer, auroral boundaries and the electron content from the bottom of the ionosphere to user-specified altitude. IRI has undergone extensive validations and is used for a wide range of applications in science, engineering, and education. This review is the result of many requests we have received for a comprehensive description of the model. It is also meant as a guide for users who are interested in a deeper understanding of the model architecture and its mathematical formalism.

Plain Language Summary The International Reference Ionosphere (IRI) is the international standard for Earth's ionosphere. The ionosphere is the plasma layer of electrons and ions that surrounds the Earth in the 60–2,000 km altitude range. In spite of being a very small constituent of the atmosphere, the important role of the ionosphere lies in its retarding and refractive effect on electromagnetic waves and in particular radio waves in the different frequency bands from very low frequencies (VLFs) to very high frequencies (VHFs). Because of these effects, IRI is needed and has been used for a wide area of applications including spacecraft navigation, telecommunication, radio astronomy, Earth observation from space, visualizations of geo-space for educational purposes, design of satellites and their payloads, testing data analysis schemes. To support the scientific understanding and operational use, and to explain the limitations of the model, this paper provides a much needed review and description of its scientific background and mathematical formalism.

1. Introduction

The terrestrial ionosphere is a plasma, that is, an ionized gas consisting of free electrons and ions. It is part of the Earth's atmosphere and is produced by solar radiation ionizing the neutral gas constituents. Only a small fraction of the neutral atmosphere is ionized. Typical ratios of electron to neutral gas density are 10^{-2} at the top of the ionosphere (at a height of about 1,000 km), 10^{-3} at the height of the ionospheric absolute electron density maximum (located roughly between 200 and 450 km of height), and 10^{-8} at the bottom of the ionosphere (at a height of about 100 km). These limits mark the altitude boundaries of the ionosphere but they must not be considered fixed. They are highly variable in both space and time, in particular this is the case for the upper limit which marks the separation between the ionosphere below it and the plasmasphere above it (Kelley, 2009; Prölss, 2004; Ratcliffe, 1972; Rishbeth & Garriott, 1969; Schunk & Nagy, 2009; Zolesi & Cander, 2014). In spite of being a very small constituent of the atmosphere, the important role of the ionosphere lies in its retarding and refractive effects on electromagnetic waves, in particular waves with frequen-

cies up to ~300 MHz. Because of this importance, the Committee on Space Research (COSPAR) and the International Union of Radio Science (URSI) initiated the International Reference Ionosphere (IRI) project in 1968. The aim is to develop and continuously improve an international standard for the most important physical parameters of the terrestrial ionosphere. This need was originally triggered by the requirement for an ionosphere model for the satellite-experiment design and satellite data analysis (COSPAR) and for radio propagation purposes (URSI), but over the years the model has gained more and more importance for space weather purposes. In April 2014, IRI became the International Standardization Organization (ISO) standard for the ionosphere by getting officially certified by the International Standardization Organization (ISO 16457: https://www.iso.org/standard/61556.html).

As requested by COSPAR and URSI, IRI is an empirical model being based on ground and space observations of the ionosphere and not depending on the evolving theoretical understanding of the ionospheric processes. Over the years, new versions of the model have been released, as new data became available and old datasets were fully exploited for the development of the model (Bilitza, 1986, 1990, 1997, 2001, 2018; Bilitza & Reinisch, 2008; Bilitza et al., 2011, 2014, 2017; Rawer et al., 1975, 1981; Rawer, Bilitza, & Ramakrishnan, 1978). Being a data-based model, the reliability of IRI depends on the spatial and temporal coverage provided by the underlying datasets. A large availability of data at mid latitudes assures a corresponding good accuracy, while the performance is not so good in regions at high (auroral and polar) and low (equatorial) latitudes, where the data availability is not comparable to that at mid latitudes. Model accuracy is also affected by the hemispheric imbalance in ground station coverage, with a much denser network of stations in the Northern hemisphere (Arikan et al., 2019; Pignalberi, Pietrella, & Pezzopane, 2021). The next section discusses the most important data sources for the IRI model development.

Being solely built on the basis of the existing data record, however, also has the great advantages that the model represents the effect of processes that may have not yet been discovered or have not yet been fully included in theoretical models. A good example is the four maxima structure in the longitudinal variation of the F2-peak electron density that was first discovered by Immel et al. (2006) in Imager for Magnetopause-to-Aurora Global Exploration (IMAGE) EUV observations, and then confirmed by Lühr et al. (2007) with Challenging Minisatellite Payload (CHAMP) data and by Scherliess et al. (2008) with Ocean Topography Experiment data. This feature is thought to be caused by nonmigrating-diurnal atmospheric tides that are driven by tropospheric weather in the tropics. The IRI model already reproduces this phenomenon (McNamara et al., 2010), while theoretical models still struggle to include it in their framework. Conversely, empirical models may have a problem when conditions arise for which no prior data record exists. So, for example, the solar minimum in 2008/2009 was much lower and prolonged than earlier minima (Solomon et al., 2010), and consequently the IRI overestimated data taken during this period (Ezquer et al., 2014; Lühr & Xiong, 2010; Perna et al., 2017).

The IRI model represents monthly averages of the electron density, electron temperature, ion temperature, ion composition (O^+, H^+, He^+, N^+, NO^+, O^+_2, Cluster ions) in the altitude range of 60–2,000 km. IRI also provides the vertical total electron content (vTEC) from the lower boundary to a user-specified upper boundary. Additional IRI outputs include the vertical ion drift near the magnetic equator, the probability for the occurrence of an F1 layer and of spread-F, and the representation of auroral boundaries and their movement with geomagnetic activity. These additional parameters and vTEC were included at the request of the IRI user community because of their importance for specific applications.

A good source for more insight in the IRI developments process and the interaction with the IRI user community is the series of special IRI-related issues of Advances in Space Research (36 up to now; a list is available at http://irimodel.org/docs/asr_list.html). The latest one was published in September of 2021 as issue 5 of volume 68.

This review will describe the model formalism behind each IRI output parameter highlighting corresponding advantages and disadvantages. The importance of the external drivers, in the form of solar, geomagnetic and ionospheric indices, will be also pointed out. Final sections of the review will be devoted to highlighting the recent advances made in data assimilation into IRI and real-time IRI, the achievements of IRI, and a summary of the most recent improvements of IRI with an outlook at plans for the future.

2. Data Used to Develop the Model

As requested by COSPAR and URSI, IRI was implemented as an empirical model representing the synthesis of most of the available and reliable observations of the ionospheric characteristics from the ground and in space. Specifically, the following data sources were used to develop the IRI model:

1. The F2-peak critical frequency *fo*F2, the propagation factor *M*(3000)F2 and the F2-peak height *hm*F2 are based on the long data record accumulated by the worldwide network of ionosondes consisting of 150–170 stations and going back to the fifties. In recent years, the steadily increasing network of digisondes (Reinisch et al., 2009; Reinisch & Galkin, 2011), which provide real-time values of *fo*F2 and *hm*F2, have greatly expanded the global coverage for these important ionospheric characteristics. The Canadian High Arctic Ionospheric Network (CHAIN) of ionosondes are a valuable data source for the high latitudes and provided the data foundation for the development of the Empirical Canadian High Arctic Ionospheric Model (E-CHAIM) (Themens et al., 2017).
2. Incoherent scatter radars (ISRs) are an excellent data source for all of IRI's primary parameters. They can provide top and bottomside profiles for electron and ion densities and temperatures. But only a small number of ISRs have been operated worldwide over time because of the significant costs involved. Data from the ISRs at Jicamarca, Arecibo, St. Santin, Millstone Hill, and Malvern contributed to the development of the IRI models for electron density, electron and ion temperature and composition.
3. Topside sounder measurements by the Alouette-1 and -2, International Satellites for Ionospheric Studies (ISIS)-1 and -2, and Intercosmos 19 satellites were the main database for the electron density profile in the topside ionosphere.
4. The IRI team also made good use of the large volume of data accumulated by satellite in situ measurements from the 60s to the present. These measurements were the main data source for developing the IRI electron and ion temperature and ion composition models. Table 1 summarizes the satellite missions used by the IRI team. The database as a whole extends over more than five solar cycles.
5. The D region and the bottomside of the E region are too low for satellite in situ measurements and too difficult to sound from the ground because of the low ion/electron densities and high neutral densities. Here IRI has to rely on rocket measurements. Different compilations of rocket data were put together to model the electron density and ion composition in this region.
6. vTEC data from Global Navigation Satellite System (GNSS) satellites have been primarily used in comparative studies with IRI (e.g., Reddybattula & Panda, 2019; Tariku, 2019). However, these studies have to account for the plasmaspheric contribution to vTEC, which currently is not included in the standard IRI. Various plasmaspheric extensions have been proposed for IRI (Section 3.9) but they have not yet reached the same degree of maturity as the rest of the IRI model. An assessment of the plasmaspheric contribution to vTEC was presented by Cherniak and Zakharenkova (2016).
7. Constellation Observing System for Meteorology, Ionosphere, and Climate (COSMIC) radio occultation (RO) data have been used for global modeling of *hm*F2 (Shubin, 2015) and there have also been many comparisons of the IRI electron density F2-peak parameters with RO data from COSMIC and other satellites (e.g., H. Huang et al., 2021; Moses et al., 2021; Pignalberi, Pietrella, & Pezzopane, 2021). However, the inherent assumption of spherical symmetry makes RO analysis difficult in regions of sharp gradients as for example, the equatorial ionization anomaly (EIA) region (e.g., Wu et al., 2009; Yue et al., 2010).
8. Ground-based absorption measurements have been consulted to better understand the variation patterns of the electron density in the lower ionosphere.

The IRI working group has been proactive in finding new data sources and in fully exploiting older data sources (like the Alouette/ISIS topside sounder data). Special IRI workshops discussed the most reliable data sources for the lower ionosphere and helped to resolve discrepancies that existed early on between measurements from the ground and in space.

3. Electron Density and Vertical Total Electron Content

For many users of ionospheric models one of the most important physical quantities is the electron density, because it determines the refractive index of the plasma and therefore the magnitude of the plasma's effect on electromagnetic waves traveling through it. The electron density profile in Earth's ionosphere is characterized by

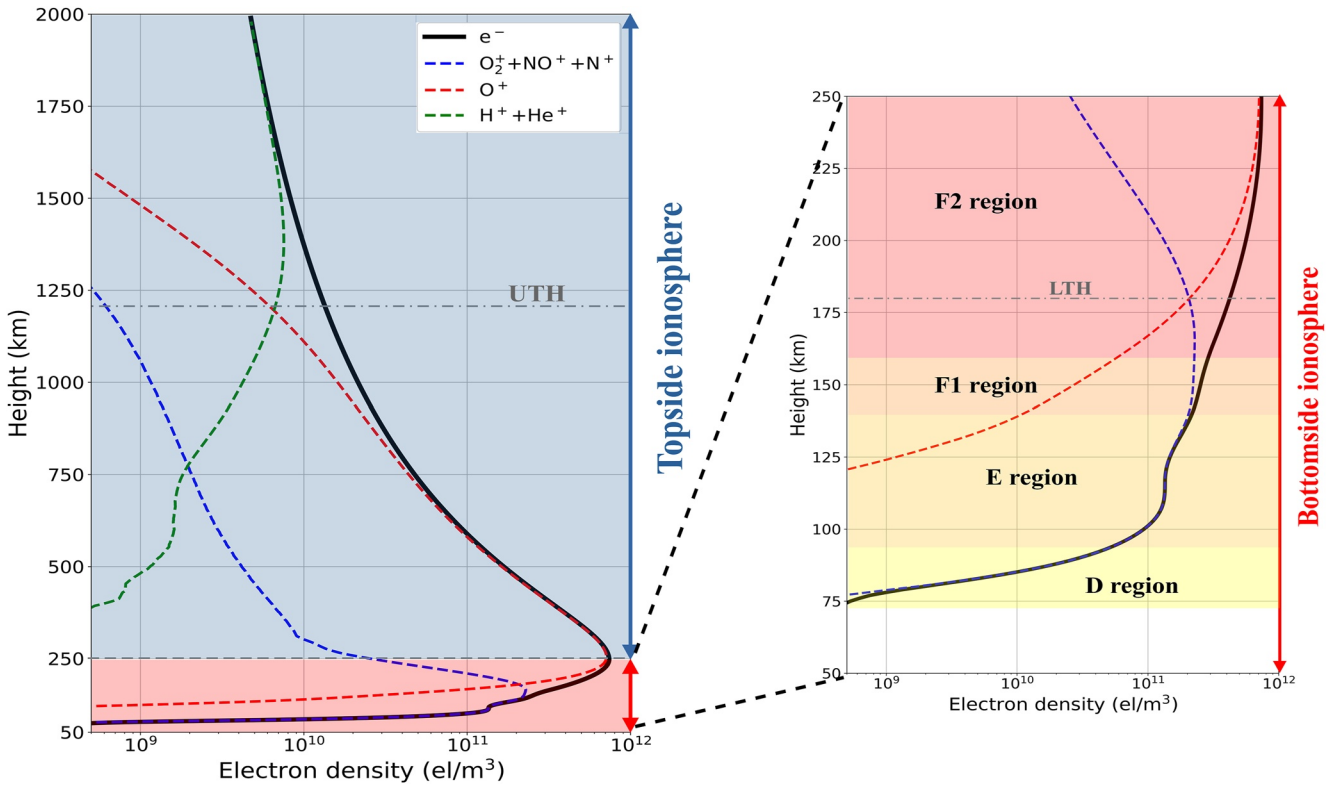

Figure 1. (left) A typical vertical electron density profile from the base of the ionosphere to an altitude of 2,000 km; profiles of molecular and atomic ions are also shown. UTH is the upper transition height, that is the height where the percentage of O^+ is equal to the percentage of light ions H^+ and He^+. (right) Expanded view of the bottomside ionosphere highlighting the different ionospheric regions. LTH is the lower transition height, which is the height where the percentage of O^+ is equal to the percentage of molecular ions.

several layers that are formed by the interaction of solar irradiance in the extreme ultraviolet (EUV) and X-ray range with the atomic and molecular gases of the terrestrial atmosphere. Figure 1 shows a typical ionospheric vertical electron density profile identifying these different layers (D, E, F1, and F2).

IRI models the ionospheric vertical electron density profile by dividing it into six sub-regions as shown in Figure 2, including the topside, the F2 bottomside, the F1 layer, the intermediate region, the E valley, and the E bottomside and D region, identified respectively by the numbers (1–6) in Figure 2.

The boundaries of these subsections are identified by several characteristic points including the F2, F1, and E-layer peaks. The F2- and E-layer peaks are of particular importance because they are anchor points for the F2-region and E-region profiles, respectively. This means that the electron densities in the topside and bottomside are normalized to the F2-peak electron density *Nm*F2 and the densities in the E valley and E bottomside are normalized to the E-peak electron density *Nm*E. The F1-layer peak point, although it is not an anchor point, is important for locating the F1-ledge on the bottomside profile. The F2-peak-normalized and the E-peak-normalized parts of the electron density profile are merged in the "intermediate region." The full vertical electron density profile is described by a set of mathematical expressions, each valid in a defined range of altitude. These expressions are described in the following sections starting from the topside down to the D region. All densities are in el/m^3, all frequencies in MHz, and heights in km.

3.1. The Topside Profile

The IRI provides the user with four options to model the electron density in the topside ionosphere (region (1) in Figure 2): IRI-2001, IRI-2001cor, NeQuick, and COR2. Bilitza (2009) using a large volume of Alouette-1, -2, and ISIS-1, -2 topside sounder data evaluated the first three of these options in terms of overall performance, as well as the accurate representation of the observed altitudinal-latitudinal structure with a special focus on the EIA

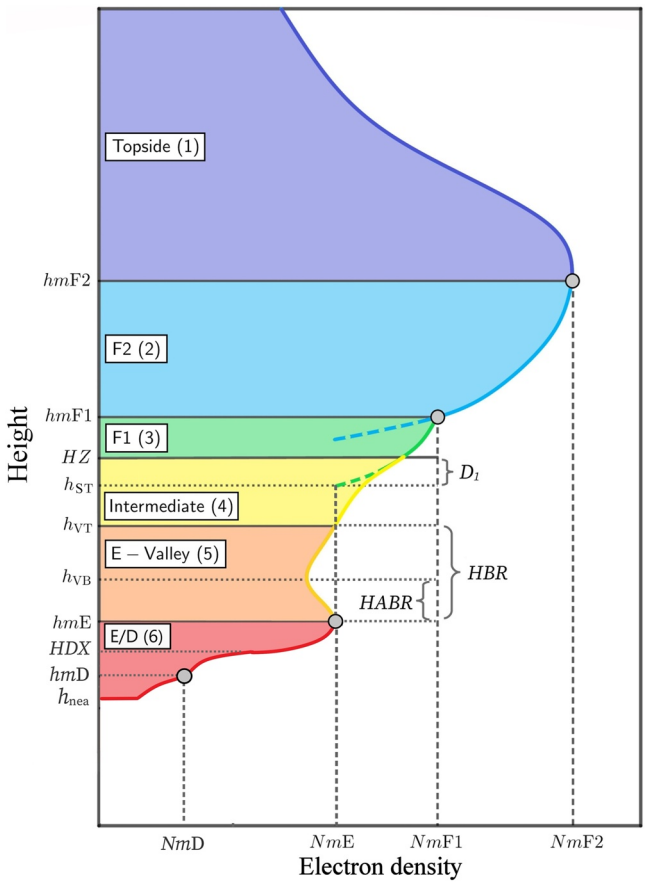

Figure 2. The International Reference Ionosphere electron density profile and its division into six sub-regions that are separately modeled. The F2-layer, F1-layer, and E-layer peaks and D-region inflection point are highlighted as gray circles.

region. The EIA region is characterized by two latitudinal maxima (crests) on both sides of the magnetic equator at lower altitudes, which then merge into a single maximum at the equator at higher altitudes. This poses a special challenge because the profile is normalized to the F2 peak which inherently introduces the EIA camel-back structure also at higher altitudes. The profile function, therefore, needs to counter-act this behavior and move the crests closer to the magnetic equator with increasing altitude until the merge into a single peak. Like earlier studies, Bilitza (2009) found the largest discrepancies for the IRI-2001 option. In fact, the IRI-2001cor model was developed to overcome the shortcomings of the IRI-2001 model option. Best results were obtained with the NeQuick option, which was accordingly declared the recommended IRI option and is the default option in the computer program. In general, he found better results at mid latitudes than at high and low latitudes. Similar results were reported by Migoya-Orué et al. (2013) using plasma density values measured by the F13 and F15 Defense Meteorological Satellites Program (DMSP) satellites, by Klenzing et al. (2013) with topside ionospheric densities over Africa measured by the Communications/Navigation Outage Forecasting System (C/NOFS) satellite, by Wang et al. (2016) with Arecibo, Jicamarca, and Millstone Hill ISR observations from 2001 to 2014, and by Pignalberi et al. (2016) who analyzed the behavior of the IRI topside options during the St. Patrick storm that occurred in March 2015. Bilitza (2009) found that the typical altitude-latitude structure of the EIA region, however, is better represented by the IRI-2001cor option. While the NeQuick option shows the F-region crests also at higher altitudes, the IRI-2001cor option reproduces the merging of the F-region crests into a single equatorial crest as the altitude increases.

Lühr and Xiong (2010) noted that either one of these options significantly overestimated CHAMP and Gravity Recovery and Climate Experiment (GRACE) satellite measurements during the very low solar cycle minimum in 2008–2009. Similar results were reported by Klenzing et al. (2011, 2013) and by Bilitza et al. (2012) based on data from the C/NOFS satellite. Bilitza and Xiong (2021) developed a solar-activity dependent correction function for the IRI-2001cor model that overcomes these shortcomings and was included as a fourth option (COR2) in the IRI.

3.1.1. The IRI-2001 Option

The name "IRI-2001" for this option is somewhat misleading because it is based on much earlier work, namely studies by Rawer and Ramakrishnan as reported in Rawer, Bilitza, and Ramakrishnan (1978), Rawer, Bilitza, Ramakrishnan, and Sheikh (1978), and in Rawer (1984) especially on pages 351–353. The model is an analytical description of the Bent et al. (1972) model, which is based on Alouette-1 topside sounder data and in its original form consisted of a set of graphs of the exponential scale heights in three altitude regimes in terms of critical frequency *fo*F2, geomagnetic latitude, and 12-month running mean of monthly solar *F*10.7 radio flux. IRI-2001 uses a Booker function (Booker, 1977) to connect the different altitude regimes. In the Booker (1977) approach, the profile (in our case $\ln(N_e/NmF2)$, where N_e is the electron density) is divided into segments with constant gradient and Epstein step-functions are used to represent the whole gradient profile analytically (see Appendix A for a description of the Booker approach and function). This analytical representation helped to smooth out some of the unreasonable sharp transitions between different altitude regimes in the Bent et al. (1972) model. The IRI-2001 option describes the topside electron density as

$$N_e(h) = NmF2 \cdot \exp\left[-\frac{B(x)}{\alpha}\right], \quad (1)$$

Table 1
Satellite In Situ Data Used for International Reference Ionosphere (IRI) Development With Orbit Information and the Data Time Period Used for IRI

Satellite	Time period	Altitude (km)	Latitude (deg)	LT (hr)
Alouette-1	9/1962–12/1971	990–1,070	[−80, +80]	0–24
Explorer 31	11/1965–8/1968	500–3,010	[−79, +79]	0–24
Alouette-2	12/1965–7/1972	500–3,000	[−80, +80]	0–24
ISIS-1	2/1969–5/1980	580–3,550	[−88, +88]	0–24
OGO-6	12/1969–4/1971	390–1,090	[−82, +82]	0–24
ISIS-2	4/1971–8/1979	1,360–1,460	[−88, +88]	0–24
AEROS-A	1/1973–8/1973	200–870	[−83, +83]	3, 15 fixed
AE-C	12/1973–12/1978	130–4,300	[−68, +68]	0–24
AEROS-B	7/1974–9/1975	140–880	[−83, +83]	4, 16 fixed
AE-D	10/1975–1/1976	140–3,700	[−90, +90]	0–24
AE-E	12/1975–5/1981	140–1,580	[−20, +20]	0–24
ISS-b	8/1978–7/1981	970–1,240	[−69, +69]	0–24
Intercosmos 19	3/1979–1/1981	500–1,020	[−74, +74]	0–24
Hinotori	2/1981–6/1982	560–640	[−31, +31]	0–24
DE-2	8/1981–2/1983	200–1,020	[−90, +90]	0–24
San Marco 5	4/1988–12/1988	170–590	[−3, +3]	0–24
Intercosmos 24	10/1989–11/1991	500–2,530	[−83, +83]	0–24
DMSP F10	12/1990–6/1993	730–860	[−90, +90]	8–20 fixed
DMSP F11	12/1991–6/1993	850–870	[−90, +90]	5–17 fixed
Intercosmos 25	12/1991–6/1993	440–3,110	[−83, +83]	0–24
SROSS C2	1/1995–12/2000	380–620	[−40, +45]	0–24
DMSP F13	3/1995–12/2005	840–880	[−90, +90]	5.75, 17.75
DMSP F12	1/1996–6/2002	840–890	[−90, +90]	9.5, 21.5
DMSP F14	1/1997–12/2005	840–880	[−90, +90]	9.5, 21.5
ROCSAT-1	3/1999–6/2004	560–665	[−35, +35]	0–24
DMSP F15	12/1999–12/2017	830–880	[−90, +90]	9.5, 21.5
KOMPSAT	6/2000–8/2001	~685	[−90, +90]	22.8
CHAMP	8/2000–2/2010	310–460	[−87, +87]	0–24
TIMED	12/2001–12/2009	625	[−74, +74]	0–24
GRACE	4/2002–4/2015	390–540	[−89, +89]	0–24
COSMIC I	4/2006–4/2020	490–870	[−72, +72]	0–24
C/NOFS	8/2008–11/2015	260–860	[−13, +13]	0–24
Swarm A, C	12/2013–12/2019	430–530	[−90, +90]	0–24
Swarm B	12/2013–12/2019	490–550	[−90, +90]	0–24
ICON	10/2019–6/2020	575–610	[−27, +27]	0–24

and uses the Booker function $B(x)$ in the form:

$$B(x) = \beta \cdot \eta \cdot E_1(x) + \xi \cdot [100E_2(x) - \alpha \cdot (h - hm\mathrm{F2})], \tag{1a}$$

with

$$E_1(x) = \mathrm{Eps}_{-1}(x; 394.5, \beta) - \mathrm{Eps}_{-1}(x_0; 394.5, \beta), \tag{1b}$$

$$E_2(x) = \mathrm{Eps}_{-1}(x; 300, 100) - \mathrm{Eps}_{-1}(x_0; 300, 100), \tag{1c}$$

Table 2
IRI-2001 Topside Profile Parameters

	η	ξ	β
t_0	0.058798	0.078922	−128.03
t_1	−0.08	−0.0046702	20.253
t_2	−0.014065	−0.019132	−8.0755
t_3	0.0069724	0.0076545	−0.65896
t_4	0.0024287	0.0032513	0.44041
t_5	0.004281	0.006029	0.71458
t_6	−0.0001528	−0.00020872	−0.042966

where η and ξ are the constant gradients, and β and 100 the thicknesses of the transition regions (see Appendix A for the definition of the Epstein functions). x is a modified altitude variable that translates the height range hmF2 to 1,000 km into the range x_0 to $x_0 + 700$

$$x - x_0 = \alpha \cdot (h - hm\mathrm{F2}), \tag{1d}$$

with the transformation factor α

$$\alpha = \frac{700}{1000 - hm\mathrm{F2}}, \tag{1e}$$

and the new peak height x_0

$$x_0 = 300 - \delta, \tag{1f}$$

where δ is a corrective term and minimizing for this corrective term one finds:

$$\delta = \frac{\frac{\eta}{1+Z} - \frac{\xi}{2}}{\frac{\eta}{\beta}\frac{Z}{(1+Z)^2} + \frac{\xi}{400}}, \tag{1g}$$

with

$$Z = \exp\left(\frac{94.5}{\beta}\right). \tag{1h}$$

The parameters η, ξ, and β are functions of the same parameters that were used in the Bent model: the geomagnetic latitude λ, the F2-layer critical frequency foF2 and $F10.7_{365}$, the 365-day running mean of the daily solar flux $F10.7_{\mathrm{d}}$.

$$\begin{aligned}\xi, \beta = {} & t_0 + t_1 \cdot T(\lambda) + t_2 \cdot R(F10.7_{365}) + t_3 \cdot T(\lambda) \cdot R(F10.7_{365}) + t_4 \cdot fo\mathrm{F2} \\ & + t_5 \cdot fo\mathrm{F2} \cdot T(\lambda) + t_6 \cdot (fo\mathrm{F2})^2,\end{aligned} \tag{1i}$$

$$\begin{aligned}\eta = {} & t_0 + t_1 \cdot T_{\mathrm{m}}(\lambda) + t_2 \cdot R(F10.7_{365}) + t_3 \cdot T(\lambda) \cdot R(F10.7_{365}) + t_4 \cdot fo\mathrm{F2} \\ & + t_5 \cdot fo\mathrm{F2} \cdot T(\lambda) + t_6 \cdot (fo\mathrm{F2})^2,\end{aligned} \tag{1j}$$

where

$$T(\lambda) = \cos^2 \lambda, \tag{1k}$$

$$T_{\mathrm{m}}(\lambda) = \mathrm{Eps}_1(\lambda; 0, 15), \tag{1l}$$

and

$$R(F10.7_{365}) = \begin{cases} \dfrac{F10.7_{365} - 40}{30} & \text{for } F10.7_{365} < 188 \\ 4.93 & \text{for } F10.7_{365} \geq 188 \end{cases}. \tag{1m}$$

The Epstein layer function $T_{\mathrm{m}}(\lambda)$ centered at the magnetic equator was introduced by Bilitza (1985b) to better represent AEROS-A and -B, and Atmospheric Explorer (AE)-C satellite in situ measurements at low latitudes and ISR measurements from Jicamarca and Arecibo. The coefficients t_i of Equations 1i and 1j are listed in Table 2. They were obtained by a non-linear least-square fitting procedure to the Bent et al. (1972) topside profiles.

3.1.2. The IRI-2001cor and COR2 Options

After its implementation in the IRI model a number of studies had found discrepancies between this IRI topside model and measurements (Bilitza & Williamson, 2000; Ezquer et al., 1998; Iwamoto et al., 2002; Třísková et al., 2002). In particular, it was found that the IRI-2001 topside model overestimates the electron density in the upper topside and unrealistically steep, almost vertical, profiles could be generated, especially at high latitudes for high solar activity. To overcome these problems Bilitza (2004) introduced a correction term *TCOR* into the IRI-2001 topside formalism and studied the variation of this term with height, modip (introduced by

Table 3
Model Parameters for the IRI-2001cor Option

	a	*b*	*c*	*d*
Daytime	−0.84	−0.67	550	1,900
Nighttime	−0.84	−1.60	230	700

Rawer [1963]; see Section 8) and local time (LT) using a large database of about 120,000 topside profiles from Alouette-1, -2, and ISIS-1, -2 topside sounder measurements. With the correction term Equation 1 becomes

$$N_e(h) = NmF2 \cdot \exp\left[\frac{-B(x)}{\alpha} + TCOR(h, \text{modip}, \text{day/night})\right]. \quad (2)$$

Identifying the "old" IRI-2001 topside model in Equation 1 as $N_{e,\text{IRI-2001}}$ and substituting it in Equation 2 we get

$$\frac{N_e(h)}{N_{e,\text{IRI-2001}}} = \exp[TCOR(h, \text{modip}, \text{day/night})], \quad (3)$$

and therefore the correction term is determined by the logarithm of the observed electron density versus the IRI-2001 value. Different approaches were investigated and very good results were achieved with a linear interpolation between a starting height h_1 (above hmF2) and $h_2 = hm$F2 + 1,500 km

$$TCOR(h, \text{modip}, \text{day/night}) = \left[a + b \cdot \text{Eps}_1(\text{modip}; 0, 10)\right] \cdot \frac{(h - h_1)}{(h_2 - h_1)} \cdot \ln 10; \quad (4)$$

$TCOR$ is equal to zero at h_1 and varies with modip at h_2

$$TCOR(h_1) = 0 \quad \text{and} \quad TCOR(h_2) = a + b \cdot \text{Eps}_1(\text{modip}; 0, 10) \cdot \ln 10. \quad (4a)$$

The starting height h_1 can be described as a function of modip in the form

$$h_1 = hm\text{F2} + c + d \cdot \text{Eps}_1(\text{modip}; 0, 19); \quad (4b)$$

the parameters a, b, c, and d were determined by fitting to the Alouette/ISIS database separately for daytime (LT = 10–14) and nighttime (LT = 22–02) conditions and are listed in Table 3.

For the description of the variation with local time the HPOL function (Appendix A) is used to provide a smooth transition from the h_1 daytime value to its nighttime value with transitions at sunrise and sunset, and the same for $TCOR(h_2)$.

The inclusion of the correction term resulted in a significant improvement over the older IRI-2001 topside model. While the IRI-2001 model option overestimated the Alouette/ISIS data by an overall average of 165%, the new IRI-2001cor option reduced this number to 46%. An even better result (24%) was provided by the NeQuick option that will be explained in the next section.

Recently Bilitza and Xiong (2021) improved the IRI-2001cor model by adding a solar activity term $SCOR(PF10.7)$ to $TCOR$ in Equation 2 with a linear dependence on the solar activity index $PF10.7$ (see Section 9.1)

$$SCOR(PF10.7) = A_0 + A_1 \cdot PF10.7. \quad (5)$$

They used in situ measurements from CHAMP, GRACE, and Swarm, as well as topside sounder data from Alouette-1, -2, and ISIS-1, 2 to describe the latitudinal and altitudinal variation of A_0 and A_1 using Booker functions (Appendix A). This new version, called COR2, shows better performance than the other options when compared with the Alouette and ISIS data (IRI-2001cor: −67%; NeQuick: −42%; COR2: −36%) and is a candidate to become the IRI default.

3.1.3. The NeQuick Option

The NeQuick modeling approach was started by Leitinger et al. (2001) and Radicella and Leitinger (2001) who established empirical relationships between ionospheric electron density parameters based on ionosonde and vTEC data. Their mathematical representation of the topside utilizes an Epstein layer function (Coïsson et al., 2006, 2009; Nava et al., 2008):

$$N_e(h) = 4NmF2 \cdot \text{Eps}_1(h; hm\text{F2}, H), \quad (6)$$

where H is a height-dependent scale height

$$H = H_0 \left[1 + \frac{r \cdot g \cdot (h - hm\mathrm{F2})}{r \cdot H_0 + g \cdot (h - hm\mathrm{F2})}\right], \tag{6a}$$

with r and g which are constant factors equal to 100 and 0.125, respectively. H_0 is the value of H at the F2-peak height hmF2 and is described as

$$H_0 = k \cdot B_{2\mathrm{bot}}, \tag{6b}$$

where $B_{2\mathrm{bot}}$ is the NeQuick bottomside thickness parameter and k is defined as

$$k = 3.22 - 0.0538 f o\mathrm{F2} - 0.00664 hm\mathrm{F2} + 0.113 \frac{hm\mathrm{F2}}{B_{2\mathrm{bot}}} + 0.00257 R_{12}, \tag{6c}$$

with R_{12} the 12-month running-mean of sunspot number. $B_{2\mathrm{bot}}$ is related to the density derivative at the inflection point $(\mathrm{d}N_e/\mathrm{d}h)_{\max}$ of the Epstein layer as

$$B_{2\mathrm{bot}} = \frac{0.04774 f o\mathrm{F2}^2}{\left(\frac{\mathrm{d}N_e}{\mathrm{d}h}\right)_{\max}}. \tag{6d}$$

Mosert de Gonzales and Radicella (1990) determined the following empirical relationship for $(\mathrm{d}N_e/\mathrm{d}h)_{\max}$ based on ionosonde data

$$\left(\frac{\mathrm{d}N_e}{\mathrm{d}h}\right)_{\max} = 0.01 \exp[-3.467 + 1.714 \ln(f o\mathrm{F2}) + 2.02 \ln(M(3000)\mathrm{F2})]. \tag{6e}$$

The propagation factor M(3000)F2 is determined with the Consultative Committee on International Radio (CCIR) model (see Sections 3.2.1 and 3.3). It is important to note that while a user can enter their own ionosonde-measured value of M(3000)F2, this will not affect Equation 6e, which was developed based on CCIR model values and will always use the CCIR model for M(3000)F2. Recently Pezzopane and Pignalberi (2019) have presented a new formulation for the H_0 parameter that shows very promising results and may result in future updates of the model. Others have explored modifying the r and g parameters of the NeQuick model to better represent the curvature of the scale height in the topside (Pignalberi et al., 2022; Themens et al., 2018).

3.2. The F2-Peak Plasma Frequency *fo*F2 and Density *Nm*F2

The F2-peak plasma frequency *fo*F2 and density *Nm*F2 are two of the most important parameters for any ionospheric model or application of such a model because they are the highest values reached in the ionosphere. The two are related by the plasma physics formula

$$N_e/m^{-3} = 1.24 \cdot 10^{10} (f_P/\mathrm{MHz})^2, \tag{7}$$

where f_P is the plasma frequency associated with the electron density N_e. IRI gives the user two options for these important parameters: the model recommended by the CCIR of the International Telecommunication Union (ITU) and the model developed by a special URSI working group. Both models use the same mathematical functions but different sets of ionosonde data and different ways of filling data gaps in the ocean areas and other data-sparse regions of the globe. CCIR maps are recommended mainly for land regions, whilst URSI maps are recommended when the mapping area includes large ocean areas. A user can choose between these two options, or give their own values of either *fo*F2 or *Nm*F2.

3.2.1. The CCIR *fo*F2 Model

CCIR maps are based on a procedure of numerical mapping pioneered by Jones and Gallet (1962, 1965) and Jones et al. (1969). They used a Fourier time series in universal time (UT) to describe the diurnal variation of monthly medians of *fo*F2 observed at each one of the worldwide network of ionosonde stations from which they had received data (about 150 in total)

$$f o\mathrm{F2}(\varphi, \phi, T) = a_0(\varphi, \phi) + \sum_{i=1}^{M} [a_{2i-1}(\varphi, \phi) \cos(i \cdot T) + a_{2i}(\varphi, \phi) \sin(i \cdot T)], \tag{8}$$

where φ and ϕ are the geographic latitude and East longitude [0,360) of the specific station, T is the universal time expressed as an angle [−180,180) and M is the maximum number of the harmonics used to represent the detailed structure of the diurnal variation. For *fo*F2, M is set to 6 and thus 13 coefficients are considered in the expansion (Equation 8) for *fo*F2. A special set of geographic functions is then used to describe the variation of the Fourier coefficients with geographic coordinates and with the special modified dip coordinate, modip μ (see Section 8), that was introduced by Rawer (1963) to describe the magnetic field dependence of ionospheric parameters. These functions are defined as

$$a_i(\varphi,\phi) = \sum_{j=0}^{J(0)} c_{i,j,0} P_{j,0}(\varphi,\phi) + \sum_{k=1}^{8} \sum_{j=0}^{J(k)} \left(c_{i,j,2k-1} \cos(k\cdot\phi) + c_{i,j,2k} \sin(k\cdot\phi)\right) P_{j,k}(\varphi,\phi), \tag{8a}$$

with $i = 0,\ldots,6$ and

$$P_{j,k}(\varphi,\phi) = [\sin\mu(\varphi,\phi)]^j (\cos\varphi)^k. \tag{8b}$$

Equation 8a uses an 8-degree harmonic expansion to describe the longitudinal structure. For additional compactness of the set of coefficients, Jones and coworkers experimented with truncating higher degrees of the latitudinal expansion to smaller orders $J(k)$ without loss of accuracy (see CCIR [1967] for further details). Specifically, the summation cutoffs $J(k)$ are 11, 11, 8, 4, 1, 0, 0, 0, 0 for $k = 0,\ldots,8$. With these adjustments the total number of longitude-latitude functions and coefficients for each of the 13 Fourier coefficients came to $K = 76$ for *fo*F2.

A major challenge for this analysis scheme was the irregular distribution of ionosonde stations across the globe with large areas of missing data in particular over the oceans. Jones and Gallet (1965) overcame this problem by adding so-called "screen points" (or "phantom stations") in data-sparse regions. They made the assumption that the local time variation of *fo*F2 is the same along lines of constant magnetic dip latitude and so they could extrapolate from a known station to phantom stations on the same field line to cover ocean areas and data-sparse regions. Considering the order of expansion in UT, φ, and ϕ, the IRI model needs 13 diurnal × 76 spherical = 988 coefficients to globally represent the 24-hr variation of the monthly median *fo*F2. The seasonal variation of *fo*F2 is taken into account by obtaining these coefficients for every month of the year. Jones and Gallet (1962, 1965) calculated these monthly coefficient sets for different years including 1954 and 1955 representing solar minimum conditions and 1956–1958 for the solar maximum. A linear fit was then applied to describe the variation with R_{12} and based on this linear relationship two sets of monthly coefficients were established, one for $R_{12} = 0$ and one for $R_{12} = 100$. Between/beyond these two extremes a linear inter/extra-polation scheme was recommended.

A problem, however, was found when extrapolating to R_{12} values beyond 150. The observed *fo*F2 no longer increased but reached an almost constant value (Balan et al., 1994). This saturation effect is at least partially due to the insufficiency of the R_{12} index in representing the solar cycle variation of the solar EUV irradiance that is responsible for the ionospheric ion production. But seasonal and latitudinal effects also play an important role as was shown by J. Y. Liu et al. (2003) and Ma et al. (2009). The CCIR model and IRI first accounted for this saturation effect by keeping R_{12} at 150 even if the observed R_{12} reached higher values. A better option became available with the introduction of the ionosonde-based Ionospheric Global (*IG*) index by R. Liu et al. (1983) (for details see Section 9.2). This index was specifically developed for use with the CCIR maps and since it is based on ionosonde data it inherently includes the saturation effect. As in the case of sunspot number R, the best correlation with monthly median *fo*F2 is found with the 12-month running mean of *IG* (IG_{12}). With the new index the CCIR coefficients remain the same, just the reference levels are redefined from $R_{12} = 0$ and 100 to $IG_{12} = 0$ and 100 and a saturation adjustment is no longer required.

Figure 3 shows some examples of *fo*F2 global maps for different hours, months and solar activity demonstrating how well CCIR and IRI represent the EIA with the so-called fountain effect. The interaction of the magnetic and electric field ($\mathbf{E}\times\mathbf{B}$ force, where $\mathbf{E}$ is the zonal electric field and $\mathbf{B}$ the geomagnetic field) pushes the ionospheric plasma vertically upward at the magnetic equator, which then flows down along magnetic field lines creating maxima on both sides of the magnetic equator at about ±20° magnetic latitude.

3.2.2. The URSI *fo*F2 Model

The CCIR model has been and still is widely used for telecommunication applications, but with the availability of satellite data, discrepancies were found, especially in regions that were not well covered by the database

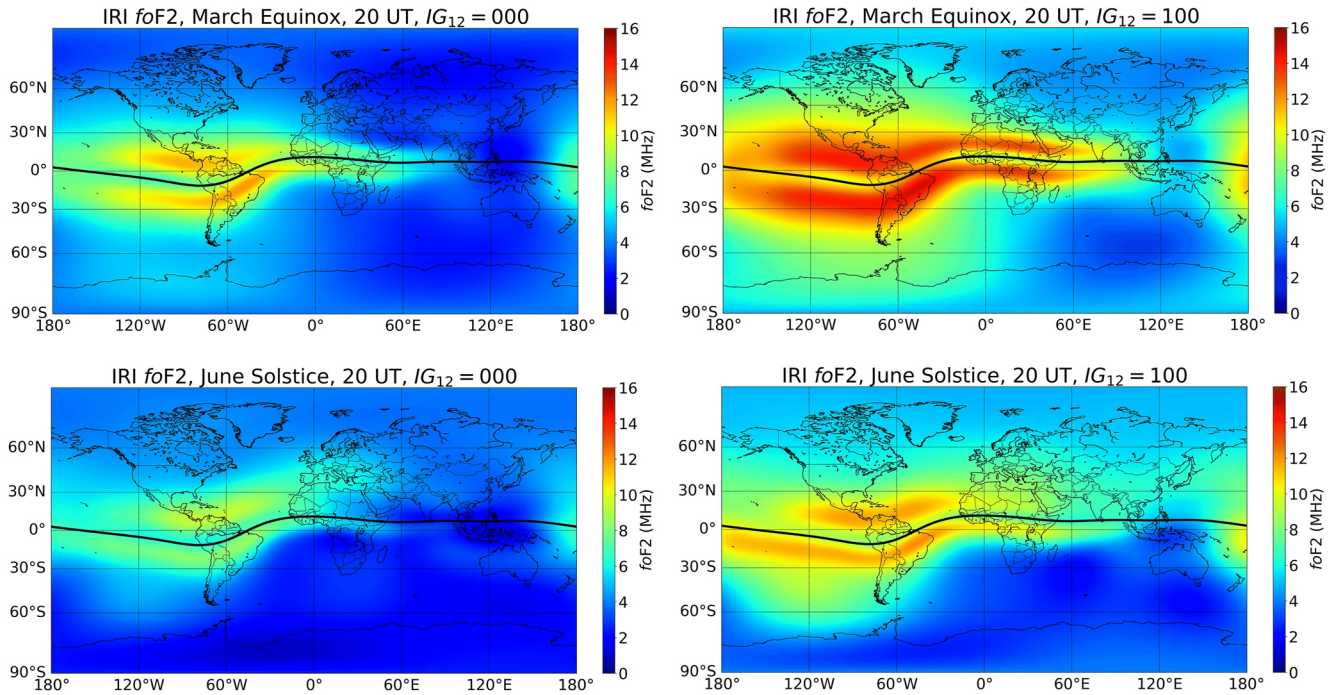

Figure 3. Global maps of *fo*F2 obtained in (upper panels) March and (lower panels) June at 20 UT for IG_{12} equal to (left panels) 0 and (right panels) 100. The black solid curve represents the geomagnetic equator.

underlying the CCIR model development (J. W. King, 1973; Matuura et al., 1981; Sheik et al., 1978). In response, the URSI assembled an international working group of experts to develop an improved model for *fo*F2. First improvements were presented by Rush et al. (1983, 1984) who worked with the same functions that were used in the CCIR model but applied a theoretical model to determine screen points in the ocean areas and other data sparse regions. Actually, theoretical values were only calculated for magnetic latitudes greater than ±25°. At low latitudes electron transport across field lines has to be considered, which complicates the calculations considerably. At these latitudes, screen points were deduced from global contour maps at constant local time. Their analysis is based on data from 110 ionosonde stations for the solar minimum period July 1975 to June 1976 and the solar maximum period July 1978 to June 1979. Fox and McNamara (1988) went a step further by combining the screen point technique of Rush et al. (1983) with the large volume of worldwide ionosonde data (over 45,000 station-months) collected by the Australian Ionospheric Prediction Service and results from the analysis of Ionosphere Sounding Satellite (ISS)-b topside sounder satellite data. They also improved the modeling technique by using higher order terms and by making the order depending on magnetic latitude. It was, however, decided to stick with the CCIR set of functions, because this formalism was used in many existing telecommunication applications. With this in mind, the final set of URSI model coefficients was determined by first using the Fox and McNamara (1988) modeling approach to establish a narrow grid of global *fo*F2 values and then fitting these data with the CCIR set of functions as described by Rush et al. (1989). Similarly to the CCIR coefficients the URSI coefficients are provided for each month and for $IG_{12} = 0$ and 100.

Compared to the ISS-b topside sounder data the URSI *fo*F2 model showed a slightly better overall performance than the CCIR model and, as expected, significant improvements in the ocean areas (Bilitza et al., 1987, 1988; Rush et al., 1989). However, since the same order of harmonic representation is used in both models the improvement over the oceans can come at the expense of a slightly diminished accuracy over land. IRI recommends use of the URSI *fo*F2 model for the ocean areas and the CCIR model over land. One has, however, to keep in mind that the *IG* index is based on the CCIR model. Calculating an *IG* index based on the URSI model, Brown et al. (2018) find slight differences compared to the *IG* index based on the CCIR model. But the differences are negligibly small and in IRI the standard CCIR-based *IG* index is used for both models.

3.2.3. The *fo*F2 Storm Model

Developing an algorithm for updating the IRI parameters during storm-time conditions has long been a high priority of the IRI team. With the IRI-2001 version, the *fo*F2 storm model developed by Fuller-Rowell et al. (2000) and Araujo-Pradere et al. (2002) was included as a new option in the IRI model. Their empirical storm-time correction model is based on the analysis of data from 75 ionosonde stations and 43 storms, and benefits from the knowledge gained from simulations from a physically based model. It captures the most obvious, long-lived, coherent feature of the ionospheric response to a geomagnetic storm, which is the deep ion depletion ("negative phase") that typically develops in the summer hemisphere during the driven phase of a storm and persists well into the recovery phase (e.g., Mendillo, 2006). The model also includes the well-established diurnal differences in the storm response: mid-latitude stations show a minimum in the ratio of disturbed to quiet *Nm*F2 in the morning hours and a maximum around 18:00 LT; this is a result of the compositional changes in response to the diurnally varying winds (upwelling/downwelling of molecular ions) (Prölss, 2004). They achieve the description of the average storm effects by introducing a new magnetic index X that is based on 33-hr prior history of the a_p index. A cubic polynomial was found to fit the data

$$\Phi = \left[a_0 + a_1 \cdot X\left(t_0\right) + a_2 \cdot X^2\left(t_0\right) + a_3 \cdot X^3\left(t_0\right)\right]\left[1 + a_4 \sin(LT + \alpha)\right], \tag{9}$$

with

$$\Phi = \left(fo\mathrm{F2}_{\mathrm{storm}} / fo\mathrm{F2}_{\mathrm{monthly\_average}}\right) \tag{9a}$$

and the new index X defined as the integral over the 3-hourly geomagnetic a_p index over the previous 33 hr

$$X\left(t_0\right) = \int F(\tau) \cdot a_p\left(t_0 - \tau\right) \mathrm{d}\tau; \tag{9b}$$

the weighting function $F(\tau)$ was obtained by the singular value decomposition method (Detman & Vassiliadis, 1997) minimizing the mean square difference between the filter input (a_p index) and filter output (Φ). The filter was constructed from mid-latitude data only. Ideally, separate filters are required for the other latitude regimes and for different seasonal conditions, but the approach was not feasible at the time due to the limited size of the data sample at high and low latitudes. The coefficients a_0, a_1, a_2, and a_3 are adjusted to fit the non-linear relationship between the ionospheric response and the index X, while a_4 and α are respectively the amplitude and the phase of the LT dependence.

The storm option (Equation 9) gives reliable results at mid latitudes during summer and equinox, but during winter and at low latitudes it does not improve significantly the quiet *fo*F2 representation made by IRI (Araujo-Pradere & Fuller-Rowell, 2001, 2002; Araujo-Pradere et al., 2003, 2004; Oyeyemi et al., 2013).

Figure 4 shows the *fo*F2 values measured by the ionosondes installed at Tromsø (69.60°N, 19.20°E), Chilton (51.50°N, 359.40°E), Ramey (18.50°N, 292.40°E), and Hermanus (34.42°S, 19.22°E) and those modeled by IRI with the IRI STORM option ON and the IRI STORM option OFF during the occurrence of the St. Patrick storm (16–21 March 2015). The figure documents the improvement achieved with the IRI STORM option in describing storm-time *fo*F2 especially at mid latitudes (Chilton and Hermanus) and also at high latitudes (Tromso), while at the low-latitude station Ramey there is no difference between the IRI values modeled with IRI STORM option ON and OFF.

3.3. The F2-Peak Height *hm*F2

The height of the F2 peak, *hm*F2, is of great importance for many radio propagation studies and applications because it marks the point of highest electron density in the ionosphere. *hm*F2 has also proven to be a valuable source for deriving the neutral wind at mid latitudes (Dyson et al., 1997; Miller et al., 1986; Richards, 1991). For many years the IRI model relied for its *hm*F2 model on the CCIR model (see Section 3.2.1) for the propagation factor *M*(3000)F2 and on the close correlation between *hm*F2 and *M*(3000)F2 (Bilitza & Eyfrig, 1978; Bilitza et al., 1979; Dudeney, 1983; Shimazaki, 1955). *M*(3000)F2 is defined as *MUF*(3000)F2/*fo*F2, where *MUF*(3000)F2 is the highest frequency that, refracted in the ionosphere, can be received at a distance of 3,000 km.

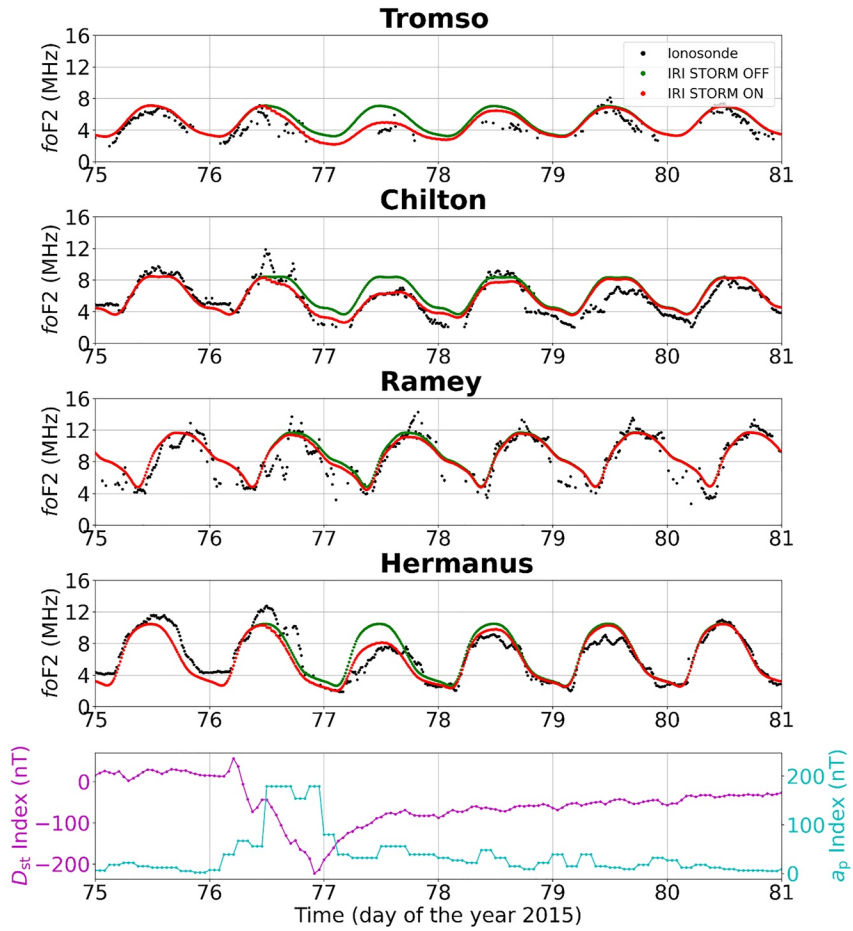

Figure 4. Time series of *fo*F2 at Tromsø (69.60°N, 19.20°E), Chilton (51.50°N, 359.40°E), Ramey (18.50°N, 292.40°E), and Hermanus (34.42°S, 19.22°E) as (black) measured by the ionosondes and modeled by IRI with (red) the IRI STORM option ON and (green) the IRI STORM option OFF, from 16 to 21 March 2015. The bottom panel shows (cyan) the a_p and (purple) D_{st} geomagnetic indices.

Like *fo*F2, *M*(3000)F2 is routinely scaled from ionograms and therefore a large database exists for this parameter covering several solar cycles.

However, limitations of the *M*(3000)F2 approach for *hm*F2 modeling have been highlighted in several studies (Abdu et al., 2010; Adeniyi et al., 2003; Araujo-Pradere et al., 2013; Bilitza, 1985a; Brum et al., 2011; Ezquer et al., 2014; Lee & Reinisch, 2006; Magdaleno et al., 2011). The main causes for these shortcomings are: (a) the limited data set available at the time of the CCIR model development; (b) limitations in representing small scale diurnal features because only a fourth order harmonic expansion is used for the CCIR-*M*(3000)F2 model; (c) the uncertainty introduced with the formula describing the relationship between *hm*F2 and *M*(3000)F2 because it is just an approximation depending on several assumptions. Finally, the use of an *M*(3000)F2-based model makes it very difficult to assimilate measured *hm*F2 values into the IRI model for a real-time updating.

Because of these limitations of the IRI *hm*F2 model, the IRI group had given high priority to the development of new *hm*F2 models and this led to a renewed community-wide focus on modeling this important quantity (Altadill et al., 2013; Brunini et al., 2013; Gulyaeva et al., 2008; Hoque & Jakowski, 2012; Shubin et al., 2013; M.-L. Zhang et al., 2009); the two most recent ones were considered the most mature and were introduced in IRI as new options and will be explained in more detail in the next sections. In addition to these models, which represent the quiet time behavior of *hm*F2, there were also studies that developed first-order descriptions of the *hm*F2 behavior under disturbed conditions; among these the very promising models by Blanch and Altadill (2012) and Gulyaeva (2012) based respectively on digisonde data from the Ebro station in Spain and topside sounder data

from ISIS, Intercosmos 19, and COSMOS-1809. They are under consideration after sufficient testing for future inclusion in the IRI model.

The current IRI model includes three options for modeling *hm*F2: BSE-1979, AMTB2013, and SHU-2015 developed respectively with *M*(3000)F2 ionosonde data (Bilitza et al., 1979; CCIR, 1967), with *hm*F2 ionosonde data (Altadill et al., 2013), and with *hm*F2 ionosonde data and COSMIC RO data (Shubin, 2015; Shubin et al., 2013). The most striking difference between the BSE-1979 option and the AMTB2013 and SHU-2015 options is that the latter ones can predict the well-observed sharp evening peak at low latitudes while BSE-1979 cannot predict this characteristic behavior because of the limited diurnal resolution of the CCIR-*M*(3000)F2 model (Bilitza et al., 2017).

3.3.1. The BSE-1979 Option

The BSE-1979 *hm*F2 model was developed by Bilitza et al. (1979) and is based on the anti-correlation between *hm*F2 and the propagation factor *M*(3000)F2 that was first discussed by Shimazaki (1955). From the definition of *M*(3000)F2 it is clear that the relationship between *hm*F2 and *M*(3000)F2 depends on the distribution of ionization below the F2 peak. Functional descriptions of the relationship have relied on the ratio *fo*F2/*fo*E to characterize this distribution. Bilitza et al. (1979), however, showed that this is not sufficient and that differences in distribution due to magnetic latitude and solar activity have also to be considered. With the help of *hm*F2 values measured by the ISRs in Millstone Hill, Arecibo, and Jicamarca, they established the following empirical relationship

$$hmF2 = \frac{1490}{M(3000)F2 + DM} - 176, \tag{10}$$

where the correction factor *DM* is

$$DM = \frac{f_1 \cdot f_2}{\left(\frac{foF2}{foE} - f_3\right)} + f_4, \tag{10a}$$

and the functions *f* depend on solar activity (12-month running mean of sunspot number R_{12}) and on the magnetic dip latitude Ψ

$$f_1 = 0.00232 R_{12} + 0.222, \tag{10b}$$

$$f_2 = 1 - \frac{R_{12}}{150}\exp\left[-\left(\frac{\Psi}{40}\right)^2\right], \tag{10c}$$

$$f_3 = 1.2 - 0.0116\exp\left(\frac{R_{12}}{41.84}\right), \tag{10d}$$

$$f_4 = 0.096\frac{R_{12} - 25}{150}. \tag{10e}$$

M(3000)F2 is obtained with the CCIR model which uses the same formalism as described for *fo*F2 in Section 3.2.1. For *M*(3000)F2 the CCIR model uses a fourth order expansion for the diurnal harmonics and a total of 49 functions and coefficients for the description of the longitude-latitude structure. The variation with solar activity is modeled by assuming a linear dependence on R_{12} between and beyond the global models provided at $R_{12} = 0$ and $R_{12} = 100$. CCIR modeling has focused on *M*(3000)F2 rather than *hm*F2, because obtaining *hm*F2 from ionograms requires a more complex analysis involving the scaling and inversion of the ionogram traces (e.g., Reinisch & Huang, 1983).

One additional problem of this approach is the fact that *hm*F2 is explicitly dependent on R_{12}, through f_1, f_2, f_3, and f_4 and at the same time, is also implicitly dependent on R_{12} through *M*(3000)F2 and *fo*E. The presence of *fo*F2 in the *DM* factor (Equation 10a) makes *hm*F2 implicitly dependent also on the ionospheric index IG_{12}. This makes it very difficult to adjust *hm*F2 to a measured (real-time) *hm*F2 value with an "effective" solar index; an approach that has been widely and successfully applied to *fo*F2.

Though Equation 10 captures reasonably well the main trends of the quiet-time *hm*F2, it cannot capture the features of small spatial and relative short time scales (e.g., Adeniyi et al., 2003; Oyeyemi et al., 2007) due to the limitations of the CCIR-*M*(3000)F2 model.

Furthermore, during the recent exceptionally low solar minimum conditions (years 2008–2009) the IRI model no longer produced realistic *hm*F2 values because the ratio *fo*F2/*fo*E reached very low values. A lower limit of 1.7 was introduced for this ratio to avoid unrealistically low *hm*F2 values.

3.3.2. The AMTB2013 Option

The AMTB model (Altadill et al., 2013) is based on data recorded from 26 digisonde stations from the Global Ionosphere Radio Observatory (GIRO) network (http://giro.uml.edu; Reinisch & Galkin, 2011) for the time period 1998–2006. Specifically, Altadill et al. (2013) considered monthly averages of electron density profiles measured by digisondes according to the Monthly Averaged Representative Profile (MARP) method proposed by X. Huang and Reinisch (1996). To obtain the MARPs, the individual profiles of a given station for a given month have been binned for the same UT at hourly sampling. Therefore, each MARP represents the quiet-time ionospheric condition of the month for a given UT and station. Then, the *hm*F2 obtained by these MARP profiles were considered as representative of a quiet ionosphere and modeled through a spherical harmonic analysis, that is

$$hmF2(\vartheta,\phi,T)=\sum_{n=0}^{N}\sum_{m=0}^{n}P_n^m(\cos\vartheta)\left\{g_n^m(T)\cos(m\cdot\phi)+h_n^m(T)\sin(m\cdot\phi)\right\}, \tag{11}$$

where ϑ and ϕ are the geocentric spherical coordinates colatitude and longitude, respectively; $P_n^m(\cos\vartheta)$ are the Legendre polynomials of degree n and order m. The seasonal and solar activity variations of *hm*F2 are included in the model through the Gauss coefficients $g_n^m(T)$ and $h_n^m(T)$ which are explained in the next paragraph (see Equation 11a). The spherical harmonic technique requires a good distribution of the data source to provide a good modeling output; since the digisonde longitude coverage was poor, Altadill et al. (2013) assumed that the ionosphere under quiet conditions remains approximately the same over a given day and, since the Earth rotates 360° under a Sun-fixed system, they considered the local time differences to be equivalent to longitude differences. Under this approximation, they defined 24 fictitious stations distributed in longitude every 15° along the latitudinal parallel on which the true station was located. They tested several latitude systems and based on their results, decided on the modified dip (modip) latitude. To capture the sharp increase of *hm*F2 values at low and equatorial latitudes related to the $\mathbf{E}\times\mathbf{B}$ drift (where $\mathbf{E}$ is the zonal ionospheric electric field characterizing low latitudes and $\mathbf{B}$ the geomagnetic field), they set to 8 the maximum degree N of the latitudinal expansion, while the maximum order of m, related to the longitudinal (and inherent local time) dependence, was set to 4. This restricting to four diurnal harmonics is one of the shortcomings of the model because it does not fully represent small scale features like the well-known evening peak of *hm*F2 at low latitudes.

The seasonal variation of *hm*F2 is considered through a two-degree Fourier expansion of the Gauss coefficients (annual and semi-annual variations) as a function of the month of the year ($T=[1,\ldots,12]$) and the coefficients of the Fourier expansion are linearly related to the 12-month running mean sunspot number R_{12}, used as a proxy of the solar activity variation (Altadill et al., 2013)

$$\begin{Bmatrix} g_n^m(T) \\ h_n^m(T) \end{Bmatrix}=\sum_{q=0}^{2}\begin{Bmatrix} ga_{n,q}^m(R_{12}) \\ ha_{n,q}^m(R_{12}) \end{Bmatrix}\cos\left(\frac{2\pi\cdot q\cdot T}{12}\right)+\begin{Bmatrix} gb_{n,q}^m(R_{12}) \\ hb_{n,q}^m(R_{12}) \end{Bmatrix}\sin\left(\frac{2\pi\cdot q\cdot T}{12}\right). \tag{11a}$$

Summarizing, the spherical harmonic model for *hm*F2 is represented by 1220 coefficients. Compared to the old IRI-2007 model (Bilitza & Reinisch, 2008), the AMTB model improved the *hm*F2 modeling by 10% on average and by up to 30% at high and low latitudes.

3.3.3. The SHU-2015 Option

The Satellite and Digisonde Model of the F2 layer (SDMF2) model was developed by Shubin et al. (2013) and then extended by Shubin (2015). Similar to the AMTB model described in the previous section, the SDMF2 model employs a spherical harmonic expansion to model measured *hm*F2 values. The model is based on RO data from the CHAMP (years 2001–2008), GRACE (years 2007–2011), and COSMIC (years 2006–2012) satellite

missions and data from 62 digisondes for the years 1987–2012. RO data were filtered to eliminate unrealistic and clearly wrong profiles as described by Shubin (2015) removing about 10% of the RO *hm*F2 data.

A problem faced by the SDMF2 developers was the uneven distribution in solar activity characterizing their data set. The low solar activity subset is much larger than the high solar activity one. This was partially compensated by filling out data empty months of the high solar activity subset with seasonal averages. All the measured data were then grouped according to their geographic location in bins sized 15° in longitude and 15° in modip, and inside each bin the median value of *hm*F2 was considered. The spatial decomposition characterizing the model is

$$hmF2\,(\phi,\mu,\mathrm{UT}_i)=\sum_{m=0}^{M}\sum_{l=m}^{L}\left[g_i^m\,(\mathrm{UT}_i)\cos(m\cdot\phi)+h_l^m\,(\mathrm{UT}_i)\sin(m\cdot\phi)\right]P_m^l(\cos\vartheta), \tag{12}$$

where ϕ is the geographic longitude, μ is the modip, UT_i is the universal time in integer hours (i = 0,…,23), ϑ is the co-modip latitude ($\vartheta = 90° - \mu$) and ${P_m}^l(\cos\vartheta)$ are the Legendre polynomials. The maximum order in geographic longitude (M) is set to 8, while the maximum order in modip (L) is set to 12. The dependency of *hm*F2 on the $F10.7_{81}$ index (the 81-day running mean of the daily solar index $F10.7_{\mathrm{d}}$) is assumed to be logarithmic, which helps to account for the observed saturation effect of *hm*F2 at high solar activity conditions. Model coefficients were determined for each hour, for each month and for two levels of solar activity, resulting in a total of 85,824 coefficients. For each month data-set-specific $F10.7_{81}$ values were used as the margins for the low ($F10.7_{81} < 80$) and the high ($F10.7_{81} > 120$) solar activity levels. Moreover, a continuous UT variation was determined for each month by fitting a Fourier expansion of order 3 to the hourly model values.

Evaluating their model and the IRI BSE-1979 option with an independent data set, that is digisonde data from the solar activity range of $80 < F10.7_{81} < 120$, Shubin (2015) found an improvement of up to 6% over IRI BSE-1979 with the largest improvements in the South African sector. The SDMF2 model is now the default option in IRI (the SHU-2015 option). Our own evaluation (Figure 5) of all three options with a COSMIC data set selected according to Shaikh et al. (2018) and Pignalberi et al. (2020) shows that the best results are obtained with the SHU-2015 option confirming the results of similar studies by Mengist et al. (2020), H. Huang et al. (2021), and Moses et al. (2021).

3.4. The F2 Bottomside Region

The F2 bottomside region (region (2) in Figure 2) is the part of the electron density profile connecting the F2 layer to the F1 layer and E valley. It was described by Ramakrishnan and Rawer (1972) as:

$$N_{\mathrm{e}}(h)=NmF2\frac{\exp\left(-x^{B_1}\right)}{\cosh(x)}, \tag{13}$$

with

$$x=\frac{hmF2-h}{B_0}, \tag{13a}$$

where N_{e} is the electron density, h the height, *Nm*F2 the F2-peak electron density, *hm*F2 the F2-peak height, and B_0 and B_1 are parameters describing respectively the thickness and shape of the bottomside layer. It can be easily shown that B_0, in fact, is the height difference between *hm*F2 and the height where the electron density has dropped down to 0.24·*Nm*F2. B_1 determines the shape of the profile as illustrated in Figure 6 for some sample B_0 and B_1 values. The larger B_1 the larger are the electron densities right below the F2 peak from *hm*F2 down to (*hm*F2 − B_0). This means that to specify the bottomside profile, B_0 and B_1 are two key parameters as illustrated in Figure 6.

The F2 bottomside region extends to the F1-peak height *hm*F1 if the F1 layer is present; otherwise, it extends to the height *HZ*, which is the upper boundary of the intermediate region (see Figure 2 and Section 3.6).

To represent the global and temporal variations of B_0 and B_1 the IRI model offers three options: Gul-1987 developed by Gulyaeva (1987); Bil-2000 developed by Bilitza et al. (2000); and ABT-2009, developed by Altadill et al. (2009), which is currently the default option. Each one of the three models, which are the subject of the following three subsections, is based on profiles measured by ionosondes. They differentiate in both the

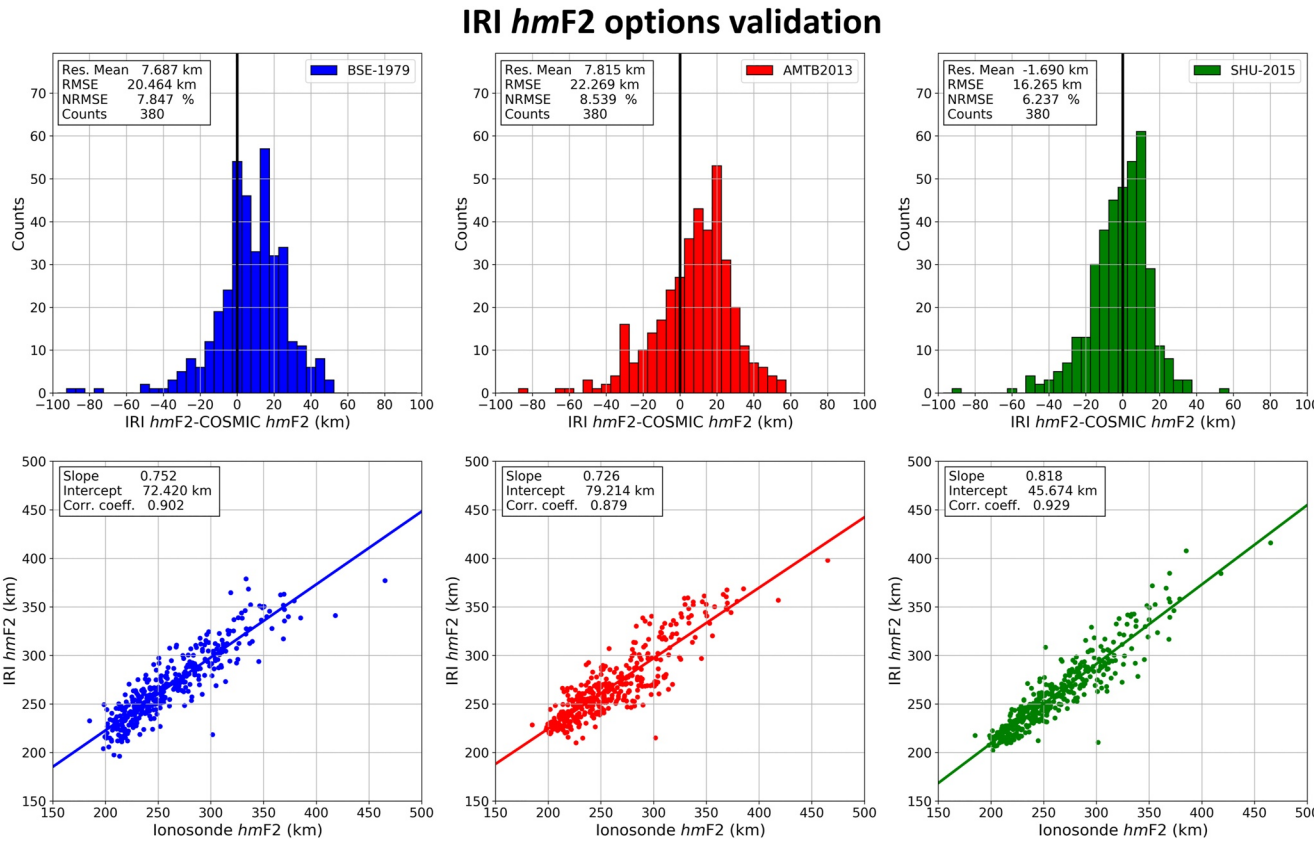

Figure 5. Comparison in terms of histograms of residuals and scatter plots of International Reference Ionosphere *hm*F2 versus Constellation Observing System for Meteorology, Ionosphere, and Climate (COSMIC) values, considering the COSMIC data set selected by Shaikh et al. (2018) and Pignalberi et al. (2020). RMSE stands for root mean square error. NRMSE stands for normalized root mean square error.

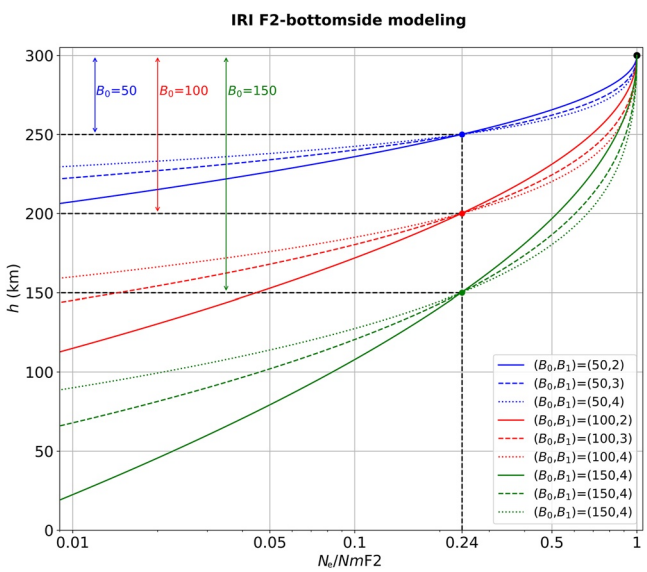

Figure 6. The bottomside function (Equation 13) for different values of B_0 and B_1.

considered ionosonde data set, in terms of volume and coverage, as well as the function used to represent the variation of parameters.

3.4.1. The Gul-1987 Option for B_0 and B_1

Gulyaeva (1987), analyzing a large number of ionograms, recorded at mid latitudes, found a significant correlation between *hm*F2 and the half-density height $h_{0.5}$ defined as the height at which $N_e(h_{0.5}) = 0.5 \cdot NmF2$. She found that the ratio between these two parameters varied from about 0.6 at noon to about 0.8 at night, as a function of the solar zenith angle χ and season, according to the following relation

$$\rho = \frac{h_{0.5}}{hmF2} = 0.8 - 0.2\left[\frac{1}{1+\exp\left(\frac{\chi - 20s}{15}\right)}\right], \tag{14}$$

where s is a seasonal parameter ($s = 1$ for winter, $s = 2$ for equinox, $s = 3$ for summer). To get a smoothly varying parameter, s is approximated as a function of the day of the year (d)

$$s = 2 - \cos\left(\frac{2\pi}{365}d\right). \tag{14a}$$

Solving Equation 13 for the half-density point ($h_{0.5}$, $NmF2/2$) and introducing Gulyaeva's ratio ρ, one obtains the following relationship between B_0 and B_1

Table 4
The B_0 Values in km Used by the Bilitza et al. (2000) Model

		Winter		Spring		Summer		Fall	
|Modip|	R_{12}	LT = 12	LT = 00	LT = 12	LT = 00	LT = 12	LT = 00	LT = 12	LT = 00
0°	10	199	67	201	68	210	61	192	68
0°	100	230	65	240	80	245	83	233	71
18°	10	77	75	108	65	142	81	110	68
18°	100	96	112	124	98	164	100	120	94
45°	10	65	70	78	81	94	84	81	81
45°	100	81	78	102	87	127	91	109	88

$$B_0 = hm\mathrm{F2}\frac{(1-\rho)}{C}, \tag{15}$$

where C is a function of B_1

$$C = 0.3606 + 0.2546B_1 - 0.0548B_1^2 + 0.0046B_1^3, \tag{15a}$$

and B_1 is described in the same way as for the Bil-2000 option that will be explained in the next section.

3.4.2. The Bil-2000 Option for B_0 and B_1

The earliest representation of B_0 in IRI consisted of a table of values that were deduced from monthly averages of ionosonde measurements at a typical low- (Mexico City; modip = 18) and mid-latitude (Lindau, Germany; modip = 45) station providing B_0 values for day and night, all seasons, and low and high solar activity (R_{12} = 10 and 100) (Ramakrishnan & Rawer, 1972). For intermediate times and location an interpolation scheme is employed as described by Bilitza (1990). For the diurnal variation IRI assumes a smooth transition from a constant daytime value to a constant nighttime value and this diurnal pattern is modeled with Epstein step functions at sunset and sunrise (function HPOL, Equation A8 in Appendix A). The Booker (1977) approach (Booker function, Equation A7 in Appendix A) is used to represent the modip variation assuming linear variation of B_0 in each modip segment with smooth transitions at the modip boundaries. The modip segments are defined by the segment boundaries at +45°, +18°, −18° and −45°, whereby the hemispherical differences are assumed to be fully represented by the seasonal differences. Above +45° B_0 is kept constant at its +45° value and similarly below −45° B_0 stays at its −45° value. A linear interpolation is used in solar activity. Comparisons with newer ionosonde data have shown significant shortcomings of this model as well as the Gulyaeva (1987) model, in particular at low and equatorial latitudes (Adeniyi & Radicella, 1998; Reinisch & Huang, 1996). To overcome these shortcomings Bilitza et al. (2000) considered a much larger volume of ionosonde data than the two earlier models, including also data from stations near the magnetic equator. Based on these data a new table of values was established (Table 4) which constitutes the Bil-2000 model using the same temporal and spatial interpolation scheme as the earlier model.

Bilitza et al. (2000) found that the most significant variation of the B_1 parameter is from day to night. Nighttime profiles are much flatter than daytime ones. The daytime value is almost constant at $B_1 = 1.9$, while the nighttime value is close to $B_1 = 2.6$ throughout the night. To model this behavior, they applied Epstein step-functions with smoothed 1-hr transitions at sunset and sunrise (function HPOL in Appendix A).

3.4.3. The ABT-2009 Option

Several researchers evaluated the two aforementioned options with the aim to understand which one provided the best results. Different studies (Blanch et al., 2007; H. Chen et al., 2006; Lee & Reinisch, 2006; Lee et al., 2008; Lei et al., 2004; Sethi et al., 2009; Themens et al., 2014; M.-L. Zhang et al., 2008) showed however that both options were characterized by significant shortcomings. Important discrepancies were found in the representation of seasonal and solar activity trends of B_0, with the Bilitza et al. (2000) model generally providing better results during daytime, and the Gulyaeva (1987) model performing better during nighttime.

This is why Altadill et al. (2009) took charge to develop a new model, based on data recorded by 27 ionosondes from 1998 to 2006, to predict B_0 and B_1 at any location between 70°N and 50°S of latitude, at any time. To work with averages of the ionospheric parameters, representative of a quiet ionosphere, they applied the MARP technique introduced by X. Huang and Reinisch (1996). MARP profiles were computed for a given station, month and hour with a percentage of exclusion of 25%, that is, 25% of vertical electron density profiles having the largest deviations compared to the average profile were excluded. The experimental values of B_0 and B_1 were then obtained through a best fitting procedure between the function (Equation 13) and the computed average profiles (Reinisch & Huang, 1998). The spherical harmonic analysis was then the analytical technique chosen for modeling both parameters

$$f(\vartheta,\phi,T)=\sum_{n=0}^{N}\sum_{m=0}^{n}P_n^m(\cos\vartheta)\left\{g_n^m(T)\cos(m\cdot\phi)+h_n^m(T)\sin(m\cdot\phi)\right\}, \tag{16}$$

where ϑ and ϕ are the geocentric spherical coordinates colatitude and longitude, respectively; ${P_n}^m(\cos\vartheta)$ are the Legendre polynomials of degree n and order m. Similar to the AMTB2013 option for *hm*F2 (Section 3.3.2), the seasonal and solar activity variations are included in the model through the Gauss coefficients ${g_n}^m(T)$ and ${h_n}^m(T)$ (see Equation 16a). Given a set of observations, when these are uniformly distributed over the terrestrial globe, to deduce the model is reasonably straightforward. Since a global distribution of ionosonde stations is not available, Altadill et al. (2009) made use of a "zero order" approximation; specifically, similar to their AMTB2013 modelling approach they considered the local time differences to be equivalent to longitude differences. An important issue related to this approach is the choice of the coordinates defining the parallels passing over the location of each original station. Altadill et al. (2009) tested different coordinate systems concluding that magnetic dip coordinates were the best choice for B_0 and geographic coordinates were the best choice for B_1.

Different parameterizations were chosen for B_0 and B_1. The maximum degree of the expansion (N in Equation 16) was set to 6 for both B_0 and B_1, while the maximum order of the expansion for the longitude (m in Equation 16) was set to 4 for B_0, and to 2 for B_1. The time dependence over the year was represented by a two-degree Fourier expansion as a function of the month of the year ($T=[1,\ldots,12]$)

$$\begin{Bmatrix} g_n^m(T) \\ h_n^m(T) \end{Bmatrix}=\sum_{q=0}^{2}\begin{Bmatrix} ga_{n,q}^m(R_{12}) \\ ha_{n,q}^m(R_{12}) \end{Bmatrix}\cos\left(\frac{2\pi\cdot q\cdot T}{12}\right)+\begin{Bmatrix} gb_{n,q}^m(R_{12}) \\ hb_{n,q}^m(R_{12}) \end{Bmatrix}\sin\left(\frac{2\pi\cdot q\cdot T}{12}\right), \tag{16a}$$

to model the annual and semiannual variations, according to the experimental results (e.g., Altadill et al., 2008, 2009, and references therein). Once the definitive sets of Gauss coefficients were obtained, the analytical functions describing the linear dependence of these coefficients on the solar index R_{12} were obtained.

The Altadill et al. (2009) model showed an improvement of up to 32% for B_0 over the Bilitza et al. (2000) model and up to 40% over the Gulyaeva (1987) model and an improvement of up to 20% for B_1.

3.5. The F1 Region

The F1 ledge marks the boundary between the solar-controlled E region below and the highly dynamical F region above. During times of low solar irradiance (night and winter) the F1 is totally submerged in the F2-bottomside region and no longer identifiable in the electron density profile as a separate layer. The F1-layer representation in IRI relies on the F1-peak critical frequency *fo*F1 model proposed by DuCharme et al. (1971, 1973). Using a large amount of ionosonde data, they modeled *fo*F1 as a function of the solar zenith angle χ, the solar activity index R_{12}, and the magnetic latitude coordinate λ

$$foF1=f_s\cos^n\chi, \tag{17}$$

where

$$f_s=f_0+\frac{(f_{100}-f_0)\,R_{12}}{100}, \tag{17a}$$

$$f_0=4.35+0.0058|\lambda|-0.00012\lambda^2, \tag{17b}$$

$$f_{100} = 5.348 + 0.011|\lambda| - 0.00023\lambda^2, \tag{17c}$$

$$n = 0.093 + 0.0046|\lambda| - 0.000054\lambda^2 + 0.0003R_{12}. \tag{17d}$$

DuCharme et al. (1973) tested several magnetic coordinates and found a small advantage when using geomagnetic latitude. However, follow-on work by one of the co-authors (R. Eyfrig) with more low-latitude stations favored the use of magnetic dip latitude Ψ, which describes the close coupling to the magnetic field lines more accurately than λ. Based on his results and recommendation Ψ is used in IRI. In addition to the *fo*F1 value itself the model also includes a criterion for the existence of an identifiable F1 layer. DuCharme et al. (1973) use a critical solar zenith angle χ_s to define the range for which an F1 layer is expected. Only for solar zenith angle lower than χ_s an F1 layer is assumed to be present. χ_s is defined as

$$\chi_s = \chi_0 + \frac{(\chi_{100} - \chi_0)\, R_{12}}{100}, \tag{18}$$

where

$$\chi_0 = 49.847333 + 0.349504|\lambda|, \tag{18a}$$

$$\chi_{100} = 38.96113 + 0.509932|\lambda|, \tag{18b}$$

and here again IRI uses Ψ instead of λ.

Based on their study of ionosonde data from many stations Scotto et al. (1997) introduced a statistical description of the occurrence probability of an F1 layer in terms of the solar zenith angle, solar activity, and magnetic latitude. The F1-layer occurrence probability function P is given as:

$$P(\chi, \lambda, R_{12}) = [0.5 + 0.5\ \cos(\chi)]^{\gamma}, \tag{19}$$

with

$$\gamma = a + b \cdot \lambda + c \cdot \lambda^2, \tag{19a}$$

and

$$\begin{cases} a = 2.98 + 0.0854R_{12}, \\ b = 0.0107 - 0.0022R_{12}, \\ c = -0.000256 + 0.0000147R_{12}. \end{cases} \tag{19b}$$

An F1 layer is added to the IRI electron density profile when the probability P is greater than 0.5. In addition to their standard model, Scotto et al. (1997) also provide a version that includes cases of L-condition. These are cases when the ionogram trace shows an F1 ledge rather than a distinct F1 cusp. They found that with the inclusion of L-condition cases the probability no longer depends significantly on geomagnetic latitude or solar activity. A good representation could be achieved by using a constant value of $\gamma = 2.36$ in Equation 19.

The standard Scotto et al. (1997) model is the recommended IRI default for the F1-layer occurrence probability. Additional options are the older DuCharme et al. (1973) criterion (Equation 18), the Scotto et al. (1997) probability model with L-condition cases included, and a strict omission of the F1 feature independent of the value of P or χ_s. The last option was recently added because of the disruptive effect of the on-off transition of the F1 structure on applications that require a continuous varying electron density profile.

It should be noted that a user can get the F1 occurrence probability P as an additional IRI output parameter. This could benefit applications that need actual probabilities (e.g., percentage of days for which an F1 layer is expected) rather than using only a cutoff criterion (Scotto et al., 1997, 1998).

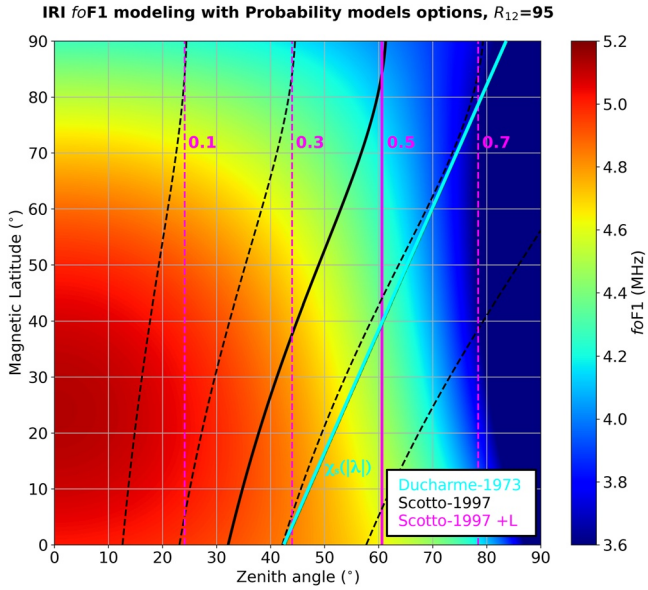

Figure 7. *fo*F1 as a function of the solar zenith angle and the magnetic latitude, for $R_{12} = 95$, according to Equation 17. Superimposed are the curves corresponding to the three options: in cyan the threshold zenith angle given by Equation 18; in magenta and black the probability functions (Equation 19) proposed by Scotto et al. (1997), with and without the L condition respectively (the cut-off curve corresponding to 0.5 is in both cases drawn as a solid curve).

Figure 7 shows *fo*F1, as a function of the solar zenith angle and the magnetic latitude according to Equation 17, for $R_{12} = 95$, and superimposed the curves related to the three options: the threshold zenith angle given by Equation 18; the probability function proposed by Scotto et al. (1997), with and without the L condition. This example illustrates the significant differences that still exist between different models for this parameter, particularly at low latitudes. Noteworthy is also the good agreement between the Ducharme model and the 0.7 probability curve of Scotto et al. (1997) without L conditions.

In addition, Figure 8 shows the F1 occurrence probabilities recorded at the ionospheric station of Rome in 2003 during the June to September time period with and without L-condition cases included, along with the occurrence probabilities given by the three options and a comparison between measured and modeled values.

The F1-layer peak height *hm*F1 is found as the height at which the F2 bottomside profile (Equation 13) reaches the F1-peak density *Nm*F1, that is obtained from *fo*F1 through the formula $NmF1/m^{-3} = 1.24 \times 10^{10} \cdot (foF1/\mathrm{MHz})^2$. Therefore, one should keep in mind that the value of *hm*F1 depends on the choice of the bottomside thickness parameters B_0 and B_1. The F1-layer electron density profile extends from *hm*F1 to the height *HZ* (see region (3) in Figure 2 and Section 3.6) and is represented by the approach proposed by Reinisch and Huang (2000) based on their study of digisonde data. They add the F1 layer to the bottomside profile by using a modified height h^* with the bottomside formulation (Equation 13). h^* is defined as

$$h^* = hmF1 \cdot \left[1 - \left(\frac{hmF1 - h}{hmF1}\right)^{1+C_1}\right]. \tag{20}$$

C_1 is the F1-layer shape factor and varies with modip μ and LT

$$C_1 = 2.5C_{10} \cdot \cos\left[\frac{(LT - 12)}{(SS - SR)}\pi\right], \tag{20a}$$

where

$$\begin{cases} C_{10} = 0.09 + 0.11\mathrm{Eps}_0(|\mu|, 30, 10) & \text{if } |\mu| \geq 18, \\ C_{10} = 0.1155 & \text{if } |\mu| < 18, \end{cases} \tag{20b}$$

and SR and SS are the LTs of sunrise and sunset, respectively, with the special conditions: if SR = SS then $C_1 = 2.5 \cdot C_{10}$ and if $C_1 < 0$ then $C_1 = 0$. When the F1 layer is not present $C_1 = 0$, so $h^* = h$, and the profile described by the function (Equation 13) extends all the way down to *HZ*.

3.6. The Intermediate Region

The intermediate region (region (4) in Figure 2) extends from the height *HZ* down to the height h_I which is either the top of the E valley described by the height h_{VT} or the E-peak height *hm*E depending on whether a valley is present or not. This region is the most difficult to model because it merges the F region, which is normalized to the F2-peak parameters, with the E region, which is normalized to the E-peak parameters. The process is made even more complicated by the potential addition of an F1 layer to the bottomside profile and potentially a valley above the E peak. In a first step, the height h_{ST} is determined as the point where the bottomside function (Equation 13) with or without the F1-layer addition has dropped down to the E-peak density *Nm*E. The height *HZ* is then defined as

$$HZ = \frac{(h_{ST} + hF1)}{2}, \tag{21}$$

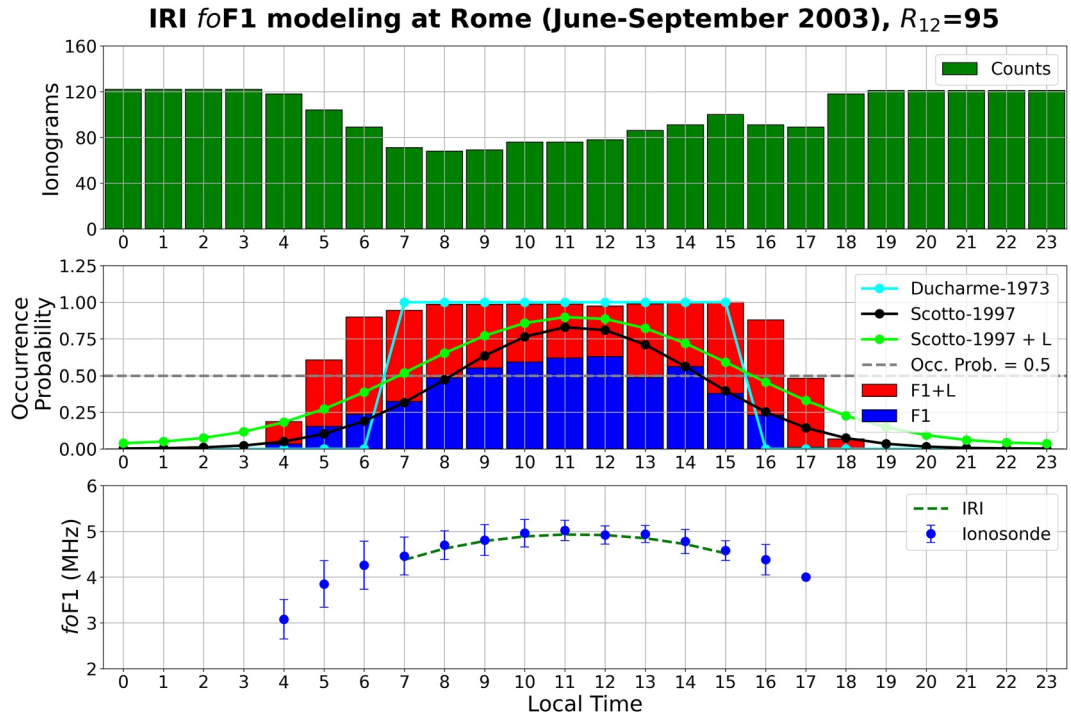

Figure 8. (top panel) Number of hourly ionograms considered to calculate the F1-layer occurrence probability at the ionospheric station of Rome (magnetic latitude 38.8°) between June and September 2013, a period characterized by a mean value of $R_{12} = 95$. (middle panel) F1-layer occurrence probabilities calculated without (in blue) and with (in red) L condition. The three different curves in black, green and cyan correspond to the F1-layer occurrence probabilities given by the three different options. (bottom panel) Comparison between modeled (green dashed curve) and measured (blue dots) *fo*F1 values. Measured data have been manually validated; the dot represents the corresponding hourly median and the vertical line the corresponding standard deviation.

where

$$\begin{cases} hF_1 = hmF1 & \text{if an F1 layer is present,} \\ hF_1 = (hmF2 + h_l)/2 & \text{if an F1 layer is not present,} \end{cases} \tag{21a}$$

and

$$\begin{cases} h_l = h_{VT} & \text{if a valley is present,} \\ h_l = hmE & \text{if a valley is not present.} \end{cases} \tag{21b}$$

Starting from *HZ* the merging with the E-valley top is achieved by a parabolic downward/upward bending of the bottomside profile such that it meets the valley top or *hm*E: downward, if h_{ST} is found above h_l; upward if h_{ST} is found below h_l. This transformation of the height range $HZ - h_{ST}$ into the height range $HZ - h_l$ is done by introducing the modified height h^{**} into the F2 bottomside formulation (Equation 13) as described by Reinisch and Huang (2000).

$$h^{**} = hmF1 \cdot \left[1 - \left(\frac{hmF1 - \eta}{hmF1}\right)^{1+C_1}\right], \tag{22}$$

with

$$\begin{cases} \eta = h \quad \text{if} \quad h_{ST} = h_{VT}, \\ \eta = HZ + \dfrac{T}{2} - \sqrt{T\left[\dfrac{T}{4} - (h - HZ)\right]} \quad \text{if} \quad h_{ST} > h_{VT}, \\ \eta = HZ + \dfrac{T}{2} + \sqrt{T\left[\dfrac{T}{4} - (h - HZ)\right]} \quad \text{if} \quad h_{ST} < h_{VT}, \end{cases} \tag{22a}$$

where

$$T = \frac{(HZ - h_{ST})^2}{h_{ST} - h_l}. \tag{22b}$$

This makes $h^{**} = h_{ST}$ for $h = h_l$ as required. With this formulation, the same function (Equation 13) is used by IRI for modeling the F2, the F1, and the intermediate regions by using different height definitions (h for the F2 layer, h^* for the F1 layer, h^{**} for the intermediate layer). This approach has been developed to avoid discontinuities and/or artificial valleys when merging different regions.

3.7. The E Region

The E region consists of the E peak, the E-valley region above the peak and the E-region bottomside below the peak. Ionosondes are the main source of information for modeling the E-peak plasma frequency *fo*E and the peak height *hm*E. Incoherent scatter radar observations also contribute to E-peak modeling and are the prime data source for the E-valley region. For the E-region bottomside we have to rely on rocket measurements.

3.7.1. The E-Valley Region

In the region above the E peak a deep valley occurs during nighttime and a shallow valley is often observed during daytime primarily at mid latitudes. The balance of ionization gain and loss processes is responsible for the valley shape and existence. Plasma redistribution due to neutral wind and $\mathbf{E} \times \mathbf{B}$ forcing also play a role. In IRI a fifth order power series is used to describe the profile from the E peak to the valley top (region (5) in Figure 2)

$$N_e(h) = NmE \cdot \left(1 + E_1 x^2 + E_2 x^3 + E_3 x^4 + E_4 x^5\right), \tag{23}$$

with $x = h - hmE$. For the deep and wide valley that develops during nighttime an exponential representation had to be introduced

$$N_e(h) = NmE \cdot \exp\left(1 + E_1 x^2 + E_2 x^3 + E_3 x^4 + E_4 x^5\right). \tag{23a}$$

The coefficients are determined such that the function peaks at *hm*E, has only one minimum in the valley range and satisfies the following predefined valley parameters:

$$HBR = h_{VT} - hmE, \tag{23b}$$

the valley width;

$$DP = 100\frac{\left(NmE - N_{e,VB}\right)}{NmE}, \tag{23c}$$

the valley depth in percentage, where $N_{e,VB}$ is the electron density at the valley base height h_{VB};

$$HABR = h_{VB} - hmE, \tag{23d}$$

the distance between the valley base and *hm*E;

$$DLN = \frac{d \ln N_e}{dh}|_{h=h_{VT}}, \tag{23e}$$

the logarithmic derivative at the valley top.

Table 5
Valley Parameters

		HABR (km)	HBR (km)	DPI (%)	DLN (km^{-1})
Nighttime	Modip = 18	28	45	81	0.06
	Modip = 45	28	67	81	0.06
Daytime	Modip = 18	0	0	0	0
	Modip = 45	10.5	17.8	Winter: 10 Else: 5	Summer: 0.01 Else: 0.016

It is not possible to measure these valley parameters with ionosondes, because the real-height analysis of ionogram traces has to rely on a priori information regarding the existence or non-existence and size of an E valley (Gulyaeva et al., 1990). Therefore, we depend on data obtained with rocket flights or with ISR for establishing the spatial and temporal variation of these parameters. IRI uses the parameters listed in Table 5, which are based on data from the ISR stations Malvern, St. Santin, Millstone Hill, and Arecibo (Bilitza, 1990).

At low and equatorial latitudes, the valley feature has been observed irregularly during daytime but not frequent enough to be included in a monthly average profile (Mahajan et al., 1990). For nighttime the compilation and study of Japanese rocket data by Maeda (1969, 1971) provided additional information. Aeronomical calculations by Titheridge (1990) show good agreement with the IRI valley parameters. Epstein step functions (Eps_0 in Appendix A) are used to obtain a continuous variation of the valley parameters (*VP*) with modip

$$\begin{cases} VP = VP(\mu = 18) + [VP(\mu = 45) - VP(\mu = 18)]\mathrm{Eps}_0(|\mu|;30,10) \ \text{ for } \ |\mu| > 18, \\ VP = VP(\mu = 18) \ \text{ for } \ |\mu| < 18, \end{cases} \tag{24}$$

The local time variation assumes constant daytime and nighttime values with smooth transitions at sunset and sunrise using the function HPOL (Equation A8 in Appendix A).

In the case of $DP = 0$ (no valley) the bottomside or F1-layer function is merged all the way down to the E-peak height *hm*E.

3.7.2. The E-Peak Plasma Frequency *fo*E, Density *Nm*E, and Height *hm*E

Concerning *Nm*E, IRI represents the E-peak critical frequency *fo*E (from which *Nm*E is obtained through the plasma frequency formula [Equation 7]) according to the model developed by Kouris and Muggleton (1973) and Muggleton (1975) and used by CCIR (1975). Their model is based on a large volume of ionosonde data (55 stations, 1944–1973) and consists of four factors

$$f o\mathrm{E}^4 = A \cdot B \cdot C \cdot D; \tag{25}$$

factor *A* describes variations with solar activity using the index $F10.7_{365}$, which is the centered 365-day running average of the daily *F*10.7 index

$$A = 1 + 0.0094\,(F10.7_{365} - 66)\,; \tag{25a}$$

B describes the changes with season and depends on the noontime solar zenith angle χ_{noon} and geographic latitude φ

$$B = \cos^m \chi_{\mathrm{noon}}, \tag{25b}$$

$$m = \begin{cases} -1.93 + 1.92\,\cos\,\varphi & \text{for } \ |\varphi| < 32^\circ \\ 0.11 - 0.49\,\cos\,\varphi & \text{for } \ |\varphi| \geq 32^\circ \end{cases}; \tag{25c}$$

C is the main latitude factor

$$C = \begin{cases} 23 + 116\,\cos\,\varphi & \text{for } \ |\varphi| < 32^\circ \\ 92 + 35\,\cos\,\varphi & \text{for } \ |\varphi| \geq 32^\circ \end{cases}, \tag{25d}$$

and *D* describes variations during the day

$$D = \cos^n \chi_a, \tag{25e}$$

$$n = \begin{cases} 1.2 & \text{for } |\varphi| > 12° \\ 1.31 & \text{for } |\varphi| \le 12° \end{cases}. \tag{25f}$$

Rawer and Bilitza (1990) modified the CCIR (1975) representation by introducing the adjusted solar zenith angle χ_a

$$\chi_a = \chi - 3 \ln \left[1 + \exp \left(\frac{\chi - 89.98}{3} \right) \right], \tag{26}$$

instead of χ in Equation 25e, to better represent observations obtained by the Arecibo ISR during dawn and dusk.

This approach was confirmed by Bradley (1994) with data from the Malvern ISR. The twilight and nighttime periods are difficult to model because of the scarcity of reliable data due to the very low densities. A number of values and formulas have been proposed for the nighttime minimum foE_{min}. An excellent review of the different proposals for the nighttime value as well as the twilight variation was presented by Bradley (1993). IRI uses the minimum value

$$(foE_{min})^2 = 0.121 + 0.0015\,(F10.7_{365} - 60)\,, \tag{27}$$

which is based on a study by Rawer and Bilitza (1990) using Arecibo ISR data.

For the E-peak height, *hm*E, IRI assumes a constant value that was increased from 105 km in earlier versions to now 110 km based on input from ionosonde and ISR observations. During daytime Chapman theory predicts a small variation with solar zenith angle (Nicolls et al., 2012; Titheridge, 2000), however direct observational evidence is scarce and almost non-existing for nighttime. The theoretical modeling of Titheridge (2000) and the assimilative modeling by Nicolls et al. (2012) find overall good agreement with the IRI *fo*E/*Nm*E and *hm*E values. A few examples of global *fo*E maps are shown in Figure 9 indicating the changes with season and solar activity.

The global morphology of these maps agrees well with those obtained by Nicolls et al. (2012) by assimilating COSMIC RO vTEC data into the Ionospheric Data Assimilation Four-Dimensional (IDA4D) algorithm. Titheridge's (2000) model calculations point to a potential shortcoming of the IRI predictions of *fo*E near the poles (underestimating *fo*E for $\varphi > 70°$) and also note the somewhat arbitrary inflection point that is introduced at $\varphi = 32°$ by the change in the analytic formalism of CCIR (1975).

Very thin layers of high electron density, much higher than *Nm*E, can occur sporadically in the E region and cause problems for communication and navigation systems. These so-called sporadic-E (Es) layers are caused by long-lived metallic ions of meteoric origin that the wind shear in this region accumulates into thin ionization sheets. At middle latitudes this is mostly a summer phenomenon, which is in accordance with the higher meteor activity during this season and also with the stronger semi-diurnal tide during the summer. Numerical maps of the critical frequency of the Es ordinary mode of propagation, *fo*Es, were prepared by Leftin et al. (1968) and Smith (1976) based on ionosonde data. But these models have not been widely accepted and used because of the irregular global distribution of stations and the insufficient data volume. More recently, analysis of data from COSMIC, CHAMP and GRACE has provided a much better global picture of the occurrence and magnitude of *fo*Es (Arras et al., 2008) with the promise of future development of *fo*Es occurrence models for IRI.

3.7.3. The E Bottomside Region

The region right below the E peak is characterized by a steep gradient that is described in IRI by an exponential function normalized to the E-peak density *Nm*E and height *hm*E

$$N_e(h) = NmE \cdot \exp\left[-D_1 \cdot (hmE - h)^K\right]. \tag{28}$$

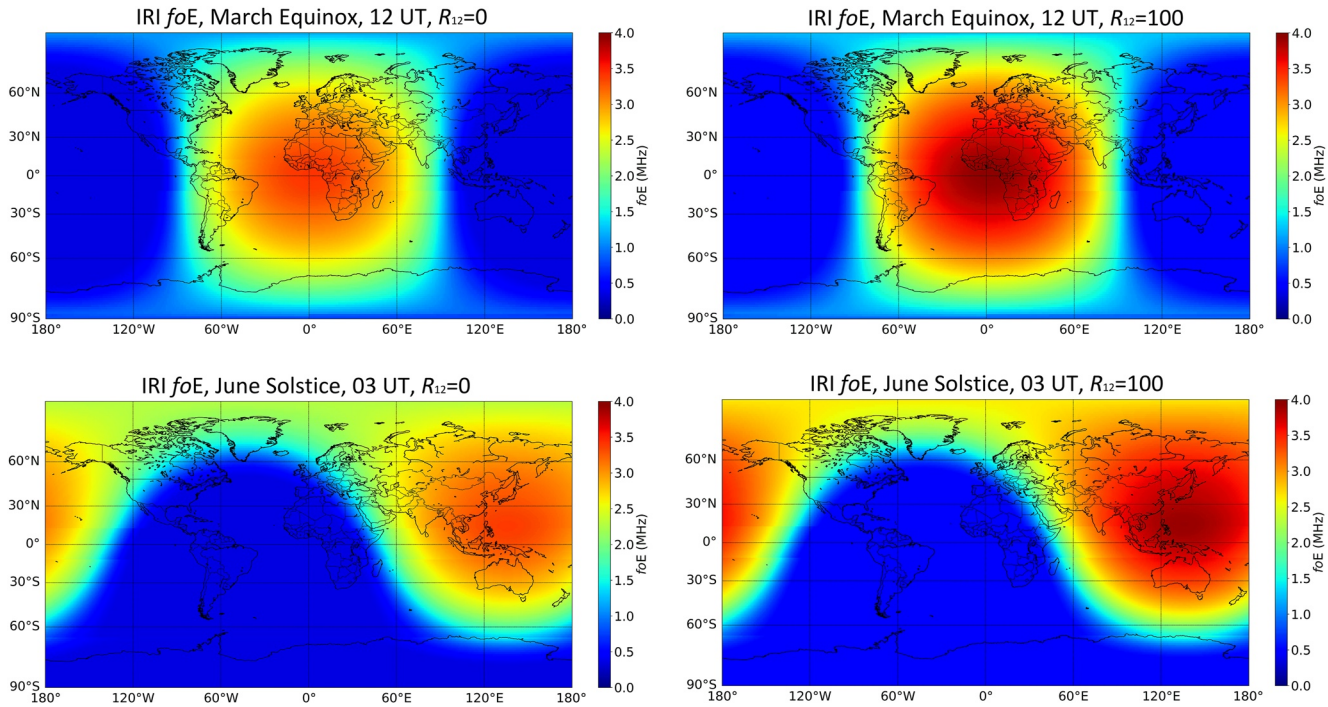

Figure 9. Global maps of *fo*E obtained in (upper panels) March at 12 UT and (lower panels) June at 03 UT for $R_{12} = 0$ (left panels) and $R_{12} = 100$ (right panels).

The parameters D_1 and K are determined such that the bottomside profile (Equation 28) matches with the D-region profile (Equation 30) and its first derivative at an intermediate height *HDX* (see Figure 2)

$$K = -\frac{DN \cdot (hmE - HDX)}{NDX \ln\left(\frac{NDX}{NmE}\right)}, \tag{28a}$$

$$D_1 = \frac{DN}{NDX \cdot K \cdot (hmE - HDX)^{K-1}}, \tag{28b}$$

where *NDX* is the electron density at *HDX* and *DN* is the electron density derivative at that height. If the exponent K is larger than 5, then K will be set to 5 and D_1 will be determined such that the point *HDX*/*NDX* is reached. This helps to avoid unrealistic profiles, but the derivative is no longer continuous at *HDX*. Comparisons with high frequency (HF) radio wave observations seem to indicate that IRI underestimates the steep gradient in this region (Ferguson & McNamara, 1986). But these observations have their own accuracy problems and a rigorous study with reliable rocket data is still outstanding. One should also keep in mind that a lowering of the E-peak height also produces a sharper gradient in this region.

3.8. The D Region

This region is too low for satellite in situ observations and the densities are too low for reliable measurements from the ground. Therefore, rocket data are the main source for data-based modeling in this region. The long record of ground-based absorption measurements (e.g., Singer et al., 1984) unfortunately provides only indirect evidence and depends strongly on the underlying assumptions about the collision frequencies (Serafimov et al., 1985). Propagation of VLF radio signals in the ground-to-bottom-of-ionosphere waveguide is another indirect technique for deducing D-region densities (Siskind et al., 2018). Scarcity of reliable data remains one of the main problems for D-region modeling. IRI includes three different model options that were developed based on different sets of rocket data and additional information: (a) Bilitza (1981a); (b) Friedrich and Torkar (2001); and

Table 6
D-Region Parameters

Time	Geographic latitude	*hm*D (km)	h_{nea} (km)	F_1 (km)	F_2 (km^2)	F_3[a] (km^3)	F_3[b] (km^3)	*HDX* (km)
Day	Low	81	65	0.02	-2×10^{-4}	9.37×10^{-3}	4.89×10^{-4}	85.6
	Middle	81	65	0.05	-1.25×10^{-3}	8.18×10^{-3}	1.707×10^{-4}	85.6
Night	All	81	65	0.05	-1.25×10^{-3}	8.79×10^{-3}	1.22×10^{-2}	92.5

Friedrich et al. (2018); (c) Danilov et al. (1991, 1995). The data foundation of the Friedrich and Torkar (2001) model and the Danilov et al. (1991) model consists of over 100 rocket soundings while Bilitza (1981a) relied on two dozen typical rocket profiles selected by Mechtley and Bilitza (1974). Only the Bilitza (1981a) model is connected to the rest of the IRI electron density profile. The other two models are not merged with the IRI profile and thus can only be used for studies that are confined to the region below the E peak. The Danilov et al. (1995) model has the added benefit that it considers the considerable influence of meteorological forcing from below. The Friedrich and Torkar (2001) model, also called Faraday IRI (FIRI) model in the literature, was recently updated to FIRI-2018 by Friedrich et al. (2018). By comparing the three options, an IRI user can get an indication of the still existing uncertainties in this region of the ionosphere.

3.8.1. The Bilitza (1981a) Model

The typical D-region electron density profile exhibits a characteristic inflection point that is, related to the transition from molecular ions to cluster ions as the dominant ions. Bilitza (1981a) used this inflection point as anchor point for the D-region profile and determined the parameters of this point and of the whole D-region profile based on the compilation of rocket data from radio wave propagation experiments selected by Mechtley and Bilitza (1974) as most reliable. The inflection point is typically found at a height *hm*D of 81 km during daytime and 88 km during nighttime. The function HPOL Equation A8 in Appendix A is used to provide a smooth transition at the D-region sunrise and sunset. For the electron density *Nm*D at the inflection point, Bilitza (1981a) found a strong dependence on the solar zenith angle χ and a weak dependence on solar activity index R_{12}

$$NmD = (6.05 + 0.088R_{12}) \cdot 10^8 \cdot \exp\left(-\frac{0.1}{\cos^{2.7}\chi}\right). \quad (29)$$

For nighttime, the reliable database is extremely limited. Bilitza (1981a) recommends a typical value of $4{\cdot}10^8$ el/m^3. If the daytime value (Equation 28) drops below this minimum value it is set to $4{\cdot}10^8$ el/m^3 as well. The D-region electron density profile from the IRI starting height h_{nea} upward is represented by a third order polynomial:

$$N_e(h) = NmD \cdot \exp\left(F_1 x + F_2 x^2 + F_3 x^3\right), \quad (30)$$

with $x = h - hmD$. The coefficients F_1, F_2, and F_3 are specified in Table 6. They were determined based on fits to the rocket profiles presented by Mechtley et al. (1972) and Mechtley and Bilitza (1974). Different values of the coefficient F_3 are used above and below the inflection point (*hm*D, *Nm*D) to account for the significant change in scale height at *hm*D. An Epstein step function is used for a continuous variation in latitude during daytime and the HPOL function for the smooth transition from day to night values (see Appendix A for a description of Eps_0 and HPOL). In the online interface, this option is referenced as IRI-95.

3.8.2. The FIRI Model

This option refers to the semi-empirical model of the lower, non auroral, ionosphere that was developed by Friedrich and Torkar (2001) and recently updated by Friedrich et al. (2018). They inspected data from 811 rocket flights that carried radio wave propagation experiments (Faraday rotation and/or differential absorption techniques) or Langmuir probes (LPs). A total of 327 profiles remained after excluding data from auroral zone launches and from disturbed time periods (storms, winter anomaly, solar eclipse). These data were then used to correct their theoretical ion-chemical model (Torkar & Friedrich, 1983). For each of the considered 327 measured electron density profiles, they calculated at each kilometer the difference between the logarithm of the measured and theoretical profiles and modeled this correction term *R* as

$$R = a_1 + a_2 \cdot \ln(\mathrm{Ch}\chi) + a_3 \cdot \cos\varphi + a_4 \cdot \ln(\mathrm{Ch}\chi) \cdot \varphi \cdot \sin\frac{\pi(80 + \mathrm{day})}{182.75} + a_5 \cdot F10.7_\mathrm{d} \cdot \ln(\mathrm{Ch}\chi) \cdot \cos\varphi, \quad (31)$$

where Ch is the Chapman function (Rishbeth & Garriott, 1969), χ is the solar zenith angle, φ the geographic latitude, and $F10.7_\mathrm{d}$ the daily solar flux index. Specifically, they found at each kilometer of altitude those values of coefficients a_1, a_2, a_3, a_4 and a_5 that give the best agreement between the input electron densities and the corresponding modeled values. The FIRI model is included into IRI in the form of tables of values which provide the logarithm of D-region electron density from 60 to 150 km in steps of 1 km (81 values) for 5 values of latitude (φ = 0°, 15°, 30°, 45°, 60°), for all 12 months, for 11 values of solar zenith angle (χ = 0°, 30°, 45°, 60°, 75°, 80°, 85°, 90°, 95°, 100°, 130°), and for 3 level of solar activity ($F10.7_\mathrm{d}$ = 75, 130, 200). The electron density for specific conditions is obtained by linear interpolation between these values. The region above 100 km is well reproduced, but requires the largest correction of the theoretical model. The largest prediction errors are found in the mesopause region (80–90 km) which could be caused by the onset of appreciable atomic oxygen and/or meteoric dust. Also the well-known diurnal asymmetry between pre-noon and post-noon hours is strongest in this region. Xu et al. (2021) presented a parameterization of the FIRI model that simplifies its application for transionospheric VLF simulations.

3.8.3. The Danilov et al. (1995) Model

Also included in IRI is the D-region model developed by Danilov et al. (1991, 1995) that is based on data from over 100 mostly Russian rocket flights (Danilov & Smirnova, 1994). The model describes variations with solar zenith angle, season, solar activity ($F10.7_\mathrm{d}$), and magnetic activity (3-hr K_p). It can also describe the effects a weak or strong stratospheric warming (SW) and a weak or strong winter absorption anomaly (WA) have on the D-region electron density. Model values are provided at the altitudes h_i = 60, 65, 70, 75, 80, 85, and 90 km by the formula

$$\log(N_\mathrm{e}(h_i)) = A_i + B_i \cdot f1\mathrm{z} + C_i \cdot f2K\mathrm{p} + D_i \cdot f3\mathrm{F} + E_i \cdot f4\mathrm{S} + F_i \cdot f5\mathrm{SW} + \mathrm{G}_i \cdot f6\mathrm{WA} \quad (32)$$

with the functions

$$f1\mathrm{z} = \begin{cases} 1 & \text{for } \chi < 45° \\ 1.1892 \cdot \sqrt{\cos\chi} & \text{for } 45° \le \chi < 90° \\ 0 & \text{for } \chi \ge 90° \end{cases}, \quad (32a)$$

$$f2K\mathrm{p} = \min\left(2,\ 3\text{-hr}\ K_\mathrm{p}\right), \quad (32b)$$

$$f3\mathrm{F} = \frac{(F10.7_\mathrm{d} - 60)}{300} \cdot f1\mathrm{z}, \quad (32c)$$

$$f4\mathrm{S} = \begin{cases} 0 & \text{for summer} \\ 0.5 & \text{for spring and fall} \\ 1 & \text{for winter} \end{cases}, \quad (32d)$$

$$f5\mathrm{SW} = \begin{cases} 0 & \text{no SW} \\ 0.5 & \text{weak SW} \\ 1 & \text{strong SW} \end{cases}, \quad (32e)$$

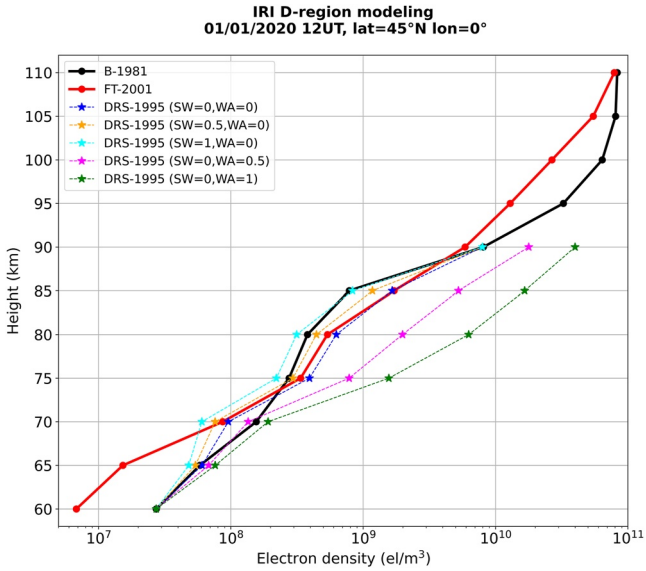

Figure 10. Profiles between 60 and 90 km obtained applying the Bilitza (1981a) model (B-1981), the Friedrich and Torkar (2001) model (FT-2001), and the Danilov et al. (1995) model (DRS-1995) the 1 January 2020 at a latitude of 45° N and a longitude of 0°. Concerning the DRS-1995 model, it can be applied only until an altitude of 90 km, and the following conditions have been considered: SW = 0 and WA = 0; SW = 0.5; SW = 1; WA = 0.5; WA = 1.

$$f6\mathrm{WA} = \begin{cases} 0 & \text{no WA} \\ 0.5 & \text{weak WA} \\ 1 & \text{strong WA} \end{cases} . \quad (32f)$$

The criteria for a weak SW is a temperature increase of 10° at the 30 hPa level and for a strong SW a temperature increase of 20°. A weak WA is identified by an increase of the absorption of 15 dB in the 2–2.8 MHz range and a strong WA by an increase of 30 dB. Both phenomena (SW and WA) occur predominantly in winter and *f*5SW and *f*6WA are therefore set to zero for the other seasons. The coefficients A_i, B_i, C_i, D_i, E_i, F_i, and G_i were determined by fitting the formula (Equation 32) to the rocket data for the specific altitude range. Since the SW and WA criteria parameters may not be readily available to most IRI users, it was decided to provide the electron densities for the 7 altitudes and 5 conditions (SW = 0, WA = 0; SW = 0.5, WA = 0; SW = 1, WA = 0; SW = 0, WA = 0.5; SW = 0, WA = 1) in a special section of the output file. This way a user can get an impression of the effect these phenomena have on the D-region electron density profile.

Figure 10 shows the profiles between 60 and 90 km obtained for the 1 January 2020 applying the three models just described at a latitude of 45° N and a longitude of 0°.

3.9. Extension to the Plasmasphere

Plasmasphere modeling efforts in the framework of IRI have a long history starting with the work of Rycroft & Jones (1987) and of Kimura et al. (1996). Since then a number of empirical plasmasphere models have been developed using different modeling techniques and different data sources. The following models have been proposed as potential candidates for the extension of IRI to plasmaspheric altitudes:

1. The Global Core Plasma Model (GCPM) developed by Gallagher et al. (2000) uses a modular approach with separate models for the plasmasphere, plasmapause, trough, polar cap and IRI for the ionosphere with continuous transitions in value and gradient. It describes the plasma density and composition as a function of the geomagnetic index K_p, the annual mean of solar index $F10.7$, season and position and relies predominantly on data from the Dynamics Explorer (DE)-1 satellite Retarding Ion Mass Spectrometer and Plasma Wave instruments and on the earlier work of Carpenter and Anderson (1992).
2. The IMAGE/RPI plasmasphere model of Ozhogin et al. (2012) is based on more than 700 density profiles along field lines derived from active sounding measurements made by the radio plasma imager (RPI) on the IMAGE satellite (Reinisch et al., 2001) between June 2000 and July 2005. The measurements cover all magnetic local times and vary spatially from $L = 1.6$ to $L = 4$. The model depends on L-shell and magnetic latitude, and provides better agreement with the RPI data than earlier models including the Carpenter and Anderson (1992) and GCPM models. For the polar cap region, a separate power profile model was developed as a function of magnetic activity (Nsumei et al., 2003).
3. The IZMIRAN plasmasphere model, often referred to as IRI-Plas, is based on the work of Chasovitin et al. (1998), Gulyaeva et al. (2002), and Gulyaeva and Titheridge (2006) using topside sounder observations from ISIS-1, -2, and Intercosmos 19. It presents vertical, exponentially varying profiles of electron density in the plasmasphere smoothly fitted to the IRI topside profile at the altitude where the IRI profile reaches half the F-peak density. The model is continuous in value and gradient and depends on solar activity and magnetic activity.

One option that is already available for the IRI user is the extrapolation of the topside density and temperature formulas to plasmaspheric heights. This is of particular interest for comparisons with GNSS vTEC measurements.

There is also a number of newer plasmaspheric models that could be used in conjunction with IRI. The Neustrelitz plasmasphere model of Jakowski and Hoque (2018) consisting of an upper L-shell dependent part and a lower altitude dependent part matched at about 2000 km, both described by exponential decay functions. The underlying database are electron density data derived from dual-frequency Global Positioning System (GPS) measurements on-board the CHAMP satellite mission from 2000 to 2005. The model uses 40 coefficients to describe the variation of the plasmaspheric density with local time, solar zenith angle, day of year, magnetic latitude, L-value and solar activity. The Space Weather Integrated Forecasting Framework Plasmasphere Model of Pierrard and Voiculescu (2011) is a physics-based model that uses the equations for the equatorial density from Carpenter and Anderson (1992) and is coupled to IRI at the ionospheric boundary. Zhelavskaya et al. (2017) developed the Plasma density in the Inner magnetosphere Neural network-based Empirical model with IMAGE data and Neural Network algorithms. They tested various combinations of input parameters and found that the optimal model is based on the 96 hr time history of geomagnetic indices K_p, *AE*, *SYM-H*, and solar index *F*10.7. The model successfully reproduces erosion of the plasmasphere on the nightside and plume formation and evolution.

4. Ion Densities and Composition

In the ionospheric plasma the Debye length is very small ($\sim 10^{-3}$ m) and therefore charge neutrality can be assumed. Accordingly, IRI sets the total ion density equal to the electron density and gives the ion composition of the plasma in the form of percentages of the individual ions in relation to the total ion density (=electron density). In the F region the ion gas consists almost exclusively of O^+ ions. With decreasing altitude, first the heavier molecular ions O_2^+ and NO^+ become the dominant ion species and then below about 80–100 km the even heavier Cluster ions. In the topside and plasmasphere the light ions H^+ and He^+ are the dominant constituents. Because of the difference in the dominant ion species these regions are represented by different models in IRI with a merging altitude of 300 km.

Ion mass spectrometer and retarding potential analyzer (RPA) are the prime instruments for measuring ion densities in the ionosphere. In the lower ionosphere rocket measurements with these instruments are the main data source, while higher up satellites have provided us with a global view of ion densities. Often, however, these are evaluated in terms of absolute densities and getting the ion composition is not always possible. Altitude profiles of the ion composition in the lower topside can be obtained, to some extent, with ISRs, however, as noted earlier only a small number of these radars exist worldwide. The relatively small database, that is available for the development of ion composition models, limits their accuracy and reliability in particular in regions and time periods that are not adequately covered by the database.

The altitude profiles of the ion composition are characterized by two transition heights, already defined in Figure 1: the lower transition height (LTH) marks the point where the O^+ density decreasing from the F region downward becomes equal to the sum of the molecular ion densities and the upper transition height (UTH), where the O^+ density decreasing from the F region upward becomes equal to the sum of the light ion densities. Therefore these two heights indicate where the percentage of O^+ ions has dropped down to 50% and thus indicate the bottomside and topside extent of the O^+ ion layer and the transition to molecular ion or light ions, respectively. A review of existing LTH and UTH models and their use for IRI was presented by Bilitza (1991).

IRI describes monthly averages of the percentages of the most important ionospheric ions (O^+, H^+, He^+, N^+, NO^+, O_2^+, Cluster ions) from 60 to 2,000 km on the whole globe. The IRI user can choose between two model options, the older one developed by Danilov and Yaichnikov (1985) and improved below 300 km by Danilov and Smirnova (1995) (DY85/DS95 option), mainly based on Russian high-altitude rocket measurements, and the newer one developed by Třísková et al. (2003), Richards et al. (2010), and Truhlik et al. (2015) (RBV10/TBT15 option, the recommended default), based on in situ satellite measurements from Intercosmos-24, AE-C, and AE-E and in the lower ionosphere on the photochemistry from the Field Line Interhemispheric Plasma (FLIP) model developed by Richards (2001, 2002, 2004).

It should be noted that Cluster ions are only included with the DY85/DS95 option and not with the RBV10/TBT15 option. Users of the IRI ion composition have to keep in mind that currently a simple merging approach is used between the topside and bottomside models. This approach sets the light ions to zero below the merging altitude of 300 km and the molecular ions to zero above 300 km. A better method is to let these percentages decrease exponentially starting from their values at 300 km. This will be implemented in a future version of IRI.

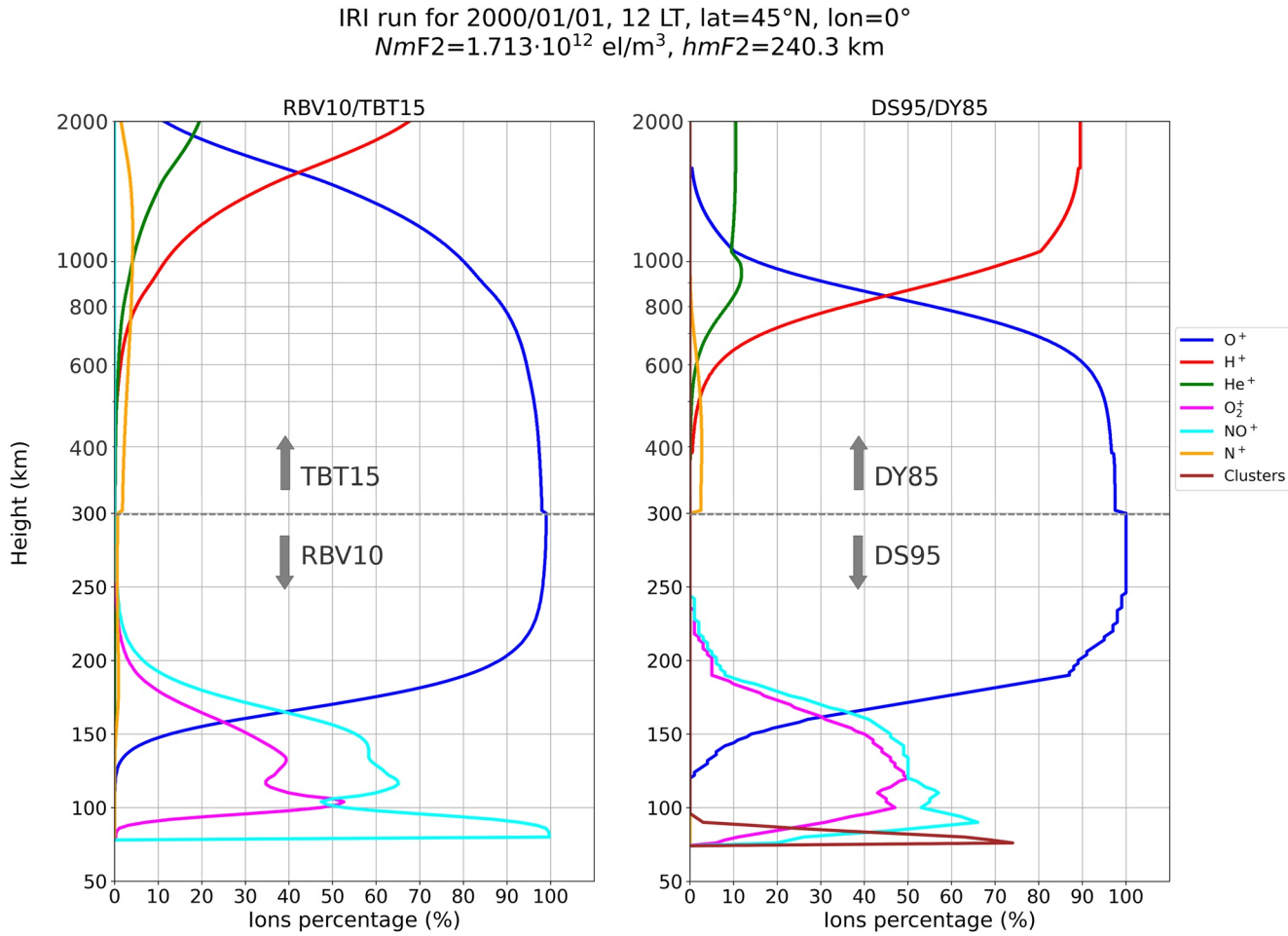

Figure 11. 1 January 2000 at 12 LT at Latitude 45°N and Longitude 0°. Ions percentage profiles calculated with (left) the RBV10/TBT15 option and (right) the DY85/DS95 option.

Figure 11 shows an example of the different vertical ions percentage profiles, according to both the RBV10/TBT15 option and the DY85/DS95 option.

4.1. The DY85 Model

The DY85 ion composition model was proposed by Danilov and Yaichnikov (1985) and is based on earlier work by Danilov and Semenov (1978). It was developed mainly considering ion mass spectrometer measurements from rocket flights and, for the region above 200 km, measurements from the AE-C, S3-1, AEROS-B, Sputnik-3 and Cosmos-274 satellites.

The model assumes that the vertical profiles of each ion species can be described by a universal equation

$$n_i = \begin{cases} n_{0i} \exp\left[\alpha_{1i} \cdot (h - h_{0i})^2 + \beta_{1i} \cdot (h - h_{0i})\right] & \text{for} \quad h > h_{0i} \\ n_{0i} \exp\left[\alpha_{2i} \cdot (h - h_{0i})^2 + \beta_{2i} \cdot (h - h_{0i})\right] & \text{for} \quad h < h_{0i} \end{cases}, \tag{33}$$

where n_i and n_{0i} are the relative concentration of the ith ion species at the altitude h and h_{0i} (the altitude of the maximum), respectively. α_{1i}, β_{1i}, and α_{2i}, β_{2i} are coefficients that describe the shape of the vertical profile below and above the maximum, respectively. So, the profile of each ion species depends on six parameters. The dependence of these parameters on the solar zenith angle χ, latitude φ, seasonal decimal month T, and solar activity $F10.7_{365}$ is considered through the following relation

$$x_i = A_1 + A_2 \cos \chi + A_3 \cos \varphi + A_4 \cos \left[\frac{2\pi(T-6)}{12}\right] + A_5 \cos \left[\frac{2\pi}{483}(300 - F10.7_{365})\right], \quad (33a)$$

where $x_i = (n_{0i}, h_{0i}, \alpha_{1i}, \beta_{1i}, \alpha_{2i}$, and $\beta_{2i})$. Therefore, to fully describe one ion species, 6·5 = 30 coefficients are needed and are obtained through least-square fitting to the data. Danilov and Yaichnikov (1985) used this method to determine model coefficients for the seven most important ionospheric ions: Cluster ions, NO^+, $O_2{}^+$, O^+, N^+, H^+, He^+. In a final step the ion percentages (ion composition) are then adjusted so that their total sum equals 100%:

$$n_i^* = \frac{n_i \cdot 100}{\sum_i n_i}. \quad (33b)$$

This final adjustment, however, can lead to somewhat unrealistic profiles as indicated by the He^+ profile above 1,000 km in Figure 11. This is one of the shortcomings of the DY85 model option.

Using additional rocket data and a more detailed analysis Danilov and Smirnova (1995) proposed a new improved model (DS95) for the region below 300 km and following their recommendation the lower part of DY85 was replaced by this new model that is described in the next section.

4.2. The DS95 Model for the Region Below the F Peak

Smirnova & Danilov (1994) noted shortcomings of the DY85 model in the lower ionosphere and developed a new model (DS95) for this region (Danilov & Smirnova, 1995) that is based on a more detailed analysis of the database used for DY85 plus a few additional rocket data. From this database they produced standard height profiles of NO^+ and $O_2{}^+$ percentages for the following conditions: three seasons (Northern/Southern hemisphere: summer/winter: May to August; winter/summer: November to March; equinox: April, September, October), two levels of solar activity ($F10.7_{365}$ = 70 and 140), and seven values of the solar zenith angle (20°, 40°, 60°, 70°, 80°, 85°, and 90°), that is, a total of 42 profiles. These profiles are described by a variable grid of 13 fixed points between 75 and 300 km. For intermediate heights linear interpolation is recommended and the same is used for intermediate solar zenith angles and intermediate levels of solar activity. A saturation effect is introduced for $F10.7_{365} > 140$. Above 100 km the difference from the percentages of the molecular ions to 100% is assigned to O^+ ions and below 100 km to Cluster ions.

4.3. The TBT15 Model for the Region Above the F Peak

An important step toward improved accuracy of the IRI topside ion composition model was made by Třísková et al. (2003) with the help of the global ion composition database provided by the Intercosmos-24 and AE-C and AE-E satellite missions. Their TTS03 model proved superior to the DY85 model in comparisons with ISIS-2, ISS-b, and AEROS-A data (Truhlik et al., 2003) and was adopted as the recommended IRI ion composition model. The C/NOFS satellite (de La Beaujardière & the C/NOFS Definition Team, 2004), that was launched in April 2008, offered a new and valuable data set for modeling the ionospheric ion composition in the low-latitude region. When comparing this data set with the IRI output, Heelis et al. (2009), Coley et al. (2010), and Klenzing et al. (2011) found that IRI overestimated the percentage of O^+ ions and underestimated the percentage of H^+ ions, especially during the anomalous and prolonged solar minimum years 2008–2009 (Bilitza et al., 2012; Y. Chen et al., 2011; Emmert et al., 2010; Perna & Pezzopane, 2016). Very low values of the UTH were another signature of the increased H^+ to O^+ density ratio observed during this period. UTH was much lower than the IRI model output, as was also reported from both the Arecibo ISR (Aponte et al., 2013) and the Kharkiv ISR (Kotov et al., 2015). With the help of data from the C/NOFS satellite Truhlik et al. (2015) were able to correct the behavior of the TTS03 model at low solar activities. Improvements were also achieved at high solar activity with a more effective exploitation of the Intercosmos-24, AE-C, and AE-D datasets. They also showed that with their new TBT15 model better agreement was achieved with the UTH observed by C/NOFS.

Like TTS03 the new TBT15 model uses the Booker (1977) approach (Appendix A) connecting the global variation at a set of fixed altitudes to construct the ion composition profiles. Besides being based on a larger data set than that used by TTS03, the TBT15 model uses four such anchor points instead of the three used by

TTS03. Moreover, instead of a linear dependence on the solar flux (specifically on the solar index $PF10.7$, see Section 9.1), it uses a logarithmic approach, and instead of modeling directly the percentages it first models the absolute densities and then normalizes to 100%. For the representation of global variations, the formalism used by TBT15 is similar to the one used by TTS03. For each individual ion during each season a system of associated Legendre polynomials up to the sixth order is applied

$$\log(n_i) = a_0^0 + \sum_{l=1}^{6} \left\{ a_l^0 P_l^0(\cos\theta) + \sum_{m=1}^{l} \left[a_l^m \cos(m\cdot\psi) + b_l^m \sin(m\cdot\psi) \right] P_l^m(\cos\theta) \right\}, \quad (34)$$

where n_i is the density of O^+, H^+, He^+, or N^+, P_l^m is the Legendre polynomial, ψ the magnetic local time (0,…,2π), and θ the *invdip* colatitude (0,…,π) (see Section 8) proposed by Truhlik et al. (2001); the coefficients a_l^m and b_l^m are determined through a standard least squares fitting procedure.

To obtain the ion density for a given day of the year and a given solar activity level, a linear interpolation between sub-models (in log of densities) is considered. Finally, the Booker (1977) formalism (Appendix A) is employed to generate vertical profiles.

4.4. The RBV10 Model for the Region Below the F Peak

In the E region chemical equilibrium can be assumed and the ion gain and loss processes are well represented in theoretical models and validated with satellite measurements from AE-C and AE-E. One of these models is the FLIP model that was developed by Richards (2001, 2002, 2004). Comparisons showed that the FLIP model provides a much better representation of AE-C ion densities in the lower ionosphere than the DS95 model (Richards et al., 2010) that is primarily based on a limited number of rocket measurements. The Richard-Bilitza-Voglozin (RBV10) model, also called ion density calculator, was developed with the goal of introducing the successful FLIP photochemistry formalism into the IRI model. RBV10 uses chemical equilibrium and the ion gain and loss processes from FLIP to determine the concentrations of O_2^+ and NO^+. For O^+ diffusion becomes important above ∼180 km and chemical equilibrium is no longer a valid assumption. The RBV10 model overcomes this problem by using an iterative technique to solve for the O^+ density given the IRI electron density and the fact that the total ion concentration must be equal to the electron density. The model uses the thermospheric O, O_2, and N_2 densities and neutral temperature provided by the United States Naval Research Laboratory Mass Spectrometer and Incoherent Scatter radar Extended (NRLMSISE-00) model (Picone et al., 2002). The photoionization rates are calculated using the solar irradiances from the EUV flux for Aeronomic Calculations model (Richards et al., 1994), while the secondary ion production rates are provided by the simple photoelectron flux model published by Richards and Torr (1983). The dependence on the solar activity is considered through the indices $F10.7_{81}$ and $F10.7_d$.

5. Plasma Temperatures

Three processes were found to be the dominant factors in determining the ionospheric plasma temperatures: (a) heating of the ambient electrons by the solar EUV produced photoelectrons; (b) energy loss through collisions; the electrons lose energy through Coulomb collisions with the ions, thereby heating the ion gas; electron and ions lose energy through collisions with neutrals; (c) heat conduction along magnetic field lines.

The lack of thermal equilibrium between electrons, ions, and neutrals in the ionosphere is by now well established, observed in situ by satellites and rockets and from the ground with incoherent scatter radars and reproduced by theoretical simulations. The electron temperature (T_e) exceeds the ion and neutral temperatures (T_i and T_n) because of its preferred heating by the solar EUV produced photoelectrons and the ion temperature exceeds the neutral temperature because of its preferred heating by the electrons through Coulomb collisions. This holds true through most of the ionosphere. With increasing altitude photoelectron heating becomes less important leading eventually to a common temperature for electrons and ions. At lower altitudes thermal equilibrium is reached between all three constituents because of the high neutral densities and accordingly very high collision frequencies. Accordingly, IRI assumes $T_e = T_i = T_n$ at $h_{TA} = 120$ km and below, and merges the ion temperature with the electron temperature at higher altitudes. Throughout the ionosphere IRI enforces the criteria $T_e \geq T_i \geq T_n$.

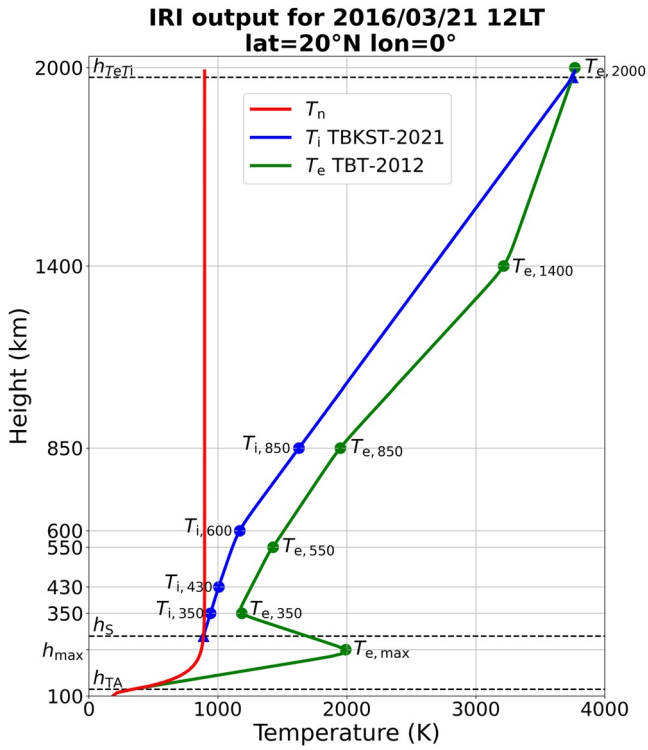

Figure 12. IRI-2016 modeled vertical profiles of neutral temperature (red), ion temperature (blue), and electron temperature (green) at a low-latitude location (latitude = 20°N, longitude = 0°) for 21 March 2016 at 12 LT. The anchor points used by IRI to model the different sections of the temperatures profiles, as well as the characteristic altitudes h_{TA} = 120 km, h_S and h_{TeTi}, are also highlighted.

IRI gives a monthly average description of the electron and ion temperatures in the ionosphere over the whole globe based on combining the global picture provided by satellite in situ measurements with the long-term record of altitudinal, diurnal and seasonal variations obtained by the incoherent scatter radars.

Figure 12 shows an IRI example of neutral, electron and ion temperature profiles in which the corresponding anchor points and significant altitudes are also highlighted (see the next sections for an explanation of these points).

5.1. The Neutral Temperature Reference

When COSPAR initiated the IRI project in the late sixties, COSPAR asked the IRI team to use the COSPAR International Reference Atmosphere (CIRA) as its reference for the neutral atmosphere and to take 120 km as the altitude from where on downward thermal equilibrium ($T_e = T_i = T_n$) can be assumed. Following COSPAR's advice, IRI used the CIRA neutral temperature values beginning with CIRA (1972). When the CIRA Working Group certified the empirical Mass Spectrometer Incoherent Scatter radar Extended to the ground (MSISE-90) model of Hedin (1991) as the new CIRA model, it was also implemented in IRI. A similar change then occurred with the 2012 version of IRI, which includes the NRLMSISE-00 empirical model that was developed by Picone et al. (2002), and had been accepted as the next version of CIRA. The NRLMSISE-00 model is a major upgrade of the MSISE-90 model using additional data from ground-based observations and from rocket and satellite experiments to describe the neutral densities and temperature from the ground to the top of the atmosphere. The Mass Spectrometer and Incoherent Scatter radar-class empirical models rely on parametric analytic approximations to the physical theory for the vertical structure of the atmosphere as a function of location, time, solar and geomagnetic activity; details are provided in the appendix of Hedin (1987).

5.2. The Electron Temperature

Concerning the electron temperature (T_e) IRI provides two options: BIL-1985 and TBT-2012, the latter also with a version taking into account the solar activity (SA) dependence (TBT-2012+SA).

The modeling philosophy characterizing the two options is the same applying a spherical harmonics representation of the global temperature variations at fixed heights and describing the altitudinal variation by connecting these global maps with the help of Epstein functions. Several satellite missions with circular orbits at different altitudes have provided the database for this approach involving measurements by LP and RPA instruments. Data from ISRs were an important source for studying the altitudinal, seasonal, and diurnal variation patterns of T_e and were also used extensively for model validation purposes. ISR data were the prime data source for modeling the region below 300 km altitude where a pronounced peak is observed at low latitudes. The almost horizontal magnetic field lines near the magnetic equator inhibit vertical heat conduction and thus produce the temperature peak.

5.2.1. The BIL-1985 Option

At the core of the BIL-1985 model (Bilitza, 1985c) are global maps of T_e at seven altitudes, namely h_i = 120 km, h_{max}, 300, 400, 600, 1,400, and 3,000 km for i = 0 to 6. At h_0 = 120 km thermal equilibrium with the neutrals can be assumed and the electron temperature is equal to the neutral temperature given by the NRLMSISE-00 model. The location and magnitude of the temperature peak is characterized by the height h_{max} and the temperature $T_{e,max}$. The variation of these parameters with geomagnetic latitude λ during daytime was established with the help of ISR data from Jicamarca, Arecibo and Millstone Hill

$$\frac{h_{\max}}{\text{km}} = 210 + 60\exp\left[-(\lambda/22.41)^2\right], \tag{35a}$$

$$\frac{T_{e,\max}}{\text{K}} = 1500 + 800\exp\left[-(\lambda/33)^2\right]. \tag{35b}$$

Both parameters peak at the magnetic equator and decrease toward a constant mid-latitude value. For nighttime the model assumes a constant value of 150 km for $h_{\max}$ based on the ISR data and the corresponding $T_{e,\max}$ value is obtained from NRLMSISE-00 at this altitude. For the diurnal variation the HPOL function with Epstein transitions at sunset and sunrise is applied (Equation A8 of Appendix A).

At 300, 400, 1,400, and 3,000 km IRI relies on the global spherical harmonics models developed by Brace and Theis (1981) based on their AE-C LP measurements for the two lower altitudes and on their ISIS-1 and -2 LP measurements for 3,000 and 1,400 km, respectively. The spherical harmonics models use eighth order polynomials of dip latitude and local time. Different sets of coefficients are given for equinox and for solstice conditions. For the intermediate height of 600 km the BIL-1985 model takes advantage of the global model that was developed by Spenner & Plugge (1979) based on their AEROS-A RPA data. The spherical harmonics model describes T_e in terms of latitude, longitude, and height at the two local times (03:00 LT and 15:00 LT) that are covered by sun-synchronous orbit of AEROS-A. With the help of this model Bilitza (1985c) approximated the daytime and nighttime electron temperature at 600 km as a function of geomagnetic latitude λ

$$T_e(600\,\text{km, daytime}) = 2900 - 5600\frac{\exp(-\lambda/11.35)}{[1+\exp(-\lambda/11.35)]^2}, \tag{36a}$$

$$T_e(600\,\text{km, nighttime}) = 839 - \frac{1161}{1+\exp\left[-\frac{(|\lambda|-45)}{5}\right]}. \tag{36b}$$

A continuous diurnal variation is then again obtained with the HPOL function. One shortcoming of this model option is the fact that data behind the different global maps cover different ranges of solar activity. The AE-C and AEROS based maps at 300 km, 400 and 600 km represent low solar activity, while ISIS-1 and ISIS-2 data covered respectively high and moderate solar activity.

5.2.2. The TBT-2012 Option and TBT-2012+SA Option

Following the approach of Bilitza (1985c) and Bilitza et al. (1985), Truhlik et al. (2000) utilized data from Intercosmos 19, 24, and 25 satellites to develop global models at 350, 550, 850, 1,400, and 2,000 km of altitude (shown in Figure 12) characterized by a more refined description of the diurnal variation including the early morning overshoot (Da Rosa, 1966; Oyama et al., 1996; Stolle et al., 2011; Yang et al., 2020) that was not well represented in previous models. Both the BIL-1995 and the TBT-2012 models describe the variations in terms of magnetic latitude and magnetic local time, providing definite sets of coefficients for different seasons. They have performed quite well when compared with satellite and ISR measurements. Their main shortcoming is the fact that they do not consider variations with solar activity. Including this dependence is a really difficult task because T_e is determined by the balance of three factors: (a) heating due to the solar EUV irradiance; (b) cooling through collisions with neutrals and ions; (c) heat conduction along magnetic field lines. Each of these three terms increases with solar activity and since they compensate each other, the net result could be a T_e increase, decrease, or no change at all.

Bilitza et al. (2007) and Truhlik et al. (2009) have investigated the complex dependence of T_e on solar activity with a large database of satellite in situ measurements and with the help of two models: the FLIP physical model (Richards, 2001) and the empirical model of S.-R. Zhang et al. (2005) based on many years of Millstone Hill ISR measurements. Their work resulted in a new version of the TBT-2012 option (TBT-2012+SA) that now includes the dependence on solar activity (Truhlik et al., 2012), through a correction term, depending on the solar index *PF*10.7 (see Section 9.1). Comparisons with data by Truhlik et al. (2012) have shown that this new version is more reliable than the older versions and consequently the TBT-2012+SA is now the default option in the IRI model.

Recently, Pignalberi, Giannattasio, et al. (2021) have compared the output of the TBT-2012+SA model with measurements made by Swarm satellites and ISRs and found that the spatial and temporal large-scale patterns are well reproduced by the IRI model. The largest differences emerged at magnetic equator latitudes at dawn, and at low and mid latitudes during daytime and nighttime, respectively.

5.3. The Ion Temperature

At topside altitudes slight differences are found between the temperatures of the different ion species (O^+, H^+, He^+) but in general they are negligibly small (Banks, 1967) and only one common ion temperature is provided in IRI. Two options are provided in IRI for the ion temperature, the Bil-1981 model (Bilitza, 1981b) and the TBKST-2021 model (Truhlik et al., 2021). The TBKST-2021 option is the recommended default because it is based on a larger database and includes seasonal and solar activity dependencies that were not included with the Bil-1981 model due to its more limited database.

5.3.1. The Bil-1981 Ion Temperature Model

The IRI description of the ionosphere vertical ion temperature (T_i) profile dates back in the 80's and is based on the work of Bilitza (1981b). As suggested by theoretical simulation and shown by observational evidence, the IRI ion temperature model is in thermal equilibrium with the neutral temperature (T_n) at low altitudes, and with T_e at high altitudes (see Figure 12).

For modeling the intermediate altitude range in which T_i departs from T_n and T_e Bilitza (1981b) introduces an anchor point at 430 km and the description of the gradients below and above 430 km. For this task, he exploited data collected in the 60's and 70's by ISRs (Jicamarca, Arecibo, and Millstone Hill) and RPA data from the AEROS-A and -B satellites. For the ion temperature at 430 km the data showed a strong dependence on geomagnetic latitude λ

$$T_i(430, \lambda) = \begin{cases} 1240 - 1400\dfrac{\exp(-0.09\lambda)}{[1 + \exp(-0.09\lambda)]^2} & \text{daytime,} \\ 1200 - 300\dfrac{\cos(Z)}{|\cos(Z)|}\sqrt{|\cos(Z)|} & \text{nighttime,} \end{cases} \quad (37)$$

where $Z = 0.47|\lambda| + 0.024\lambda^2$.

Here again the HPOL function from Appendix A is used to obtain a smooth transition from the constant daytime value to the constant nighttime value. The gradient ST_1 below 430 km is obtained by connecting the T_i profile to the T_n profile at the height h_S. Bilitza (1981b) obtained h_S as the height where the tangent from the T_n profile passes through T_i(430 km). However, this process did not always produce satisfying results and with the IRI-2016 version a constant value of 200 km was introduced for h_S. The gradient ST_2 above 430 km is approximated by an average value of 3 K/km for daytime and 0 K/km for nighttime. HPOL is then applied to get a continuous diurnal variation. Next the height h_{TeTi} is determined where the T_i profile defined by T_i(430 km) and ST_2 crosses the T_e profile. Bilitza (1981b) then applied Booker's (1977) mathematical approach (Appendix A) to combine the segments of constant gradient (ST_1, ST_2, ST_3) into a smooth, analytical representation of the ion temperature vertical profile. Here ST_3 is the corresponding gradient used for the T_e profile above h_{TeTi}.

According to the aforementioned equations, Bil-1981 does not explicitly describe the seasonal and solar activity variability of the ion temperature. These variations are included implicitly below h_S because $T_i = T_n$ and above h_{TeTi} because $T_i = T_e$, and because both T_n from the NRLMSISE-00 model (Picone et al., 2002) and T_e from the default IRI option (Truhlik et al., 2012) are characterized by seasonal and solar activity variations. However, several authors have highlighted the need for an improved description of the solar activity dependence in the IRI ion temperature modeling (Bilitza & Hoegy, 1990; Buonsanto, 1989).

5.3.2. The TBKST-2021 Ion Temperature Model

Truhlik et al. (2021) proposed a new global model of T_i, which resolves some shortcomings of the current option (as pointed out by, e.g., Pignalberi, Aksonova, et al., 2021; Rana et al., 2019). The model is based on a database comprising of almost all available T_i satellite data obtained by means of RPA measurements. Bilitza et al. (2007) pointed out that combining data from different satellites it is extremely important to assess the data quality of the individual datasets and discard or correct datasets with known contamination problems. Thus, the used data

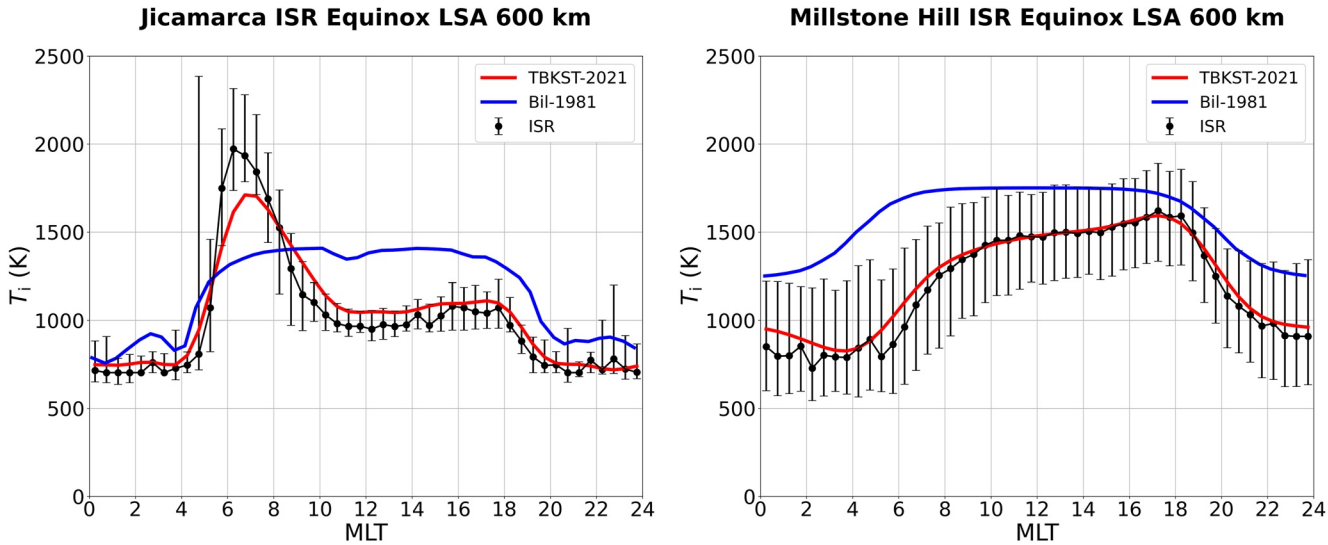

Figure 13. Comparison between the TBKST-2021 model proposed by Truhlik et al. (2021) (in red), the current IRI model (Bil-1981, in blue) and ISR data (in black) from Jicamarca (left) and Millstone Hill (right), at an altitude of 600 km, for an equinox period and for low solar activity. Concerning the ISR data, the black circles are half-hour medians, while the error bars are the upper and lower quartiles. Note the T_i morning enhancement (between 6 and 7 magnetic local time) at Jicamarca, that is not included in the Bil-1981 option, but well represented by the TBKST-2021 model.

were corrected and inter-calibrated through comparisons with T_i data from long term measurements made by three ISRs: Jicamarca, Arecibo, and Millstone Hill. The altitude range described by the model ranges from 350 to 850 km covering the region where generally T_i is higher than T_n and lower than T_e. For altitudes above 850 km and below 350 km an extrapolation is used in such a way that at high altitudes T_i merges with T_e and at low altitudes T_i merges with T_n. Instead of a single anchor point at an altitude of 430 km, the new model includes global models at four anchor points (350, 430, 600, and 850 km). Both models use a common merging point, $h_S = 210$ km, as an additional anchor point. Figure 12 shows an example of a T_i profile generated by the TBKST-2021 model.

The comparison of the new model with the Bil-1981 T_i model and with ISR data in Figure 13 illustrates the significant improvement achieved with the new model. Most importantly, it describes the well-established early morning peak at low latitudes and the late afternoon peak at mid latitudes.

6. IRI at Low Latitudes

At low latitudes the almost horizontal magnetic field and the eastward current (electrojet) flowing along the magnetic equator (Lühr et al., 2021) produce a number of irregularities (Abdu, 2020) and anomalies that make modeling this region particularly difficult (Fejer & Maute, 2021). The interaction of the magnetic field **B** and the electric field **E** generates an **E** × **B** drift that pushes the ionospheric plasma upward at the magnetic equator (appropriately called Fountain Effect), which then moves down the magnetic field lines forming maxima on both sides of the equator at about 15°–20° dip latitude. In addition to the plasma densities and temperatures IRI provides an estimate of the equatorial vertical plasma drift because it is the main driver of the EIA. Plasma instabilities caused by rapid changes in the vertical plasma transport (Rayleigh-Taylor instability) result in bubbles of lower density that can have detrimental effects on applications that depend on radio waves traveling through the ionosphere. To assist such application IRI output includes the occurrence probability of spread-F, which is the signature of plasma bubbles recorded by ionosondes from the ground. The bubbles also cause rapid fluctuations in amplitude and phase of traversing radio signals, called scintillations, that can disrupt satellite-based communication links. A review of existing ionospheric scintillation models was presented by Priyadarshi (2015) and a first attempt at an IRI scintillation occurrence model was presented by S.-P. Chen et al. (2017). Shi et al. (2011) and Alfonsi et al. (2013) showed that there is a strong correlation between the occurrence of spread-F and scintillations. The challenges of plasma bubble and scintillation forecast were recently discussed by Li et al. (2021).

6.1. The Equatorial Vertical Ion Drift Model

The first global empirical model of the equatorial F-region vertical ion drift v_i was developed by Scherliess and Fejer (1999) by combining the AE-E data set of Fejer et al. (1995) with the vertical drift observations made from 1968 to 1992 by the ISR in Jicamarca. Up to now IRI has relied on this first model to describe v_i. In the latest version v_i is represented by the newer model of Fejer et al. (2008) that is based on 5 years of Republic of China satellite-1 (ROCSAT-1) measurements. This model describes the variation of v_i with local time, season and longitude at an altitude of 600 km under moderate and high solar activity conditions. The longitudinal dependence of v_i is much stronger than in the earlier model exhibiting the characteristic wave-number-four signature and the seasonal/longitudinal variation of the pre-reversal evening peak, features which are well observed in the data. This improvement was possible because the ROCSAT-1 data provide a much higher longitudinal resolution than the AE-E data with which the Scherliess and Fejer (1999) model was built. Data-model discrepancies were reported particularly in the African sector (Dubazane & Habarulema, 2018; Marew et al., 2019).

The Fejer et al. (2008) model consists of data tables for each half-hour, each 15 longitude bin, each season and daily value of the solar index $F10.7_d$ from 100 to 200 in steps of 10. Interpolation and extrapolation is performed for conditions not covered by these grid points. The model results are in excellent agreement with measurements from other space and ground-based measurements including data from the Jicamarca ISR.

6.2. The Spread-F Occurrence Probability Model

Plasma irregularities and inhomogeneities are responsible for the spread both in range and in frequency that is observed on ionograms recorded especially at equatorial and low latitudes, a phenomenon that was first reported by Booker and Wells (1938). Equatorial spread-F phenomena usually occur just after local sunset (e.g., Pezzopane, Zuccheretti, et al., 2013; Pietrella et al., 2017) and the scale sizes of the irregularities responsible for the phenomenon range from a few centimeters to a few hundred kilometers (Abdu et al., 2003). After sunset, at the magnetic equator, the F layer may rapidly rise and develop a steep bottomside gradient that results in an F-region plasma density profile shaped by the Rayleigh-Taylor (RT) instability (Ossakow, 1981). Other authors suggested that the basic mechanism at the base of the equatorial spread-F onset is the RT instability in conjunction with the $\mathbf{E} \times \mathbf{B}$ drift pre-dusk reversal, where $\mathbf{E}$ is the ionospheric zonal electric field and $\mathbf{B}$ the geomagnetic field (Abdu, 2001).

The parameter most interesting for applications that utilize radio waves propagating through the ionosphere is the spread-F occurrence probability. IRI provides this information based on the model of Abdu et al. (2003). To set up the model Abdu et al. (2003) considered 13 years (from 1978 to 1990) of spread-F data recorded by the Brazilian ionosonde stations at Fortaleza (3.9°S, 321.5°E) near the magnetic equator, and at Cachoeira Paulista (22.6°S, 315.0°E). They grouped the data set according to low, medium, and high solar activity levels, represented, respectively, by: $F10.7_d \leq 100$, $100 < F10.7_d < 180$, and $F10.7_d \geq 180$. They scaled ionograms separately for the range spread-F (RSF) and frequency spread-F (FSF), and included in the data set only the RSF events. RSF ionograms present an echo spreading mainly along the range axis and they are associated with plasma irregularities in the lower part of the F region, while FSF ionograms present echo spreading along the frequency axis close to the critical frequencies of the ordinary and extraordinary traces, so they are associated with irregularities nearby the F-region peak (e.g., Cabrera et al., 2010).

The monthly percentage (P) of spread-F occurrence, as a function of local time t, geographic latitude φ, month m and solar activity $F10.7_d$, is expressed as a product of univariate normalized cubic-B splines:

$$P(t, m, F10.7_d, \varphi) = \sum_{i=1}^{23} \sum_{j=1}^{12} \sum_{k=1}^{3} \sum_{l=1}^{2} a_{i,j,k,l} N_{i,4}(t) N_{j,2}(m) N_{k,2}(F10.7_d) N_{l,2}(\varphi), \quad (38)$$

where $N_{i,4}(t)$ is a cubic-B spline of order four to consider the LT dependence, $N_{j,2}(m)$, $N_{k,2}(F10.7_d)$, $N_{l,2}(\varphi)$ are cubic-B splines of order two to consider the seasonal, solar activity and latitudinal dependences; $a_{i,j,k,l}$ are the monthly means of the spread-F occurrences for each interval of LT, month, solar flux, and latitude. The IRI implementation of the model added the constraint $0 \leq P \leq 1$ to avoid unrealistic probabilities.

Since the spread-F phenomenon occurs mainly during evening to morning hours, Abdu et al. (2003) chose 23 local time nodes distributed at one hour interval between 16 and 08 LT, except between 18–21 and 03–06 LT

where the time nodes are distributed at half an hour interval to account for the rapid changes characterizing the spread-F occurrence.

The main limitation of this model is that it is regional, based on Brazilian data, while significant differences have been found regarding the spread-F occurrence in different longitude sectors of the globe (Abdu et al., 1981; Batista et al., 1986; Pezzopane, Zuccheretti, et al., 2013; Pietrella et al., 2017). Klinngam et al. (2015) and Thammavongsy et al. (2020) have shown that the IRI spread-F probability tends to overestimate the actual occurrence in the Southeast Asia sector.

To get a global empirical description of the equatorial spread-F occurrence it is necessary to combine the spread-F occurrence statistics from different longitude sectors. Future improvements may also benefit from the relationship between the occurrence rate of spread-F and the equatorial vertical plasma drift (Stolle et al., 2008).

7. IRI at High Latitudes

At high latitudes the multitude of interactions of the ionospheric plasma with the magnetosphere, radiation belts, and solar wind makes the empirical representation of this region a very complex task. The high-latitude ionosphere can be separated into two characteristic regions with significantly different variation patterns and dependences: the auroral oval and the polar cap within this oval. The northern and southern auroral ovals are around the magnetic poles at about 60°–80°N/S magnetic latitude and visible from space and from below by the beautiful display of the Northern/Southern Lights (Aurora borealis/australis). The connection between the Earth internal magnetic field, the magnetospheric magnetic field, and the interplanetary magnetic field (IMF) is such that energetic electrons can precipitate deep into the atmosphere generating the auroral display. In the polar cap, density enhancements are observed and described as polar patches and auroral arcs. Themens et al. (2017) have focused on developing an empirical model for the F2-peak density and height in this region in the framework of their E-CHAIM effort, and they recently extended this modeling activity to the topside (Themens et al., 2018) and bottomside (Themens et al., 2019). They have found a strong model performance in representing vTEC measurements from the high-latitude region (Themens et al., 2021).

7.1. Auroral Boundaries

A demarcation of auroral boundaries has been an important goal of the IRI team from early on as a starting point for a more accurate representation of the high-latitude ionosphere in IRI. Auroral oval boundaries are important because they mark the region of highest electron precipitation, the boundary from closed to open magnetic field lines, and the IMF/solar wind-induced ion convection. During magnetically disturbed periods the oval expands equatorward. Szuszczewicz et al. (1993) and Bilitza (1995) discussed and compared the different existing models for representing auroral boundaries. Feldstein and Starkov (1967) proposed a set of representative ovals for seven different levels of the geomagnetic activity based on all-sky imager observations from the International Geophysical Year time period 1957–1958. Holzworth and Meng (1975) used a third-order Fourier formula to set up a simple mathematical representation of these boundaries. Other statistical models, exploiting in situ flux measurements from different satellites, were developed for the auroral precipitating electron flux and the resulting Hall and Pedersen conductivities (Fuller-Rowell & Evans, 1987; Hardy et al., 1987; Spiro et al., 1982; Wallis & Budzinski, 1981); auroral boundaries are easily obtained from these models by choosing a minimum flux or conductivity level.

Y. Zhang and Paxton (2008) presented a new approach based on ultraviolet observations by the Global Ultraviolet Imager (GUVI) of the Thermosphere Ionosphere Mesosphere Energetics and Dynamics (TIMED) satellite. The great advantage of the imager is that it generates a much larger database and a better global and LT coverage than the in situ measurements on which the previous models were based. Y. Zhang and Paxton (2008) used the Atmospheric Ultraviolet Radiance Integrated Code (AURIC) of Strickland et al. (1999) and the Boltzmann Three Constituent auroral transport code of Daniell (1993) to obtain tables that allowed relating the radiances to the flux characteristics of precipitating electrons, including the mean energy E_0 and the energy flux Q. They considered GUVI data from 2002 to 2005 (~44,000 images) to develop E_0 and Q models describing variations with magnetic latitude and magnetic local time for different levels of geomagnetic activity. Their database included some intense super-storms and so they were able to consider a wider range of magnetic activity conditions (K_p = 0–9) than the earlier models.

The IRI model uses a threshold flux of 0.25 erg cm^{-2} s^{-1} for obtaining the equatorward auroral boundary from the Y. Zhang and Paxton (2008) model.

Y. Zhang et al. (2010) proposed a real-time updating of the Y. Zhang and Paxton (2008) model for IRI with the help of an effective K_p value. This value is determined by adjusting the model to the actual auroral boundary value identified during auroral crossings of TIMED/GUVI or the Special Sensor Ultraviolet Spectrographic Imager (SSUSI) on-board DMSP satellites (Paxton et al., 2002).

7.2. The Storm Model for the Auroral E Region

During geomagnetic storms particle precipitations can significantly increase the electron density in the auroral E region, with a consequent interruption of HF communications. McKinnell et al. (2004) and McKinnell and Friedrich (2007) were the first who tried to model this feature for IRI, proposing their Ionospheric Model for Auroral Zone (IMAZ), based on European Incoherent Scatter Scientific Association (EISCAT) ISR measurements from 1984 to 1998 and about 50 rocket flights. The IMAZ model is using a neural network that was trained with the EISCAT data set. However, it was difficult to integrate it into the IRI model because one of the required inputs was the riometer absorption value from a nearby riometer. As a compromise, IMAZ was provided as an independent code.

A new model for the auroral E-region storm effects was introduced with the 2012 version of IRI. The model was developed by Mertens et al. (2013a, 2013b), based on data from the TIMED Sounding of the Atmosphere using the Broadband Emission Radiometry (SABER) instrument. Mertens et al. (2013a, 2013b) identified the 4.3 μm radiance measurement as a good proxy for characterizing the response of the nighttime E-region electron density to auroral precipitation. In fact, while it is true that the emissions at this wavelength during daytime are dominated by the CO_2 vibrational rotation bands, during nighttime the emissions from vibrationally excited NO^+ become important and can be reliably separated from the background CO_2 contribution. The strong point of Mertens et al. (2013a, 2013b) approach is that they showed that NO^+ Volume Emission Rate (*VER*) is an excellent proxy for the incoming energy flux. According to this, Mertens et al. (2013b) proposed that the storm-time to quiet-time ratio (r) for the auroral E-region electron density can be obtained from corresponding *VERs* as

$$r = \frac{VER_{\text{storm}}}{VER_{\text{quiet}}} \approx \frac{\left[\text{NO}^+\right]_{\text{storm}}}{\left[\text{NO}^+\right]_{\text{quiet}}} \approx \frac{[N_e]_{\text{storm}}}{[N_e]_{\text{quiet}}}, \tag{39}$$

where N_e is the electron density; in addition, a power-law function is used to describe the dependence of r on the 3-hourly a_p index as

$$r\left(a_p, \lambda\right) = k_1 \cdot a_p^{k_2} + k_3, \tag{40}$$

where k_1, k_2, and k_3 are coefficients depending on the magnetic latitude λ. Tests made by Mertens et al. (2013b) considering ISR measurements showed a good consistency of this approach. However, an important limitation of this method is the restriction to nighttime and twilight hours. To overcome this fact, the nighttime $r(a_p, \lambda)$ dependence is assumed to be valid throughout the day.

8. Coordinates Used in IRI

IRI uses a number of different coordinates and coordinate systems that have proven to be appropriate for specific global areas or altitudinal regimes. At lower altitudes with a strong control by the neutrals mostly geographic latitude and longitude are used. With increasing altitude and decreasing neutral densities the influence of the Earth's magnetic field on the ionosphere becomes more important and magnetic coordinates are used. Magnetic field modeling has progressed over the years and a number of different magnetic coordinate systems have been introduced and are being used in IRI. Similar to IRI and CIRA there is also an international standard for the Earth's magnetic field, called International Geomagnetic Reference Field (IGRF) (Alken et al., 2021). IGRF consists of spherical harmonics models in a 5-year progression and the coefficients for projecting for 5 years into the future. An international Working Group of International Association of Geomagnetism and Aeronomy (IAGA) is in

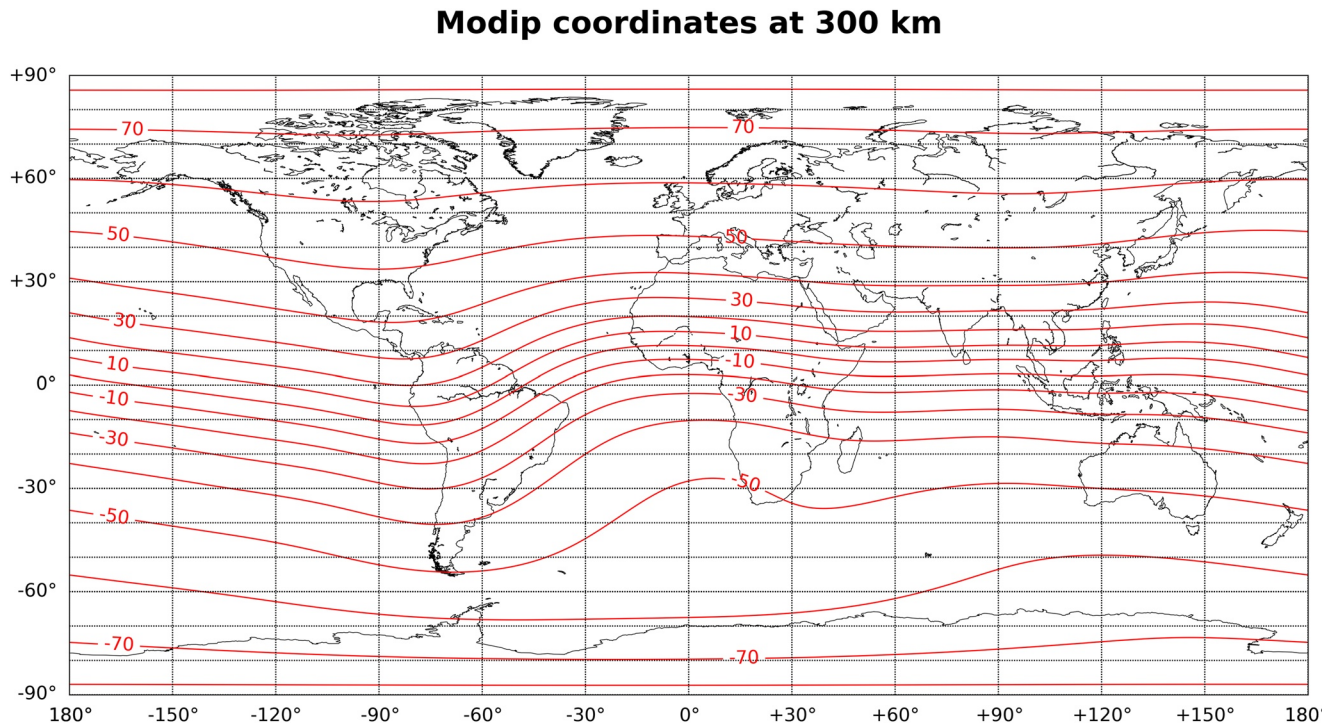

Figure 14. Worldmap of the modified dip latitude (modip) at 300 km of altitude.

charge of model updates and release of a new addition 5 years after the last one. The IGRF geomagnetic latitude and longitude are used in IRI and are updated as new versions of IGRF are being released.

An important coordinate deduced from the IGRF model is the magnetic inclination (ψ), also called dip, which is the angle between the horizontal plane and the direction of the magnetic field line. An often-used coordinate related to the magnetic inclination is the magnetic dip latitude Ψ, which is defined by ψ at 300 km altitude as

$$\tan \Psi = \frac{1}{2} \tan \psi. \tag{41}$$

The modified dip latitude (modip) μ was introduced by Rawer (1963) to better represent the ionospheric variations particularly in equatorial and polar regions. It is defined as

$$\tan \mu = \frac{\psi}{\sqrt{\cos \varphi}}, \tag{42}$$

or to avoid the singularity at the poles ($\varphi = \pm 90°$) it is better to use the equivalent form

$$\sin \mu = \frac{\psi}{\sqrt{\psi^2 + \cos \varphi}}. \tag{43}$$

μ is close to magnetic inclination ψ at low latitudes and gets closer to the geographic latitude φ at higher latitudes. Figure 14 shows a worldmap of modip at 300 km of altitude.

The invariant dip latitude (*invdip*), introduced by Truhlik et al. (2001), gets closer to the dip latitude Ψ (see Equation 41) near the equator and closer to the invariant latitude (*invl*) at high latitudes, and it is defined as

$$invdip = \frac{\alpha \cdot invl + \beta \cdot \Psi}{\alpha + \beta}, \tag{44}$$

where

$$\alpha = \sin^3 |\Psi| \quad \text{and} \quad \beta = \cos^3 (invl), \tag{44a}$$

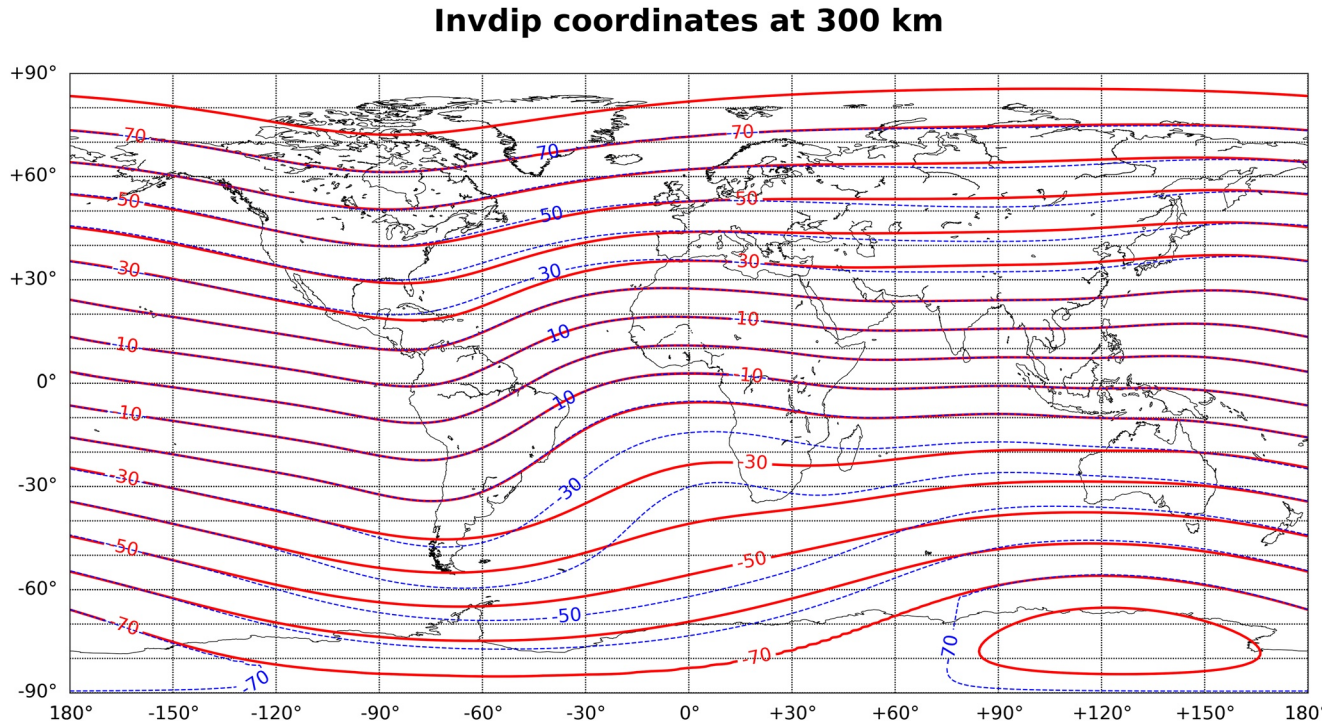

Figure 15. Worldmap of the invariant dip latitude (*invdip*) at 300 km of altitude using formula (Equation 44) (dashed blue lines) and formula (Equations 47a and 47b) (solid red lines).

and *invl* is defined as

$$L\cos^2(invl) = R. \tag{45}$$

The invariant radius R and the McIlwain parameter L are related through the equation

$$B = \frac{M}{R^3}\left(4 - \frac{3R}{L}\right)^{\frac{1}{2}}, \tag{45a}$$

where M is the dipole moment and B the magnetic flux density.

The IRI model calculates *invl* through the following expression

$$invl = A\cos\left(A\sum_{i=0}^{7} B_i A^i\right)^{\frac{1}{2}}, \tag{46}$$

where

$$A = \left(\frac{M}{B}\right)^{\frac{1}{3}} L^{-1}, \tag{46a}$$

and coefficients B_i are $B_0 = 1.25992100$, $B_1 = -0.19842590$, $B_2 = -0.04686632$, $B_3 = -0.01314096$, $B_4 = -0.00308824$, $B_5 = 0.00082777$, $B_6 = -0.00105877$ and $B_7 = 0.000183142$.

Figure 15 shows a worldmap of *invdip* at 300 km of altitude. IRI applies this coordinate primarily to model plasma temperatures.

Truhlik et al. (2015) introduced a slightly modified version of *invdip* to better follow the longitudinal variations in particular of ion composition. The new *invdip* coordinate uses the same formalism as (Equation 44) but with

$$\alpha = 2 - \frac{1}{\left[1 + \exp\left(\frac{\psi - 25}{2}\right)\right]} + \frac{1}{\left[1 + \exp\left(\frac{-\psi - 25}{2}\right)\right]}, \tag{47a}$$

$$\beta = -1 + \frac{1}{\left[1 + \exp\left(\frac{invl - 25}{2}\right)\right]} + \frac{1}{\left[1 + \exp\left(\frac{-invl - 25}{2}\right)\right]}. \tag{47b}$$

As Figure 15 shows at the equator and high latitudes the two coordinates are identical, at mid latitudes there are slight differences, especially in the Southern hemisphere.

9. IRI Drivers

In general, the external drivers of a model are extremely important because they help it to properly represent the ionospheric conditions. For IRI these are solar, magnetic, and ionospheric indices, obtained from solar, magnetic, and ionospheric measurements. They will be described in greater detail in the next sections. In addition, an IRI user can also input measured values for key ionospheric parameters as explained in Section 9.4.

9.1. Solar Indices

The daily sunspot number R, related to the daily number of spots and spots groups observed on the sun, was the main index for many of the early ionospheric models, and among them the IRI. Now, instead of R, models depend most frequently on R_{12}, the 12-month running mean of monthly values of R. R is distributed by the Solar Influences Data analysis Center (SIDC, http://sidc.oma.be/) in Brussels, Belgium. A recent review of the way R is computed from the observation of spots and groups of spots on the Sun resulted in a recalibration of the index (Clette et al., 2014). Recalibrated values of R are now internationally accepted and the new sunspot number is distributed by SIDC. The new index exceeds the old one by a factor of about 1.4. Models like IRI that were developed with the old R index need to account for this and in the case of IRI this is done by using the new index with a scaling factor of 0.7 (Gulyaeva, 2016). R_{12} is the solar index recommended by ITU to describe the solar activity of its widely used CCIR (1967) model for *fo*F2 and *M*(3000)F2. In IRI the R_{12} index is used for *hm*F2 (specifically, by both the BSE-1979 and the AMTB2013 options), for *fo*F1, for the bottomside thickness parameter B_0, for the electron density at the D-region inflection point and also by the NeQuick topside option.

$F10.7$ is the solar radio flux at 10.7 cm wavelength that has been measured since 1947, first at Ottawa, Ontario and then at the Penticton Radio Observatory in British Columbia, both in Canada (Tapping, 2013). The $F10.7$ index is also called Covington index in honor of Arthur Covington who first started the continuous monitoring of the solar radio flux in Ottawa. $F10.7$ is measured in solar flux units (sfu), where 1 sfu = 10^{-22} W · m^{-2} · Hz^{-1}. $F10.7$ is slowly replacing R in ionospheric modeling, because it correlates better with the EUV irradiance from the Sun that is responsible for the ionization of the ionosphere. Besides the daily index $F10.7_d$, IRI uses the 81-day (3 solar rotations) and the 365-day running mean of $F10.7$, respectively identified as $F10.7_{81}$ and $F10.7_{365}$. A combination of daily and 81-day indices, $PF10.7 = (F10.7_d + F10.7_{81})/2$, has also been used with good success for modeling the solar cycle dependence of ionospheric parameters in particular for the topside electron temperature and ion composition. The TBT15 ion composition model of Truhlik et al. (2015) uses this newer index, while the older option DS95/DY85 developed by Danilov and Yaichnikov (1985) and Danilov and Smirnova (1995) is modeled with the $F10.7_{365}$ index. $F10.7_d$ is used by the spread-F probability function of Abdu et al. (2003), and also to model the solar cycle dependence of the equatorial ion vertical drift (Fejer et al., 2008) and the D-region electron density (Friedrich et al., 2018). The $F10.7_{81}$ index is the parameter of choice of the SDMF2 option (Shubin, 2015; Shubin et al., 2013) to model the solar dependence of *hm*F2, while the $F10.7_{365}$ index is used by the IRI-2001 topside options. In addition to the $F10.7$ indices mentioned already, the $F10.7$ index from the day before is required as input for the NRLMSISE-00 model (Picone et al., 2002) that is used in IRI for defining the lower limits for the plasma temperatures and as input for the RBV10 ion composition model of Richards et al. (2010).

The IRI indices file "ig_rz.dat" includes the values of R_{12} and "apf107.dat" the $F10.7$ indices. Both files are starting from January 1958 and are updated twice a year; there is also an on-the-fly production option for these

files available on the IRI homepage (irimodel.org) that updates daily and was developed by D. Themens. IRI also offers an option for users to enter their own indices.

9.2. Ionospheric Indices

The Ionosonde Global (*IG*) index is obtained by adjusting the solar cycle representation of *fo*F2 used by the CCIR (1967) model to noontime *fo*F2 ionosonde measurements. The *IG* index was proposed by R. Liu et al. (1983) and is produced and distributed by the United Kingdom (UK) Solar System Data Centre (https://www.ukssdc.ac.uk/). Since CCIR provides *fo*F2 monthly averages, accordingly *IG* is a monthly index. *IG* local indices are calculated at definite ionosonde stations and then *IG* is obtained as the corresponding global median. The index was originally based on 11 reference stations; currently the index is determined with four reference stations: two from the Southern Hemisphere (Port Stanley/UK and Canberra/Canada) and two from the Northern Hemisphere (Kokubunji/Japan and Chilton/UK). This has limited the reliability of this index in representing the global ionospheric conditions; nevertheless, to describe the solar cycle changes in the F-region ionosphere *IG* is still better than R_{12} and $F10.7$ indices. The advantage of the *IG* index is that, being obtained from ionospheric measurements, it includes dynamic effects not covered by solar indices. Because the global index smooths out regional differences, it was found that *fo*F2 correlates better with the 12-month running mean IG_{12} of *IG* than with the monthly value. IG_{12} is then used in IRI when modeling *fo*F2. Brown et al. (2018) found that, considering hemispheric *IG* indices, monthly indices perform better than the 12-month running means. Specifically, they showed that using monthly hemispheric indices improves the IRI model performance by almost a factor of 2. This is explainable through the significant hemispheric differences characterizing the station-specific *IG* values that are smoothed out once a global index is computed. Also Themens & Jayachandran (2016) strengthened this point in their study of IRI performance in the polar cap and sub-auroral region. The IRI files "ig_rz.dat" includes values of the IG_{12} index from January 1958 onward.

9.3. Geomagnetic Indices

A geomagnetic index is usually a good proxy for the representation of the average geomagnetic and ionospheric conditions in terms of broad categories such as "quiet," "moderate" or "disturbed."

The geomagnetic indices officially adopted by IAGA can be divided in three major "families" (Kauristie et al., 2017):

1. The K_p–index of global activity (K_p, a_p, A_p, a_a);
2. Indices describing the magnetospheric ring current (D_{st} and its variants);
3. The *AE*–Indices describing Auroral Electrojets.

The indices used by the IRI model are the K_p and the a_p.

K_p is a 3–hr index that aims at describing the global level of "all irregular disturbances of the geomagnetic field caused by solar particle radiation within the 3–hr interval concerned" (Siebert & Meyer, 1996). It was introduced by Julius Bartels in 1938 and adopted by IAGA in 1951. K_p is derived from (currently) 13 sub–auroral magnetic observatories measurements. For each of these observatories, the disturbance level at that site is determined by measuring the range (i.e., the difference between the highest and lowest values) during 3–hr time intervals for the most disturbed horizontal magnetic field component, after removing the regular daily variation. The range is then converted to a *K* value of the given 3–hr interval, taking values between 0 (quietest) and 9 (most disturbed) on a quasi-logarithmic scale (Menvielle & Berthelier, 1991). The *K* values are then converted to a standardized number, denoted as K_s, using conversion tables based on the statistical properties of *K* at the observatory in consideration. K_s is given in a scale of thirds, ranging through 28 grades in the order: 0°, 0^+, 1^-, 1°, 1^+, 2^-, 2°, 2^+,…, 8^-, 8°, 8^+, 9^-, 9°. The planetary activity index, K_p, is the mean of the K_s values at each station.

A derived quantity is the 3–hr index a_p, which is a linearized version of K_p converted according to the values that are reported in Table 7.

K_p and a_p are calculated bi–weekly and are available since 1932.

Table 7
Correspondence Between Values of K_p and a_p Indices

K_p	0°	0+	1−	1°	1+	2−	2°	2+	3−	3°	3+	4−	4°	4+
a_p	0	2	3	4	5	6	7	9	12	15	18	22	27	32
K_p	5−	5°	5+	6−	6°	6+	7−	7°	7+	8−	8°	8+	9−	9°
a_p	39	48	56	67	80	94	111	132	154	179	207	236	300	400

Specifically, the IRI model makes use of the K_p index for the specification of auroral boundaries, and of the a_p index for both the electron density specification made in the auroral E region and the *fo*F2 storm model. The IRI file "apf107.dat" includes values of the a_p index.

Table 8 is a summary of the indices used in the different IRI sub-models.

9.4. User-Specified Parameters

As described in the sections before the ionospheric density and temperature profiles are characterized by several key parameters. If a user has measurements for some of these key parameters for a time period and location s/he is interested in, s/he can enter these directly into the IRI code. If this option is selected the modeled key parameters will be replaced by the measured parameters. This is a way to adjust the whole IRI profile to the specific conditions. Parameters for which this option is available include the F2-peak, F1-peak, E-peak, and D-region-inflection-point densities and the F2-peak, F1-peak, E-peak, and D-region-inflection-point heights. Instead of the electron densities a user can also use the corresponding plasma frequencies, which may be directly available from an ionosonde measurement. Instead of the F2-peak height a user can also provide the propagation factor $M(3000)F2$ which is measured by ionosondes and which is inversely proportional to the F2-peak height. A recent addition to the list of parameters a user can specify are the bottomside thickness and shape parameters B_0 and B_1. To avoid unrealistic profiles B_1 is constrained to the range 0.6–6 and B_1 input is accepted only if B_0 was also a user input.

There is also an option to use the well-established inverse relationship between electron temperature and electron density for updating the electron temperature in case electron density measurements are available. Brace and Theis (1978) had investigated this relationship with AE-C LP data and proposed the height-dependent formula

$$T_e^{BT} = 1051 + (17.07h - 2746)\exp\left(-5.122 \cdot 10^{4}h + 6.094 \cdot 10^{-6}N_e - 3.353 \cdot 10^{-8}h \cdot N_e\right). \quad (48)$$

Using AE-C and DE-2 LP data Bilitza et al. (1985) found that an additional dependence on solar activity had to be introduced and they obtained the following formulas using either the daily $F10.7_d$ solar flux index

$$T_e = T_e^{BT}\left[1 + \frac{0.117 + 2.02 \cdot 10^{-3} \cdot F10.7_d}{1 + \exp\left(\frac{-F10.7_d + 102.5}{5}\right)}\right], \quad (49)$$

or $F10.7_{81}$

$$T_e = T_e^{BT}\left[1 + \frac{0.123 + 1.69 \cdot 10^{-3} \cdot F10.7_{81}}{1 + \exp\left(\frac{-F10.7_{81} + 115}{10}\right)}\right]. \quad (50)$$

An IRI user who has electron density measurements available at any of the fixed heights that define the T_e profile, has the option to apply these formulas for determining the electron temperatures at the specific heights. The T_e profile is then constructed using the Booker approach with the updated T_e values.

Table 8
Summary of Solar, Ionospheric, and Geomagnetic Indices Used in the Different International Reference Ionosphere Sub-Models

Parameter	Region	Author and year	Indices
Electron Density	D region	Bilitza (1981a, 1981b)	R_{12}
		Friedrich et al. (2018)	$F10.7_d$
		Danilov et al. (1995)	$F10.7_d$, K_p
	E peak	Kouris and Muggleton (1973)	$F10.7_{365}$
		Mertens et al. (2013a, 2013b)	a_p
	F1 region	DuCharme et al. (1973)	R_{12}
		Scotto et al. (1997)	R_{12}
	Bottomside	Bilitza et al. (2000)	R_{12}
		Altadill et al. (2009)	R_{12}
	F peak	Jones and Gallet (1965)	IG_{12}
		Rush et al. (1989)	IG_{12}
		Fuller-Rowell et al. (2000)	a_p [a]
	*hm*F2	Bilitza et al. (1979)	R_{12}
		Altadill et al. (2013)	R_{12}
		Shubin (2015)	$F10.7_{81}$
	Topside	Rawer, Bilitza, and Ramakrishnan (1978) and Rawer, Bilitza, Ramakrishnan, and Sheikh (1978)	$F10.7_{365}$
		Bilitza (2004)	$F10.7_{365}$
		Nava et al. (2008)	R_{12}
		Bilitza and Xiong (2021)	$PF10.7$
	Spread-F	Abdu et al. (2003)	$F10.7_d$
Temperatures	T_e	Truhlik et al. (2012)	$PF10.7$
	T_i	Truhlik et al. (2021)	$PF10.7$
	T_n NRLMSISE-00	Picone et al. (2002)	$F10.7_d$, $F10.7_{81}$, a_p [b]
Ion composition and velocity	N_i ($h \leq 300$ km)	Richards et al. (2010)	$F10.7_d$, $F10.7_{81}$
	N_i ($h > 300$ km)	Truhlik et al. (2015)	$PF10.7$
	N_i ($h \leq 300$ km)	Danilov and Smirnova (1995)	$F10.7_{365}$
	N_i ($h > 300$ km)	Danilov and Yaichnikov (1985)	$F10.7_{365}$
	v_i	Fejer et al. (2008)	$F10.7_d$
Auroral oval	Boundaries	Y. Zhang et al. (2010)	K_p

[a]3-hr a_p for current time and the 12 preceding 3-hr a_p indices. [b]daily a_p, and 3-hr a_p for current time, the 3 preceding 3-hr a_p indices, the average of the next 8 3-hr indices, and again the average of the next eight indices.

10. Data Assimilation Into IRI and Real-Time IRI

Different data assimilation techniques have been applied with the aim to improve the IRI output. The goal is to move from the climatological representation provided by the standard IRI model to a description of real-time or past-time ionospheric weather conditions based on the ingestion of real-time or past-time measurements.

The earliest studies have focused on obtaining equivalent R_{12} or IG_{12} indices because of their basic role in determining the F2-peak height and density, respectively. An equivalent index is obtained by varying the model-driving index or indices until good agreement is achieved between data and model. Bilitza et al. (1997) used worldwide ionosonde *fo*F2 data from 1986 to 1989 to obtain equivalent *IG* indices in support of Geosat altimeter data analysis. Komjathy et al. (1998), Hernandez-Pajares et al. (2002), Migoya-Orué et al. (2015), Ssessanga et al. (2015), and Habarulema and Ssessanga (2016) used GNSS vTEC data to determine R_{12} and/or IG_{12} equivalent indices. Recently, Pignalberi et al. (2018b), besides reviewing the use of effective indices for ionospheric modeling,

proposed a new assimilation method to update the IRI model in the European region. Specifically, *fo*F2 and *M*(3000)F2 measurements are assimilated from several ionospheric stations to calculate effective values of indices R_{12} and IG_{12} and then these scattered values are interpolated by means of the geostatistical interpolation technique called universal Kriging method (Kitanidis, 1997; Oliver & Webster, 1990). Corresponding maps are then used as input to the IRI model, thus obtaining updated values of *fo*F2 and *M*(3000)F2, hence of *hm*F2. Pignalberi et al. (2019) have recently updated their procedure by using also vTEC values for the IRI updates. Y. Zhang et al. (2010) determine an effective K_p index by adjusting their auroral boundary model to the boundary identified during an auroral crossing of GUVI or SSUSI (see Section 7.1).

More recently, data assimilation into IRI has utilized more advanced mathematical tools to achieve a better representation of real-time conditions combining ground and space data sources. Schmidt et al. (2008) and Wenjing et al. (2015) represented the difference between GPS data and IRI with a multidimensional expansion in B-spline functions. Fridman et al. (2006) proposed a GPS Ionospheric Inversion (GPSII) assimilation model using the Tikhonov methodology (Tikhonov & Arsenin, 1977) with IRI as the background model. The Electron Density Assimilative Model (EDAM) of Angling et al. (2009) assimilates GPS data into IRI using weighted, damped least mean square. One of the most extensive efforts was undertaken by Yue et al. (2012) who used the Kalman filter technique to assimilate a large number of different datasets into IRI including GPS vTEC data, RO data from CHAMP, GRACE, COSMIC, Satelite de Aplicaciones Cientificas-C (SAC-C), Meteorological Operational Satellite-A (Metop-A), and TerraSAR-X, and Jason-1 and -2 altimeter vTEC measurements. They did this re-analysis for the time period 2002–2011 creating a valuable data source for space weather studies. Pezzopane et al. (2011), Pezzopane, Pietrella, et al. (2013), and Pietrella et al. (2018) first determine an effective sunspot number comparing IRI to ionosonde F2-peak parameter measurements and then apply an interpolation technique to assimilate into IRI the full electron density profile recorded by ionosondes. A regional three-dimensional ionospheric electron density specification over China and adjacent areas in the altitude range 100–900 km was developed by Aa et al. (2016) by applying a three-dimensional variational technique to assimilate GNSS observations from the Crustal Movement Observation Network of China and the International GNSS Service, and the ionospheric RO data from COSMIC satellites into IRI with very good validation results. An et al. (2019) represent global vTEC by assimilating satellite altimetry data from Jason−2/−3 and more than 300 global GNSS stations from 2014 to 2018 into the a priori IRI using a two-dimensional spherical harmonic expansion in a sun-fixed geomagnetic reference frame.

Galkin et al. (2012, 2018, 2020) have developed the IRI-based Real-Time Assimilative Mapping (IRTAM, http://giro.uml.edu/RTAM) system that assimilates *fo*F2, *hm*F2, B_0, and B_1 measurements from the ground-based GIRO ionosonde network into IRI. IRTAM uses the CCIR (1967) model functions to represent the difference between *fo*F2 data and model, generating real-time maps of *fo*F2 every 15 min. An example of the IRTAM *fo*F2 output is shown in Figure 16.

The IRTAM technique is also applied for assimilating GIRO measurements of *hm*F2, B_0 and B_1 into IRI, bringing IRI ever closer to representing the real-time conditions. For the IRTAM-determination of *hm*F2, the work of Brunini et al. (2013) was helpful because they had already used the CCIR formalism to globally represent the IRI *hm*F2. It is worth highlighting that IRTAM uses a low-pass temporal filter as a part of its diurnal harmonics analysis to smooth out data jitter, outliers, and low-confidence values. Another recent improvement is the inclusion of a linear trend term so that the model parameter does not have to return to the same value after 24 hr.

Pignalberi, Pietrella, and Pezzopane (2021) performed a detailed comparison between IRI and IRTAM, based on the F2-layer peak characteristics *fo*F2 and *hm*F2 recorded by 40 ground-based ionosondes spread all over the world from 2000 to 2019 and from COSMIC satellites from 2006 to 2018. The main outcome of their study is that nearby the assimilated ionosonde locations, IRTAM improves the IRI *fo*F2 and *hm*F2 modeling, especially *fo*F2, while away from the participating stations, the IRI and IRTAM outputs for *fo*F2 are similar and the IRI *hm*F2 description is always more accurate and precise than the IRTAM one.

Efforts are underway to further improve the real-time IRI by applying the IRTAM approach to GNSS vTEC data (Froń et al., 2020; Galkin et al., 2022).

The IRI software includes the necessary subroutines (irirtam.for) to facilitate the use of the IRTAM coefficients in the standard IRI code.

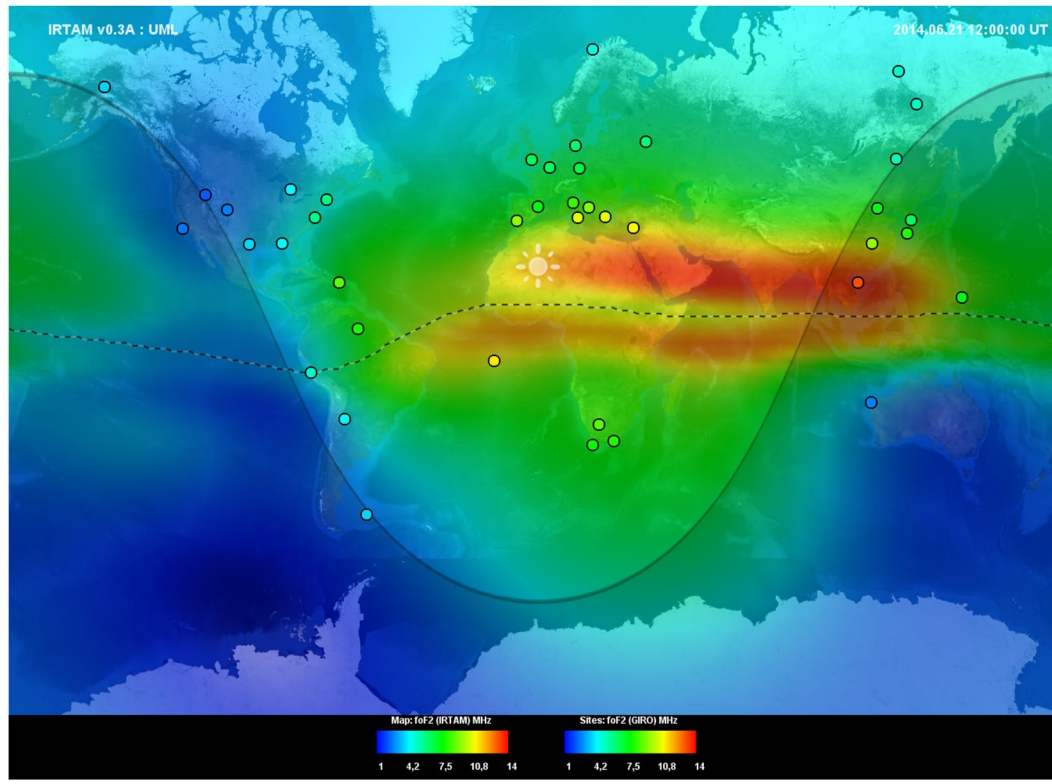

Figure 16. Example of *fo*F2 global map as generated by IRTAM. Circles represent the location of ionosonde stations used to generate the map, and the color inside the circles indicates the measured *fo*F2 value.

11. IRI Achievements

IRI is unanimously recognized and recommended as the standard for the ionosphere. COSPAR and URSI, the two international unions that started the IRI project, have both recognized IRI as the international standard for the ionosphere and recommended its usage to its member states. The European Cooperation for Space Standardization has elected IRI as its reference model for the ionosphere. The most important endorsement came with the election of IRI to become the ISO standard for the ionosphere in April 2014 and its revision in February 2022 (ISO 16457, 2022).

Model assessment studies undertaken by independent and impartial evaluators highlighted IRI's excellent performance. Shim et al. (2011, 2012) were tasked with a systematic assessment of ionosphere/thermosphere models in the framework of the Coupling, Energetics, and Dynamics of Atmospheric Regions program sponsored by the National Science Foundation. Out of the eight models included in the study, IRI was the only empirical model, the others were theoretical models. The analysis considered *Nm*F2 and *hm*F2 from ionosondes and COSMIC RO and electron density along the CHAMP orbit for several event periods using a variety of performance measures and skill scores. IRI was the clear overall winner. Shim et al. (2017, 2018) continued their model assessment effort with the storms that occurred on 14–15 December 2006 (American Geophysical Union storm event) and on 17 March 2013, respectively. Data used for these two studies were ionosonde and GPS vTEC measurements. The results showed that the IRI model is on par with the best theoretical and assimilative models in predicting *fo*F2.

The main IRI papers are highly cited in a wide range of scientific journals covering space physics, space weather, geodesy, Earth science, applied optics, aeronautics, radio science, communications, computers, engineering, plasma science, cosmic research, and solar physics. Table 9 lists the percentage of papers that have used IRI for each year since 2009 in the Journal of Geophysical Research (JGR)—Space Physics, Space Weather (SW), and Radio Science (RS).

The table illustrates the continuous important service the IRI model provides to the space physics community over many years. It also highlights the steady increase in usage in recent years especially prominent in the case of JGR and RS. For a single model to be used in almost every 12th JGR paper, every 10th SW paper and every sixth RS paper is no doubt a singular achievement.

Table 9
Percentage of Papers per Year That Acknowledge Usage of the IRI Model in the Journal of Geophysical Research (JGR), Space Weather (SW), and Radio Science (RS)

Year	JGR	SW	RS
2009	5.0	0	10.5
2010	5.6	5.6	11.8
2011	7.1	8.1	14.2
2012	7.6	4.8	13.8
2013	5.1	2.3	8.2
2014	6.6	5.7	10.7
2015	8.3	1.6	9.1
2016	6.5	2.2	13.2
2017	4.4	6.3	11.8
2018	7.6	7.9	16.4
2019	7.4	6.1	15.4
2020	7.5	13.4	16.4
2021	8.0	9.8	17.3

In fact, IRI is cited in a wide range of scientific journals besides the ones listed in Table 9. This includes Advances in Space Research, Advances in Radio Science, Annales Geophysicae, Applied Optics, Astrophysics and Space Science, Atmosphere, Chinese Journal of Aeronautica, Computers & Geosciences, Computer Physics Communications, Cosmic Research, Earth Planets and Space, Geochimica et Cosmochimica Acta, Geodesy and Geodynamics, Geomagnetism and Aeronomy, GPS Solutions, Journal of Asian Earth Science, Journal of Atmospheric and Solar-Terrestrial Physics, Journal of Geodesy, Journal of Space Weather & Space Climate, Planetary and Space Science, Plasma Science and Technology, Remote Sensing, Solar Physics, Space Science Reviews, and Surveys in Geophysics.

12. Conclusion

The International Reference Ionosphere (IRI) is the internationally recognized standard for Earth's ionosphere and is applied for science, engineering and educational purposes by a large user community. The preceding pages provided a comprehensive description of the model with the goal of supporting the scientific understanding and operational use of the model, and are also meant as a guide for users who are interested in a deeper understanding of the model architecture and its mathematical formalism.

The paper also presents the latest update of the model, IRI-2020, which includes the following major improvements:

1. A more accurate representation of the solar activity variation of the topside electron density based on ISIS 1,2, Alouette 1,2, CHAMP, GRACE, and Swarm satellite measurements (Bilitza & Xiong, 2021), as described in Section 3.1.2.
2. An updated model for the D-region electron density based on the work of Friedrich et al. (2018) combining their compilation of reliable rocket measurements with a theoretical ion-chemical model, as described in Section 3.8.2.
3. A new model for the ionospheric ion temperature based on a large volume of in situ measurements from many satellites that were first calibrated with simultaneous ISR measurements (Truhlik et al., 2021), as described in Section 5.3.2.
4. The equatorial vertical ion drift model of Fejer et al. (2008) based on 5 years of ROCSAT-1 in situ measurements, as described in Section 6.1.

IRI-related activities and community outreach are continuing with the bi-annual IRI Workshops that in recent years included a strong capacity-building component by including over 30 students from developing countries in the framework of the COSPAR Capacity Building Workshop Program. Most recently these were well-attended workshops at the National Central University in Taiwan in 2017 and at Frederick University in Cyprus in 2019.

A special focus in recent years and for future activities is the work on a Real-Time IRI, with the goal of progressing from the prediction of ionospheric climate to ionospheric weather forecast. There is quite a number of studies that assimilated a variety of data into a background IRI with the intent of reproducing real-time conditions (see Section 10 for details). The IRI-based Real-Time Assimilative Mapping (IRTAM) effort of Galkin et al. (2018, 2020) is very promising and has great potential. Recent activities have focused on applying the IRTAM formalism to GNSS vTEC data in collaboration with the International GNSS Service (IGS) Iono group (Froń et al., 2020; Galkin et al., 2022).

There are plans for inclusion of several new models in a future version of IRI. This includes the model of Blanch and Altadill (2012) describing ionospheric storm effects on the F2-peak height *hm*F2 and the model of Shubin and Deminov (2019) describing *fo*F2 including storm effects and the main ionospheric trough. Both models require inputs of solar wind parameters which is planned with the help of access to the OMNI database (J. H. King & Papitashvili, 2005). Work has begun on developing a model for the occurrence probability of sporadic E based on the large database established by Arras et al. (2008). High priority is also given to the inclusion of an improved model for the occurrence probability of spread-F, since the current model is limited to the Brazilian

longitude sector. Similar global models for scintillation and plasma bubble occurrences are also high on the list, including, and most desirable, a comprehensive study of the correlation between these different phenomena.

Finally, we are happy to see the steady increase in IRI usage as documented in Table 9 by the yearly percentages of science papers using IRI.

Appendix A: Epstein Functions, Booker Function, and HPOL Function

IRI modeling has made use of a family of functions introduced by S. Epstein (Bilitza, 1990; Rawer & Bilitza, 1989). These functions have been used to represent altitudinal variations as well as special latitudinal and diurnal features of IRI parameters. The first three members of the Epstein family of functions are shown in Figure A1 and defined as

$$\mathrm{Eps}_{-1}(x) = \ln(1 + e^{x}), \tag{A1}$$

$$\mathrm{Eps}_{0}(x) = \frac{1}{1 + e^{-x}}, \tag{A2}$$

$$\mathrm{Eps}_{1}(x) = \frac{e^{x}}{(1 + e^{x})^{2}}, \tag{A3}$$

with

$$x(h; HX, SC) = \frac{h - HX}{SC}, \tag{A4}$$

and the relation between these functions is

$$\mathrm{Eps}_{i+1}(x) = \frac{\mathrm{dEps}_{i}(x)}{\mathrm{d}x}. \tag{A5}$$

Eps_{-1} describes a transition, Eps_{0} a step, and Eps_{1} a layer, and each of these functions is centered at $x = 0$ ($h = HX$); SC is a thickness parameter that describes the width of the specific feature. Figure A2 shows Eps_{0}, Eps_{-1} and Eps_{1} for different values of HX and SC.

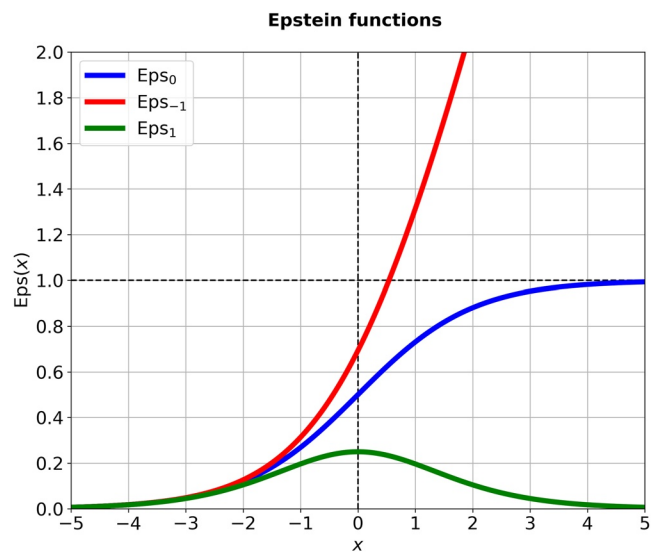

Figure A1. Epstein functions.

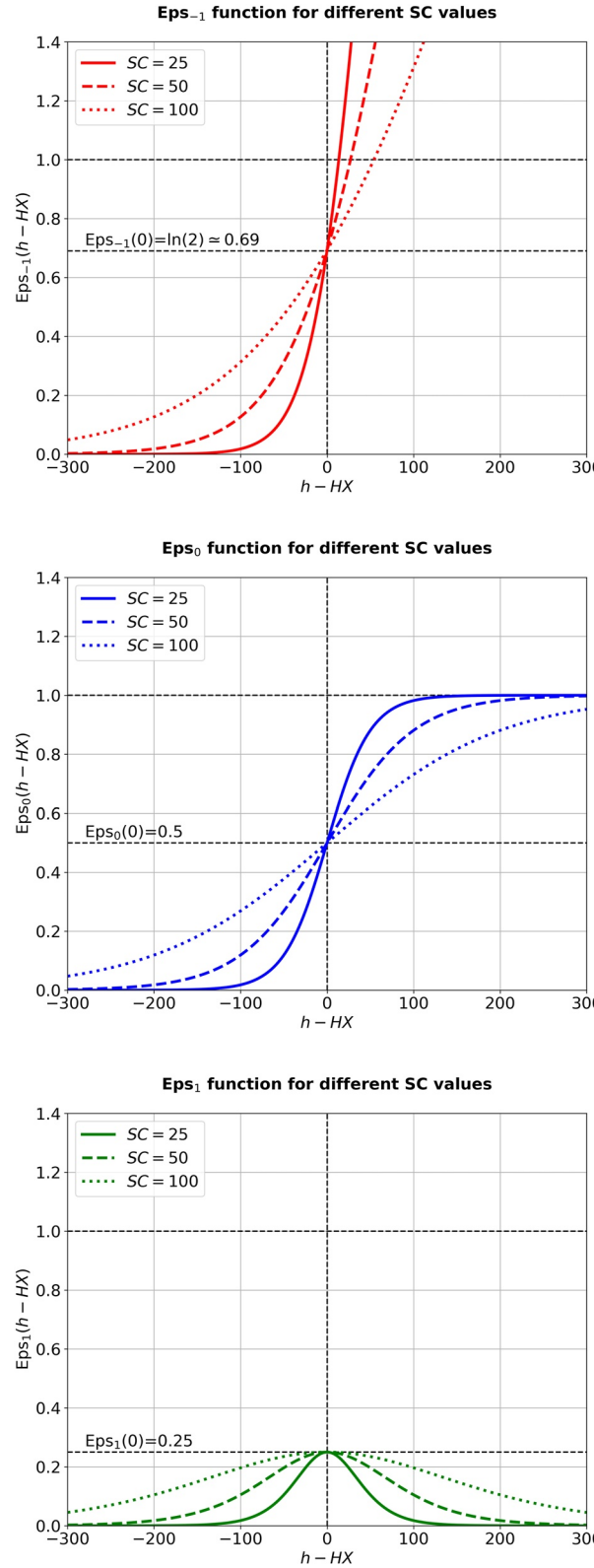

Figure A2. (top) Eps_{-1}, (middle) Eps_0, (bottom) Eps_1 for different values of *SC*.

Booker (1977) used the Epstein functions for a unique approach to represent data profiles. First, the profile is divided in sections of almost constant gradient (the skeleton) and then the Epstein step function Eps_0 is used to represent the transition from one gradient to the next. For a profile with N sections of constant gradients g_i one gets the gradient profile as

$$g(h) = g_1 + \sum_{i=1}^{N} (g_{i+1} - g_i)\,\mathrm{Eps}_0\,(h; HX_i, SC_i)\,, \tag{A6}$$

with the section boundaries HX_i and the transition thicknesses SC_i. Integrating from h_0 (which is the base point of the profile) to h we obtain the Booker function

$$\begin{aligned}\mathrm{B}\,(h; h_0, g_i, HX_i, SC_i) = \mathrm{B}_0 + (h - h_0)\,g_1 + \sum_{i=1}^{N} (g_{i+1} - g_i)\,SC_i\,\left[\mathrm{Eps}_{-1}\,(h; HX_i, SC_i)\right. \\ \left. - \mathrm{Eps}_{-1}\,(h_0; HX_i, SC_i)\right]\,,\end{aligned} \tag{A7}$$

with the integration constant $B_0 = \mathrm{B}(h_0; h_0, g_i, HX_i, SC_i)$. Suitable transition thicknesses SC_i have to be found by trial and error. Small values produce a profile closer to the skeleton than to the real profile; large values provide greater smoothness but could cause interference between adjacent step functions resulting in larger differences with respect to the real profile. Best results are obtained with $D/20 < SC_i < D/10$ where D is the height range of the smallest of the two adjacent subsections. Care has to be taken in choosing the base point (integration boundary) h_0. It should not be located in one of the highly variable transition regions. The best choice is a h_0 from a region where the skeleton and the original profile are close to each other. Figure A3 shows an example of the Booker function.

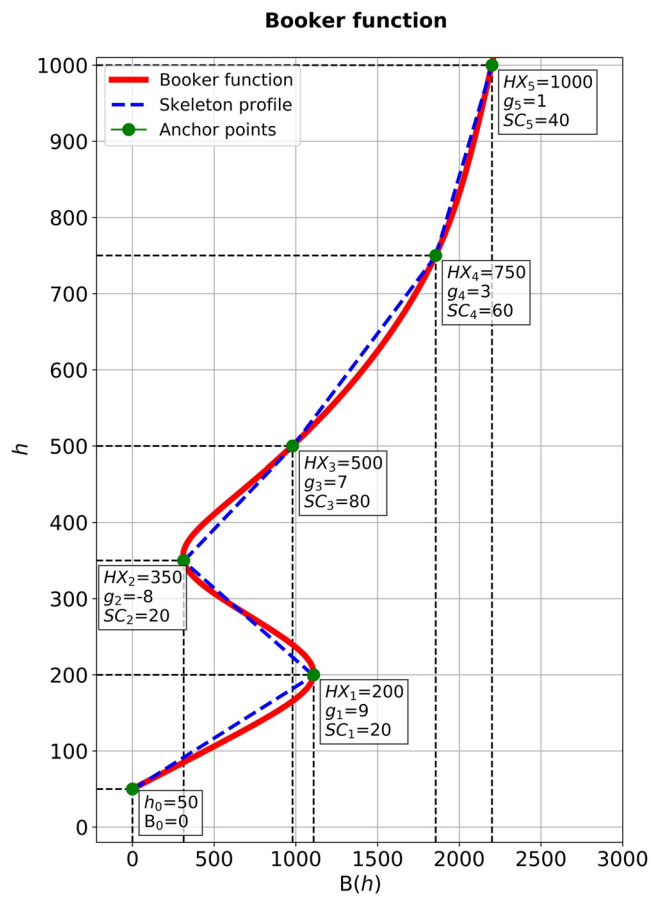

Figure A3. Example of Booker function.

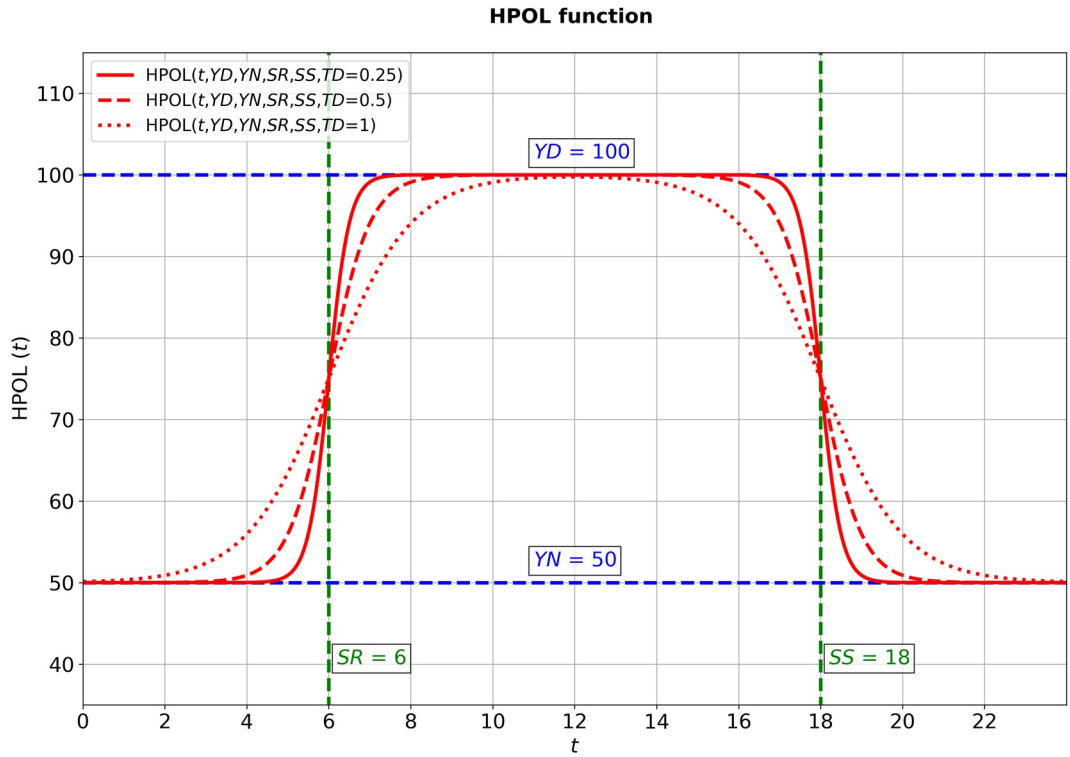

Figure A4. Different examples of HPOL functions.

Epstein step functions are also used to describe a simple transition from a constant day value to a constant night value for IRI parameters. This is achieved with the combination of two step functions

$$\mathrm{HPOL}(t; YD, YN, SR, SS, TD) = YN + (YD - YN) \cdot \mathrm{Eps}_0(t; SR, TD) + (YN - YD) \cdot \mathrm{Eps}_0(t; SS, TD), \quad \text{(A8)}$$

resulting in a function that varies continuously with local time t from a constant nighttime value YN to a constant daytime value YD. The steps occur at the local times of sunrise (SR) and sunset (SS) and the step width is determined by TD (usually 1 hr) (see Figure A4).

Acronyms

AE	Atmospheric Explorer
CCIR	Consultative Committee on International Radio
CHAMP	Challenging Minisatellite Payload
CIRA	COSPAR International Reference Atmosphere
C/NOFS	Communications/Navigation Outage Forecasting System
COSMIC	Constellation Observing System for Meteorology, Ionosphere, and Climate
COSPAR	Committee on SPAce Research
DE	Dynamics Explorer
DMSP	Defense Meteorological Satellites Program
E-CHAIM	Empirical Canadian High Arctic Ionospheric Model
EIA	equatorial ionization anomaly
EUV	extreme ultraviolet
FIRI	Faraday IRI
FLIP	Field Line Interhemispheric Plasma
FSF	frequency spread-F
GCPM	Global Core Plasma Model
GIRO	Global Ionospheric Radio Observatory

GNSS	Global Navigation Satellite System
GPS	Global Positioning System
GRACE	Gravity Recovery and Climate Experiment
GUVI	Global Ultraviolet Imager
HF	high frequency
IAGA	International Association of Geomagnetism and Aeronomy
IGRF	International Geomagnetic Reference Field
IMAGE	Imager for Magnetopause-to-Aurora Global Exploration
IMAZ	Ionospheric Model for Auroral Zone
IMF	interplanetary magnetic field
IRI	International Reference Ionosphere
IRTAM	IRI Real-Time Assimilative Mapping
ISIS	International Satellites for Ionospheric Studies
ISO	International Standardization Organization
ISR	incoherent scatter radar
ISS	Ionosphere Sounding Satellite
ITU	International Telecommunication Union
LP	Langmuir Probe
LT	local time
LTH	lower transition height
MARP	Monthly Averaged Representative Profile
MSISE	Mass Spectrometer Incoherent Scatter radar Extended
NRLMSISE	Naval Research Laboratory Mass Spectrometer Incoherent Scatter radar Extended
ROCSAT	Republic of China satellite
RPA	Retarding Potential Analyzer
RPI	Radio Plasma Imager
RSF	range spread-F
RT	Rayleigh-Taylor
SA	solar activity
SDMF2	Satellite and Digisonde Model of the F2 layer
SIDC	Solar Influences Data analysis Center
SW	stratospheric warming
TIMED	Thermosphere Ionosphere Mesosphere Energetics and Dynamics
URSI	International Union of Radio Science
UT	universal time
UTH	upper transition height
VHF	very high frequency
VLF	very low frequency
vTEC	vertical total electron content
WA	winter absorption anomaly

Glossary

Bottomside	the part of the vertical electron density profile below the F2-region peak.
Equatorial ionization anomaly	The low-latitude ionospheric region characterized by two latitudinal maxima (crests) on both side of the magnetic equator at lower altitudes, which then merge into a single maximum at the equator at higher altitudes.
$F10.7_d$	the daily solar radio flux at 10.7 cm wavelength.
$F10.7_{81}$	the 81-day running mean of solar flux $F10.7$.
$F10.7_{365}$	the 365-day running mean of solar flux $F10.7$.
*fo*D	the critical frequency associated with the D-region inflection point.
*fo*E	the critical frequency associated with the E-region peak.
*fo*F1	the critical frequency associated with the F1-region peak.
*fo*F2	the critical frequency associated with the F2-region peak.

*hm*D	the real height of the D-region inflection point.
*hm*E	the real height of the E-region peak.
*hm*F1	the real height of the F1-region peak.
*hm*F2	the real height of the F2-region peak.
IG	the Ionosonde Global monthly index based on noontime *fo*F2 ionosonde measurements recorded at four reference stations two from the Southern Hemisphere (Port Stanley/UK and Canberra/Canada) and two from the Northern Hemisphere (Kokubunji/Japan and Chilton/UK).
IG_{12}	the 12-month running-mean of the ionospheric index *IG*.
Ionosonde	a high frequency radar that sends short pulses of radio energy vertically into the ionosphere. These pulses are reflected back toward the ground and the ionosonde records the delay time between transmission and reception of pulses. By varying the carrier frequency of pulses typically from f = 1–20 MHz, the delay time $\Delta\tau(f)$ at different frequencies is measured. This record is named ionogram and is usually presented in the form of a graph, where normally in place of the delay time $\Delta\tau(f)$ the virtual height $h'(f) = \frac{1}{2}\,\Delta\tau(f)$ c is plotted, where c is the free-space speed of light.
M(3000)F2	the obliquity factor for a distance of 3,000 km. Defined as *MUF*(3000)F2/*fo*F2, where *MUF*(3000)F2 is the highest frequency that, refracted in the ionosphere, can be received at a distance of 3,000 km.
*Nm*D	the electron density of the D-region inflection point.
*Nm*E	the electron density of the E-region peak.
*Nm*F1	the electron density of the F1-region peak.
*Nm*F2	the electron density of the F2-region peak.
R	the daily solar index related to the daily number of spots and spots groups observed on the Sun.
R_{12}	the 12-month running-mean of monthly sunspot number of *R*.
Topside	the part of the vertical electron density profile above the F2-region peak.

Data Availability Statement

As a review, this paper does not rely on new data collections. Data for the majority of the satellite missions listed in Table 1 are available from NASA's Space Physics Data Facility (https://spdf.gsfc.nasa.gov/). The ionosonde data used to produce Figure 4 are available from the Digital Ionogram Database (http://ulcar.uml.edu/DIDBase/) of the Global Ionosphere Radio Observatory in Lowell, MA. The geomagnetic indices used to produce Figure 4 are available from the NASA's Space Physics Data Facility of the Goddard Space Flight Center (https://spdf.gsfc.nasa.gov/pub/data/omni/high_res_omni/). Radio occultation data used to produce Figure 5 are available from the COSMIC Data Analysis and Archive Center (CDAAC, https://data.cosmic.ucar.edu/gnss-ro/cosmic1/). Ionosonde data used to produce Figure 8 are available from the Electronic Space Weather upper atmosphere database (eSWua)—HF data, version 1.0, https://doi.org/10.13127/eswua/hf. Incoherent scatter radar data used to produce Figure 13 are available from the portal at http://cedar.openmadrigal.org.

Acknowledgments
A special thank you and acknowledgement goes to the members of the COSPAR/URSI Working Group on the International Reference Ionosphere. They have contributed to the success and continuous improvement of the model. A. Pignalberi was partially supported by the Italian MIUR-Progetti di Rilevante Interesse Nazionale Grant 2017APKP7T on Circumterrestrial Environment: Impact of Sun–Earth Interaction. V. Truhlik was supported by Grant LTAUSA17100 of the Ministry of Education, Youth and Sports of the Czech Republic. The IRI homepage at http://irimodel.org provides open access to the FORTRAN model code of all major version of the model, to online computations of IRI parameters, and to information about IRI members, workshops, and publications. The authors thank Michael Mendillo and two additional anonymous reviewers for their valuable inputs.

References

Aa, E., Liu, S., Huang, W., Shi, L., Gong, J., Chen, Y., et al. (2016). Regional 3-D ionospheric electron density specification on the basis of data assimilation of ground-based GNSS and radio occultation data. *Space Weather*, *14*(6), 433–448. https://doi.org/10.1002/2016SW001363

Abdu, M., Souza, J., Batista, I., & Sobral, J. (2003). Equatorial spread F statistics and empirical representation for IRI: A regional model for the Brazilian longitude sector. *Advances in Space Research*, *31*(3), 703–716. https://doi.org/10.1016/S0273-1177(03)00031-0

Abdu, M. A. (2001). Outstanding problems in the equatorial ionosphere thermosphere electrodynamics relevant to spread F. *Journal of Atmospheric and Solar-Terrestrial Physics*, *63*(9), 869–884. https://doi.org/10.1016/S1364-6826(00)00201-7

Abdu, M. A. (2020). Equatorial F region irregularities. In M. Materassi, B. Forte, A. J. Coster, & S. Skone (Eds.), *The dynamical ionosphere* (pp. 169–178). Elsevier. chapter 12. https://doi.org/10.1016/B978-0-12-814782-5.00012-1

Abdu, M. A., Batista, I. S., Brum, C. G. M., MacDougall, J. W., Santos, A. M., de Souza, J. R., & Sobral, J. H. A. (2010). Solar flux effects on the equatorial evening vertical drift and meridional winds over Brazil: A comparison between observational data and the IRI model and the HWM representations. *Advances in Space Research*, *46*(8), 1078–1085. https://doi.org/10.1016/j.asr.2010.06.009

Abdu, M. A., Bittencourt, J. A., & Batista, I. S. (1981). Magnetic declination control of the equatorial F region dynamo field development and spread-F. *Journal of Geophysical Research*, *86*(A13), 11443–11446. https://doi.org/10.1029/JA086iA13p11443

Adeniyi, J., Bilitza, D., Radicella, S., & Willoughby, A. (2003). Equatorial F2-peak parameters in the IRI model. *Advances in Space Research*, *31*(3), 507–512. https://doi.org/10.1016/S0273-1177(03)00039-5

Adeniyi, J. O., & Radicella, S. M. (1998). Diurnal variation of ionospheric profile parameters B0 and B1 for an equatorial station at low solar activity. *Journal of Atmospheric and Solar-Terrestrial Physics*, *60*(3), 381–385. https://doi.org/10.1016/S1364-6826(97)00118-1

Alfonsi, L., Spogli, L., Pezzopane, M., Romano, V., Zuccheretti, E., De Franceschi, G., et al. (2013). Comparative analysis of spread-F signature and GPS scintillation occurrences at Tucuman, Argentina. *Journal of Geophysical Research: Space Physics*, *118*(7), 4483–4502. https://doi.org/10.1002/jgra.50378

Alken, P., Thébault, E., Beggan, C. D., Amit, H., Aubert, J., Baerenzung, J., et al. (2021). International geomagnetic reference field: The thirteenth generation. *Earth Planets and Space*, *73*(1), 49. https://doi.org/10.1186/s40623-020-01288-x

Altadill, D., Arrazola, D., Blanch, E., & Buresova, D. (2008). Solar activity variations of ionosonde measurements and modeling results. *Advances in Space Research*, *42*(4), 610–616. https://doi.org/10.1016/j.asr.2007.07.028

Altadill, D., Magdaleno, S., Torta, J. M., & Blanch, E. (2013). Global empirical models of the density peak height and of the equivalent scale height for quiet conditions. *Advances in Space Research*, *52*(10), 1756–1769. https://doi.org/10.1016/j.asr.2012.11.018

Altadill, D., Torta, J. M., & Blanch, E. (2009). Proposal of new models of the bottom-side B0 and B1 parameters for IRI. *Advances in Space Research*, *43*(11), 1825–1834. https://doi.org/10.1016/j.asr.2008.08.014

An, X., Meng, X., Jiang, W., Chen, H., He, Q., & Xi, R. (2019). Global ionosphere estimation based on data fusion from multisource: Multi-GNSS, IRI model, and satellite altimetry. *Journal of Geophysical Research: Space Physics*, *124*(7), 6012–6028. https://doi.org/10.1029/2019JA026896

Angling, M. J., Shaw, J., Shukla, A. K., & Cannon, P. S. (2009). Development of an HF selection tool based on the Electron Density Assimilative Model near-real-time ionosphere. *Radio Science*, *44*(1), RS0A13. https://doi.org/10.1029/2008RS004022

Aponte, N., Brum, C. G. M., Sulzer, M. P., & Gonzalez, S. A. (2013). Measurements of the O^+ to H^+ transition height and ion temperatures in the lower topside ionosphere over Arecibo for equinox conditions during the 2008–2009 extreme solar minimum. *Journal of Geophysical Research: Space Physics*, *118*(7), 4465–4470. https://doi.org/10.1002/jgra.50416

Araujo-Pradere, E., Fuller-Rowell, T. J., & Bilitza, D. (2003). Validation of the STORM response in IRI2000. *Journal of Geophysical Research*, *108*(A3), 1120. https://doi.org/10.1029/2002JA009720

Araujo-Pradere, E. A., Buresova, D., Fuller-Rowell, D. J., & Fuller-Rowell, T. J. (2013). Initial results of the evaluation of IRI hmF2 performance for minima 22–23 and 23–24. *Advances in Space Research*, *51*(4), 630–638. https://doi.org/10.1016/j.asr.2012.02.010

Araujo-Pradere, E. A., & Fuller-Rowell, T. J. (2001). Evaluation of the STORM time ionospheric empirical model for the Bastille Day event. *Solar Physics*, *204*(1), 317–324. https://doi.org/10.1023/A:1014250604073

Araujo-Pradere, E. A., & Fuller-Rowell, T. J. (2002). STORM: An empirical storm-time ionospheric correction model, 2, Validation. *Radio Science*, *37*(5), 4-1–4-14. https://doi.org/10.1029/2002RS002620

Araujo-Pradere, E. A., Fuller-Rowell, T. J., & Bilitza, D. (2004). Empirical Ionospheric Correction Model (STORM) response in IRI2000 and challenges for empirical modeling in the future. *Radio Science*, *39*(1), RS1S24. https://doi.org/10.1029/2002RS002805

Araujo-Pradere, E. A., Fuller-Rowell, T. J., & Codrescu, M. V. (2002). STORM: An empirical storm-time ionospheric correction model 1. Model description. *Radio Science*, *37*(5), 3-1–3-12. https://doi.org/10.1029/2001RS002467

Arikan, F., Sezen, U., & Gulyaeva, T. L. (2019). Comparison of IRI-2016 F2 layer model parameters with ionosonde measurements. *Journal of Geophysical Research*, *124*(10), 8092–8109. https://doi.org/10.1029/2019JA027048

Arras, C., Wickert, J., Beyerle, G., Heise, S., Schmidt, T., & Jacobi, C. (2008). A global climatology of ionospheric irregularities derived from GPS radio occultation. *Geophysical Research Letters*, *35*(14), L14809. https://doi.org/10.1029/2008GL034158

Balan, N., Bailey, G. J., Jenkins, B., Rao, P. B., & Moffet, J. (1994). Variations of ionospheric ionization and related solar fluxes during an intense solar cycle. *Journal of Geophysical Research*, *99*(A2), 2243–2253. https://doi.org/10.1029/93JA02099

Banks, P. M. (1967). Ion temperature in the upper atmosphere. *Journal of Geophysical Research*, *72*(13), 3365–3385. https://doi.org/10.1029/JZ072i013p03365

Batista, I. S., Abdu, M. A., & Bittencourt, J. A. (1986). Equatorial F-region vertical plasma drifts: Seasonal and longitudinal asymmetries in the American sector. *Journal of Geophysical Research*, *91*(A11), 12055–12064. https://doi.org/10.1029/JA091iA11p12055

Bent, R. B., Llewellyn, S. K., & Walloch, M. K. (1972). Description and evaluation of the Bent ionospheric model. *Report SAMSO-TR* (Vol. *1*, pp. 72–239).

Bilitza, D. (1981a). Electron density in the D-region as given by the International Reference Ionosphere. In K. Rawer, J. V. Lincoln, & R. O. Conkright (Eds.), *International Reference Ionosphere-IRI 79, World Data Center A for Solar-Terrestrial Physics*. *Report UAG-82, 245* (pp. 7–10).

Bilitza, D. (1981b). Models for ionospheric electron and ion temperature. In K. Rawer, J. V. Lincoln, & R. O. Conkright (Eds.), *International Reference Ionosphere-IRI 79, World Data Center A for Solar-Terrestrial Physics*. *Report UAG-82, 245* (pp. 11–16).

Bilitza, D. (1985a). Comparison of measured and predicted F2 peak altitudes. *Advances in Space Research*, *5*(10), 29–32. https://doi.org/10.1016/0273-1177(85)90176-0

Bilitza, D. (1985b). Electron density in the equatorial topside. *Advances in Space Research*, *5*(10), 15–19. https://doi.org/10.1016/0273-1177(85)90174-7

Bilitza, D. (1985c). Implementation of the new electron temperature model in IRI. *Advances in Space Research*, *5*(10), 117–122. https://doi.org/10.1016/0273-1177(85)90193-0

Bilitza, D. (1986). International reference ionosphere: Recent developments. *Radio Science*, *21*(3), 343–346. https://doi.org/10.1029/RS021i003p00343

Bilitza, D. (1990). *International Reference Ionosphere 1990*. National Space Science Data Center, Report 90-22. Retrieved from https://irimodel.org/docs/IRI1990pp0-84.pdf

Bilitza, D. (1991). The use of transition height for the representation of the ion composition. *Advances in Space Research*, *11*(10), 183–186. https://doi.org/10.1016/0273-1177(91)90341-G

Bilitza, D. (1995). Including auroral boundaries in the IRI model. *Advances in Space Research*, *16*(1), 13–16. https://doi.org/10.1016/0273-1177(95)00093-T

Bilitza, D. (1997). International reference ionosphere – Status 1995/96. *Advances in Space Research*, *20*(9), 1751–1754. https://doi.org/10.1016/S0273-1177(97)00584-X

Bilitza, D. (2001). International Reference Ionosphere 2000. *Radio Science*, *36*(2), 261–275. https://doi.org/10.1029/2000RS002432

Bilitza, D. (2004). A correction for the IRI topside electron density model based on Alouette/ISIS topside sounder data. *Advances in Space Research*, *33*(6), 838–843. https://doi.org/10.1016/j.asr.2003.07.009

Bilitza, D. (2009). Evaluation of the IRI-2007 model options for the topside electron density. *Advances in Space Research*, *44*(6), 701–706. https://doi.org/10.1016/j.asr.2009.04.036

Bilitza, D. (2018). IRI the International Standard for the Ionosphere. *Advances in Radio Science*, *16*, 1–11. https://doi.org/10.5194/ars-16-1-2018

Bilitza, D., Altadill, D., Truhlik, V., Shubin, V., Galkin, I., Reinisch, B., & Huang, X. (2017). International Reference Ionosphere 2016: From ionospheric climate to real-time weather predictions. *Space Weather*, *15*(2), 418–429. https://doi.org/10.1002/2016SW001593

Bilitza, D., Altadill, D., Zhang, Y., Mertens, C., Truhlik, V., Richards, P., et al. (2014). The International Reference Ionosphere 2012 – A model of international collaboration. *Journal of Space Weather and Space Climate*, *4*, A07. https://doi.org/10.1051/swsc/2014004

Bilitza, D., Bhardwaj, S., & Koblinsky, C. (1997). Improved IRI predictions for the GEOSAT time period. *Advances in Space Research*, *20*(9), 1755–1760. https://doi.org/10.1016/S0273-1177(97)00585-1

Bilitza, D., Brace, L. H., & Theis, R. F. (1985). Modelling of ionospheric temperature profiles. *Advances in Space Research*, *5*(7), 53–58. https://doi.org/10.1016/0273-1177(85)90356-4

Bilitza, D., Brown, S. A., Wang, M. Y., Souza, J. R., & Roddy, P. A. (2012). Measurements and IRI model predictions during the recent solar minimum. *Journal of Atmospheric and Solar-Terrestrial Physics*, *86*, 99–106. https://doi.org/10.1016/j.jastp.2012.06.010

Bilitza, D., & Eyfrig, R. (1978). Model zur Darstellung der Höhe des F2-Maximums mit Hilfe des M(3000)F2 Wertes des CCIR (German). *Kleinheubacher Berichte*, *21*, 167–174.

Bilitza, D., & Hoegy, W. R. (1990). Solar activity variations of ionospheric plasma temperatures. *Advances in Space Research*, *10*(8), 81–90. https://doi.org/10.1016/0273-1177(90)90190-B

Bilitza, D., McKinnell, L.-A., Reinisch, B., & Fuller-Rowell, T. (2011). The international reference ionosphere today and in the future. *Journal of Geodesy*, *85*(12), 909–920. https://doi.org/10.1007/s00190-010-0427-x

Bilitza, D., Radicella, S., Reinisch, B., Adeniyi, J., Mosert, M., Zhang, S., & Obrou, O. (2000). New B0 and B1 models for IRI. *Advances in Space Research*, *25*(1), 89–95. https://doi.org/10.1016/S0273-1177(99)00902-3

Bilitza, D., Rawer, K., & Pallaschke, S. (1988). Study of ionospheric models for satellite orbit determination. *Radio Science*, *23*(3), 223–232. https://doi.org/10.1029/RS023i003p00223

Bilitza, D., Rawer, K., Pallaschke, S., Rush, C. M., Matuura, N., & Hoegy, W. R. (1987). Progress in modeling the ionospheric peak and topside electron density. *Advances in Space Research*, *7*(6), 5–12. https://doi.org/10.1016/0273-1177(87)90265-1

Bilitza, D., & Reinisch, B. W. (2008). International reference ionosphere 2007: Improvements and new parameters. *Advances in Space Research*, *42*(4), 599–609. https://doi.org/10.1016/j.asr.2007.07.048

Bilitza, D., Sheik, N., & Eyfrig, R. (1979). A global model for the height of the F2-peak using M3000 values from the CCIR numerical map. *Telecommunication Journal*, *46*, 549–553.

Bilitza, D., Truhlik, V., Richards, P., Abe, T., & Třísková, L. (2007). Solar cycle variation of mid-latitude electron density and temperature: Satellite measurements and model calculations. *Advances in Space Research*, *39*(5), 779–789. https://doi.org/10.1016/j.asr.2006.11.022

Bilitza, D., & Williamson, R. (2000). Toward a better representation of the IRI topside based on ISIS and Alouette data. *Advances in Space Research*, *25*(1), 149–152. https://doi.org/10.1016/S0273-1177(99)00912-6

Bilitza, D., & Xiong, C. (2021). A solar activity correction term for the IRI topside electron density model. *Advances in Space Research*, *68*(5), 2124–2137. https://doi.org/10.1016/j.asr.2020.11.012

Blanch, E., & Altadill, D. (2012). Midlatitude F region peak height changes in response to interplanetary magnetic field conditions and modeling results. *Journal of Geophysical Research*, *117*(A12), A12311. https://doi.org/10.1029/2012JA018009

Blanch, E., Arrazola, D., Altadill, D., Buresova, D., & Mosert, M. (2007). Improvement of IRI B0, B1 and D1 at mid-latitudes using MARP. *Advances in Space Research*, *39*(5), 701–710. https://doi.org/10.1016/j.asr.2006.08.007

Booker, H. G. (1977). Fitting of multi-region ionospheric profiles of electron-density by a single analytic-function of height. *Journal of Atmospheric and Terrestrial Physics*, *39*(5), 619–623. https://doi.org/10.1016/0021-9169(77)90072-1

Booker, H. G., & Wells, H. W. (1938). Scattering of radio waves by the F-region of the ionosphere. *Journal of Geophysical Research*, *43*(3), 249–256. https://doi.org/10.1029/TE043i003p00249

Brace, L. H., & Theis, R. F. (1978). An empirical model of the interrelationship of electron temperature and density in the daytime thermosphere at solar minimum. *Geophysical Research Letters*, *5*(4), 275–278. https://doi.org/10.1029/GL005i004p00275

Brace, L. H., & Theis, R. F. (1981). Global empirical models of ionospheric electron temperature in the upper F-region and plasmasphere based on in situ measurements from atmosphere explorer C, ISIS 1 and ISIS 2 satellites. *Journal of Atmospheric and Terrestrial Physics*, *43*(12), 1317–1343. https://doi.org/10.1016/0021-9169(81)90157-4

Bradley, P. A. (1993). Twilight and night-time representations of foE for the IRI. *Advances in Space Research*, *13*(3), 105–113. https://doi.org/10.1016/0273-1177(93)90259-E

Bradley, P. A. (1994). Improved representation of the night and twilight E-region critical frequency. *Advances in Space Research*, *14*(12), 71–74. https://doi.org/10.1016/0273-1177(94)90242-9

Brown, S., Bilitza, D., & Yiğit, E. (2018). Ionosonde-based indices for improved representation of solar cycle variation in the International Reference Ionosphere model. *Journal of Atmospheric and Solar-Terrestrial Physics*, *171*, 137–146. https://doi.org/10.1016/j.jastp.2017.08.022

Brum, C. G. M., Rodrigues, F. S., dos Santos, P. T., Matta, A. C., Aponte, N., Gonzalez, S. A., & Robles, E. (2011). A modeling study of foF2 and hmF2 parameters measured by the Arecibo incoherent scatter radar and comparison with IRI model predictions for solar cycles 21, 22, and 23. *Journal of Geophysical Research*, *116*(A3), A03324. https://doi.org/10.1029/2010JA015727

Brunini, C., Conte, J. F., Azpilicueta, F., & Bilitza, D. (2013). A different method to determine the height of the F2 peak. *Advances in Space Research*, *51*(12), 2322–2332. https://doi.org/10.1016/j.asr.2013.01.027

Buonsanto, M. J. (1989). Comparison of incoherent scatter observations of electron density, and electron and ion temperature at Millstone Hill with the International Reference Ionosphere. *Journal of Atmospheric and Terrestrial Physics*, *51*(5), 441–468. https://doi.org/10.1016/0021-9169(89)90125-6

Cabrera, M. A., Pezzopane, M., Zuccheretti, E., & Ezquer, R. G. (2010). Satellite traces, range spread-F occurrence, and gravity wave propagation at the southern anomaly crest. *Annales Geophysicae*, *28*(5), 1133–1140. https://doi.org/10.5194/angeo-28-1133-2010

Carpenter, D. L., & Anderson, R. R. (1992). An ISEE/whistler model of empirical electron density in the magnetosphere. *Journal of Geophysical Research*, *97*(A2), 1097–1108. https://doi.org/10.1029/91JA01548

CCIR. (1967). *Atlas of ionospheric characteristics, Report 340*. Consultative Committee on International Radio, International telecommunication Union.

CCIR. (1975). *Atlas of ionospheric characteristics, Report 340-2*. Consultative Committee on International Radio, International Telecommunications Union.

Chasovitin, Y. K., Gulyaeva, T. L., Deminov, M. G., & Ivanova, S. E. (1998). *Russian Standard Model of the Ionosphere (SMI), COST 251 Technical Document TD(98)005* (pp. 161–172). Rutherford Appleton Laboratory.

Chen, H., Liu, L., Wan, W., Ning, B., & Lei, J. (2006). A comparative study of the bottom side profile parameters over Wuhan with IRI-2001 for 1999–2004. *Earth Planets and Space*, *58*(5), 601–605. https://doi.org/10.1186/BF03351957

Chen, S.-P., Bilitza, D., Liu, J.-Y., Caton, R., Chang, L. C. W., & Yeh, W.-H. (2017). An empirical model of L-band scintillation S4 index constructed by using FORMOSAT- 3/COSMIC data. *Advances in Space Research*, *60*(5), 1015–1028. https://doi.org/10.1016/j.asr.2017.05.031

Chen, Y., Liu, L., & Wan, W. (2011). Does the $F_{10.7}$ index correctly describe solar EUV flux during the deep solar minimum of 2007–2009? *Journal of Geophysical Research*, *116*(A4), A04304. https://doi.org/10.1029/2010JA016301

Cherniak, I., & Zakharenkova, I. (2016). NeQuick and IRI-Plas model performance on topside electron content representation: Spaceborne GPS measurements. *Radio Science*, *51*(6), 752–766. https://doi.org/10.1002/2015RS005905

CIRA. (1972). *CIRA 1972: COSPAR international reference atmosphere 1972*. Akademie-Verlag.

Clette, F., Svalgaard, L., Vaquero, J. M., & Cliver, E. W. (2014). Revisiting the sunspot number, A 400-year perspective on the solar cycle. *Space Science Reviews*, *186*(1–4), 35–103. https://doi.org/10.1007/s11214-014-0074-2

Coïsson, P., Nava, B., & Radicella, S. M. (2009). On the use of NeQuick topside option in IRI-2007. *Advances in Space Research*, *43*(11), 1688–1693. https://doi.org/10.1016/j.asr.2008.10.035

Coïsson, P., Radicella, S. M., Leitinger, R., & Nava, B. (2006). Topside electron density in IRI and NeQuick: Features and limitations. *Advances in Space Research*, *37*(5), 937–942. https://doi.org/10.1016/j.asr.2005.09.015

Coley, W. R., Heelis, R. A., Hairston, M. R., Earle, G. D., Perdue, M. D., Power, R. A., et al. (2010). Ion temperature and density relationships measured by CINDI from the C/NOFS spacecraft during solar minimum. *Journal of Geophysical Research*, *115*(A2), A02313. https://doi.org/10.1029/2009JA014665

Daniell, R. E., Jr. (1993). Modeling of optical signatures of electron spectra in the ionospheric heating experiments. In *Proceedings of the 7th International Ionospheric Effects Symposium*. SRI International. 6B/5/1.

Danilov, A., & Yaichnikov, A. (1985). A new model of the ion composition at 75 km to 1000 km for IRI. *Advances in Space Research*, *5*(7), 75–79. https://doi.org/10.1016/0273-1177(85)90360-6

Danilov, A. D., Rodevich, A. Y., & Smirnova, N. V. (1991). Parametric model of the D region taking into account meteorological effects. *Geomagnetizm i Aeronomiya*, *31*(5), 881–885. (in Russian).

Danilov, A. D., Rodevich, A. Y., & Smirnova, N. V. (1995). Problems with incorporating a new D-region model into the IRI. *Advances in Space Research*, *15*(2), 165–168. https://doi.org/10.1016/S0273-1177(99)80042-8

Danilov, A. D., & Semenov, V. K. (1978). Relative ion composition model at midlatitudes. *Journal of Atmospheric and Terrestrial Physics*, *40*(10–11), 1093–1102. https://doi.org/10.1016/0021-9169(78)90057-0

Danilov, A. D., & Smirnova, N. V. (1994). Comparison of IRI with rocket measurements. *Advances in Space Research*, *14*(12), 125–134. https://doi.org/10.1016/0273-1177(94)90253-4

Danilov, A. D., & Smirnova, N. V. (1995). Improving the 75 km to 300 km ion composition model of the IRI. *Advances in Space Research*, *15*(2), 171–177. https://doi.org/10.1016/S0273-1177(99)80044-1

Da Rosa, A. (1966). The theoretical time-dependent thermal behavior of the ionospheric electron gas. *Journal of Geophysical Research*, *71*(17), 4107–4120. https://doi.org/10.1029/JZ071i017p04107

de La Beaujardière, O., & the C/NOFS Definition Team. (2004). C/NOFS: A mission to forecast scintillations. *Journal of Atmospheric and Solar-Terrestrial Physics*, *66*(17), 1573–1591. https://doi.org/10.1016/j.jastp.2004.07.030

Detman, T. R., & Vassiliadis, D. (1997). Review of techniques for magnetic storm forecasting. In B. T. Tsurutani, W. D. Gonzalez, Y. Kamide, & J. K. Arballo (Eds.), *Magnetic Storms*. *Geophysical Monograph Series* (Vol. 98, pp. 253–266). AGU. https://doi.org/10.1029/GM098p0253

Dubazane, M. B., & Habarulema, J. B. (2018). An empirical model of vertical plasma drift over the African sector. *Space Weather*, *16*(6), 619–635. https://doi.org/10.1029/2018SW001820

DuCharme, E. D., Petrie, L. E., & Eyfrig, R. (1971). A method for predicting the F_1 layer critical frequency. *Radio Science*, *6*(3), 369–378. https://doi.org/10.1029/RS008i010p00837

DuCharme, E. D., Petrie, L. E., & Eyfrig, R. (1973). A method for predicting the F_1 layer critical frequency based on the Zurich smoothed sunspot number. *Radio Science*, *8*(10), 837–839. https://doi.org/10.1029/RS008i010p00837

Dudeney, J. R. (1983). The accuracy of simple methods A simple empirical method for determine the height of the maximum electron concentration of the F2-layer from scaled ionospheric characteristics. *Journal of Atmospheric and Terrestrial Physics*, *45*(8/9), 629–640. https://doi.org/10.1016/S0021-9169(83)80080-4

Dyson, P. L., Davies, T. P., Parkinson, M. L., Reeves, A. J., Richards, P. G., & Fairchild, C. E. (1997). Thermospheric neutral winds at southern midlatitudes: A comparison of optical and ionosonde hmF2 methods. *Journal of Geophysical Research*, *102*(A12), 27189–27196. https://doi.org/10.1029/97JA02138

Emmert, J. T., Lean, J. L., & Picone, J. M. (2010). Record–low thermospheric density during the 2008 solar minimum. *Geophysical Research Letters*, *37*(12), L12102. https://doi.org/10.1029/2010GL043671

Ezquer, R. G., Jadur, C. A., & Mosert de Gonzalez, M. (1998). IRI-95 TEC predictions for the South American peak of the equatorial anomaly. *Advances in Space Research*, *22*(6), 811–814. https://doi.org/10.1016/S0273-1177(98)00103-3

Ezquer, R. G., López, J. L., Scidá, L. A., Cabrera, M. A., Zolesi, B., Bianchi, C., et al. (2014). Behavior of ionospheric magnitudes of F2 region over Tucumán during a deep solar minimum and comparison with the IRI2012 model predictions. *Journal of Atmospheric and Solar-Terrestrial Physics*, *107*, 89–98. https://doi.org/10.1016/j.jastp.2013.11.010

Fejer, B. G., de Paula, E. R., Heelis, R. A., & Hanson, W. B. (1995). Global equatorial ionospheric vertical plasma drifts measured by the AE-E satellite. *Journal of Geophysical Research*, *100*(A4), 5769–5776. https://doi.org/10.1029/94JA03240

Fejer, B. G., Jensen, J. W., & Su, S.-Y. (2008). Quiet time equatorial F region vertical plasma drift model derived from ROCSAT-1 observations. *Journal of Geophysical Research*, *113*(A5), A05304. https://doi.org/10.1029/2007JA012801

Fejer, B. G., & Maute, A. (2021). Equatorial ionospheric electrodynamics. In C. Huang, G. Lu, Y. Zhang, & L. J. Paxton (Eds.), *Ionosphere dynamics and applications* (pp. 159–183). chapter 9. https://doi.org/10.1002/9781119815617

Feldstein, Y. I., & Starkov, G. V. (1967). Dynamics of auroral belt and polar geomagnetic disturbances. *Planetary and Space Science*, *15*(2), 209–229. https://doi.org/10.1016/0032-0633(67)90190-0

Ferguson, B. G., & McNamara, L. F. (1986). Calculation of HF absorption using the international reference Ionosphere. *Journal of Atmospheric and Terrestrial Physics*, *48*(1), 41–49. https://doi.org/10.1016/0021-9169(86)90111-X

Fox, M. W., & McNamara, L. F. (1988). Improved world-wide maps of monthly median foF2. *Journal of Atmospheric and Terrestrial Physics*, *50*(12), 1077–1086. https://doi.org/10.1016/0021-9169(88)90096-7

Fridman, S. V., Nickisch, L. J., Aiello, M., & Hausman, M. (2006). Realtime reconstruction of the three dimensional ionosphere using data from a network of GPS receivers. *Radio Science*, *41*(5), RS5S12. https://doi.org/10.1029/2005RS003341

Friedrich, M., Pock, C., & Torkar, K. (2018). FIRI-2018, an updated empirical model of the lower ionosphere. *Journal of Geophysical Research: Space Physics*, *123*(8), 6737–6751. https://doi.org/10.1029/2018JA025437

Friedrich, M., & Torkar, K. (2001). FIRI: A semiempirical model of the lower ionosphere. *Journal of Geophysical Research*, *106*(A10), 21409–21418. https://doi.org/10.1029/2001JA900070

Froń, A., Galkin, I., Krankowski, A., Bilitza, D., Hernández-Pajares, M., Reinisch, B., et al. (2020). Towards cooperative global mapping of the ionosphere: Fusion feasibility for IGS and IRI with global climate VTEC maps. *Remote Sensing*, *12*(21), 3531. https://doi.org/10.3390/rs12213531

Fuller-Rowell, T. J., Araujo-Pradere, E., & Codrescu, M. V. (2000). An empirical ionospheric storm-time correction model. *Advances in Space Research*, *25*(1), 139–146. https://doi.org/10.1016/S0273-1177(99)00911-4

Fuller-Rowell, T. J., & Evans, D. S. (1987). Height-integrated Pedersen and Hall conductivity patterns inferred from the TIROS-NOAA satellite data. *Journal of Geophysical Research*, *92*(A7), 7606–7618. https://doi.org/10.1029/JA092iA07p07606

Galkin, I., Froń, A., Reinisch, B., Hernández-Pajares, M., Krankowski, A., Nava, B., et al. (2022). Global monitoring of ionospheric weather by GIRO and GNSS data fusion. *Atmosphere*, *13*(3), 371. https://doi.org/10.3390/atmos13030371

Galkin, I. A., Reinisch, B. W., & Bilitza, D. (2018). Realistic ionosphere: Real-time ionosonde service for ISWI. *Sun & Geosphere*, *13*(2), 173–178. https://doi.org/10.31401/SunGeo.2018.02.09

Galkin, I. A., Reinisch, B. W., Huang, X., & Bilitza, D. (2012). Assimilation of GIRO data into a real-time IRI. *Radio Science*, *47*(4), RS0L07. https://doi.org/10.1029/2011RS004952

Galkin, I. A., Reinisch, B. W., Vesnin, A. M., Bilitza, D., Fridman, S., Habarulema, J. B., & Veliz, O. (2020). Assimilation of sparse continuous near-Earth weather measurements by NECTAR model morphing. *Space Weather*, *18*(11), e2020SW002463. https://doi.org/10.1029/2020SW002463

Gallagher, D. L., Craven, P. D., & Comfort, R. H. (2000). Global core plasma model. *Journal of Geophysical Research*, *105*(A8), 18819–18833. https://doi.org/10.1029/1999JA000241

Gulyaeva, T. L. (1987). Progress in ionospheric informatics based on electron density profile analysis of ionograms. *Advances in Space Research*, *7*(6), 39–48. https://doi.org/10.1016/0273-1177(87)90269-9

Gulyaeva, T. L. (2012). Empirical model of ionospheric storm effects on the F2 layer peak height associated with changes of peak electron density. *Journal of Geophysical Research*, *117*(A2), A02302. https://doi.org/10.1029/2011JA017158

Gulyaeva, T. L. (2016). Modification of solar activity indices in the International Reference Ionosphere IRI and IRI-Plas models due to recent revision of sunspot number time series. *Solar-Terrestrial Physics*, *2*(3), 59–66. https://doi.org/10.12737/20872

Gulyaeva, T. L., Bradley, P. A., Stanislawska, I., & Juchnikowski, G. (2008). Towards a new reference model of hmF2 for IRI. *Advances in Space Research*, *42*(4), 666–672. https://doi.org/10.1016/j.asr.2008.02.021

Gulyaeva, T. L., Huang, X., & Reinisch, B. W. (2002). The ionosphere-plasmasphere model software for ISO. *Acta Geodaetica et Geophysica Hungarica*, *37*(2–3), 143–152. https://doi.org/10.1556/ageod.37.2002.2-3.3

Gulyaeva, T. L., & Titheridge, J. E. (2006). Advanced specification of electron density and temperature in the IRI ionosphere-plasmasphere model. *Advances in Space Research*, *38*(11), 2587–2595. https://doi.org/10.1016/j.asr.2005.08.045

Gulyaeva, T. L., Titheridge, J. E., & Rawer, K. (1990). Discussion of the valley problem in N(h) analysis of ionograms. *Advances in Space Research*, *10*(8), 123–126. https://doi.org/10.1016/0273-1177(90)90198-9

Habarulema, J. B., & Ssessanga, N. (2016). Adapting a climatology model to improve estimation of ionosphere parameters and subsequent validation with radio occultation and ionosonde data. *Space Weather*, *15*(1), 84–98. https://doi.org/10.1002/2016SW001549

Hardy, D. A., Gussenhoven, M. S., Raistrick, R., & McNeil, W. J. (1987). Statistical and functional representation of the pattern of auroral energy flux, number flux, and conductivity. *Journal of Geophysical Research*, *92*(A11), 12275–12294. https://doi.org/10.1029/JA092iA11p12275

Hedin, A. E. (1987). MSIS-86 thermospheric model. *Journal of Geophysical Research*, *92*(A5), 4649–4662. https://doi.org/10.1029/JA092iA05p04649

Hedin, A. E. (1991). Extension of the MSIS thermosphere model into the middle and lower atmosphere. *Journal of Geophysical Research*, *96*(A2), 1159–1172. https://doi.org/10.1029/90JA02125

Heelis, R. A., Coley, W. R., Burrell, A. G., Hairston, M. R., Earle, G. D., Perdue, M. D., et al. (2009). Behavior of the O+/H+ transition height during the extreme solar minimum of 2008. *Geophysical Research Letters*, *36*(18), L00C03. https://doi.org/10.1029/2009GL038652

Hernandez-Pajares, M., Juan, J., Sanz, J., & Bilitza, D. (2002). Combining GPS measurements and IRI model values for space weather specification. *Advances in Space Research*, *29*(6), 949–958. https://doi.org/10.1016/S0273-1177(02)00051-0

Holzworth, R. H., & Meng, C. I. (1975). Mathematical representation of the auroral oval. *Geophysical Research Letters*, *2*(9), 337–380. https://doi.org/10.1029/GL002i009p00377

Hoque, M. M., & Jakowski, N. (2012). A new global model for the ionospheric F2 peak height for radio wave propagation. *Annales Geophysicae*, *30*(5), 797–809. https://doi.org/10.5194/angeo-30-797-2012

Huang, H., Moses, M., Volk, A. E., Elezz, O. A., Kassamba, A. A., & Bilitza, D. (2021). Assessment of IRI-2016 hmF2 model options with digisonde, COSMIC observations for low and high solar flux conditions during 23rd solar cycle. *Advances in Space Research*, *68*(5), 2093–2103. https://doi.org/10.1016/j.asr.2021.01.033

Huang, X., & Reinisch, B. W. (1996). Vertical electron density profiles from digisonde ionograms. The average representative profile. *Annals of Geophysics*, *39*(4), 751–756. https://doi.org/10.4401/ag-4010

Immel, T. J., Sagawa, E., England, S. L., Henderson, S. B., Hagan, M. E., Mende, S. B., et al. (2006). Control of equatorial ionospheric morphology by atmospheric tides. *Geophysical Research Letters*, *33*(15), L15108. https://doi.org/10.1029/2006GL026161

ISO 16457. (2022). *Space systems – Space Environment (natural and artificial) – The Earth's ionosphere model: International reference ionosphere (IRI) model and extension to the plasmasphere*. International Standardization Organization. Retrieved from http://www.iso.org/iso/home/store/catalogue_tc/catalogue_detail.htm?csnumber=61556

Iwamoto, I., Katoh, H., Maruyama, T., Minakoshi, H., Watari, S., & Igarashi, K. (2002). Latitudinal variations of solar flux dependence in the topside plasma density: Comparison between IRI model and observations. *Advances in Space Research*, *29*(6), 877–882. https://doi.org/10.1016/S0273-1177(02)00054-6

Jakowski, N., & Hoque, M. M. (2018). A new electron density model of the plasmasphere for operational applications and services. *Journal of Space Weather and Space Climate*, *8*, A16. https://doi.org/10.1051/swsc/2018002

Jones, W. B., & Gallet, R. M. (1962). Representation of diurnal and geographical variations of ionospheric data by numerical methods. *Journal of Research of the National Bureau of Standards, Section D: Radio Propagation*, *66*(4), 129–147. https://doi.org/10.6028/jres.066D.043

Jones, W. B., & Gallet, R. M. (1965). Representation of diurnal and geographic variations of ionospheric data by numerical methods, II. Control of instability. *ITU Telecommunication Journal*, *32*(1), 18–28.

Jones, W. B., Graham, R. P., & Leftin, M. (1969). *Advances in ionospheric mapping by numerical methods*. *ESSA Technical Report ERL 107-ITS75*. U.S. Department of Commerce.

Kauristie, K., Morschhauser, A., Olsen, N., Finlay, C. C., McPherron, R. L., Gjerloev, J. W., & Opgenoorth, H. J. (2017). On the usage of geomagnetic indices for data selection in internal field modelling. *Space Science Reviews*, *206*(1–4), 61–90. https://doi.org/10.1007/s11214-016-0301-0

Kelley, M. C. (2009). *The Earth's ionosphere*. *International Geophysics Book Series* (2nd ed.), (Vol. 96). Academic Press.

Kimura, I., Hikuma, A., Kasahara, Y., & Oya, H. (1996). Electron density distribution in the plasmasphere in conjunction with IRI model, deduced from Akebono wave data. *Advances in Space Research*, *18*(6), 279–288. https://doi.org/10.1016/0273-1177(95)00937-X

King, J. H., & Papitashvili, N. E. (2005). Solar wind spatial scales in and comparisons of hourly Wind and ACE plasma and magnetic field data. *Journal of Geophysical Research*, *110*(A2), A02104. https://doi.org/10.1029/2004JA010649

King, J. W. (1973). The determination of foF2 and hmF2 from satellite-borne probe data. *Telecommunication Journal*, *40*, 364–368.

Kitanidis, P. K. (1997). *Introduction to geostatistics: Application to hydrogeology* (p. 272). Cambridge University Press.
Klenzing, J., Simões, F., Ivanov, S., Bilitza, D., Heelis, R. A., & Rowland, D. (2013). Performance of the IRI-2007 model for equatorial topside ion density in the African sector for low and extremely low solar activity. *Advances in Space Research*, *52*(10), 1780–1790. https://doi.org/10.1016/j.asr.2012.09.030
Klenzing, J., Simões, F., Ivanov, S., Heelis, R. A., Bilitza, D., Pfaff, R., & Rowland, D. (2011). Topside equatorial ionospheric density and composition during and after extreme solar minimum. *Journal of Geophysical Research*, *116*(A12), A12330. https://doi.org/10.1029/2011JA017213
Klinngam, S., Supnithi, P., Rungraengwajiake, S., Tsugawa, T., Ishii, M., & Maruyama, T. (2015). The occurrence of equatorial spread-F at conjugate stations in Southeast Asia. *Advances in Space Research*, *55*(8), 2139–2147. https://doi.org/10.1016/j.asr.2014.10.003
Komjathy, A., Langley, R., & Bilitza, D. (1998). Ingesting GPS-derived TEC data into the International Reference Ionosphere for single frequency radar altimeter ionospheric delay corrections. *Advances in Space Research*, *22*(6), 793–801. https://doi.org/10.1016/S0273-1177(98)00100-8
Kotov, D. V., Truhlik, V., Richards, P. G., Stankov, S., Bogomaz, O. V., Chernogor, L. F., & Domnin, I. F. (2015). Night-time light ion transition height behaviour over the Kharkiv (50°N, 36°E) IS radar during the equinoxes of 2006–2010. *Journal of Atmospheric and Solar-Terrestrial Physics*, *132*, 1–12. https://doi.org/10.1016/j.jastp.2015.06.004
Kouris, S. S., & Muggleton, L. M. (1973). A proposed prediction method for monthly median foE, contribution No. 6/03/07 to Interim Working Party 6/3. *CCIR Report 252-2*.
Lee, C.-C., & Reinisch, B. W. (2006). Quiet-condition hmF2, NmF2, and B0 variations at Jicamarca and comparison with IRI-2001 during solar maximum. *Journal of Atmospheric and Solar-Terrestrial Physics*, *68*(18), 2138–2146. https://doi.org/10.1016/j.jastp.2006.07.007
Lee, C.-C., Reinisch, B. W., Su, S.-Y., & Chen, W. S. (2008). Quiet-time variation of F2-layer parameters at Jicamarca and comparison with IRI-2001 during solar minimum. *Journal of Atmospheric and Solar-Terrestrial Physics*, *70*(1), 184–192. https://doi.org/10.1016/j.jastp.2007.10.008
Leftin, M., Ostrow, S. M., & Preston, C. (1968). *Numerical maps of foEs for solar cycle minimum and maximum*. *ESSA Technical Report ERL 73-ITS 63*. US Government Printing Office.
Lei, J., Liu, L., Wan, W., Zhang, S. R., & Holt, J. M. (2004). A statistical study of ionospheric profile parameters derived from Millstone Hill incoherent scatter radar measurements. *Geophysical Research Letters*, *31*(14), L14804. https://doi.org/10.1029/2004GL020578
Leitinger, R., Nava, B., Hochegger, G., & Radicella, S. (2001). Ionospheric profilers using data grids. *Physics and Chemistry of the Earth - Part C: Solar, Terrestrial & Planetary Science*, *26*(5), 293–301. https://doi.org/10.1016/S1464-1917(01)00002-2
Li, G., Ning, B., Otsuka, Y., Abdu, M. A., Abadi, P., Liu, Z., et al. (2021). Challenges to equatorial plasma bubble and ionospheric scintillation short-term forecasting and future aspects in East and Southeast Asia. *Surveys in Geophysics*, *42*(1), 201–238. https://doi.org/10.1007/s10712-020-09613-5
Liu, J. Y., Chen, V. I., & Lin, J. S. (2003). Statistical investigation of the saturation effect in the ionospheric foF2 versus sunspot, solar radio noise, and solar EUV radiation. *Journal of Geophysical Research*, *108*(A2), 1067. https://doi.org/10.1029/2001ja007543
Liu, R., Smith, P., & King, J. (1983). A new solar index which leads to improved foF2 predictions using the CCIR atlas. *Telecommunication Journal*, *50*(8), 408–414.
Lühr, H., Alken, P., & Zhou, Y.-L. (2021). The equatorial electrojet. In C. Huang, G. Lu, Y. Zhang, & L. J. Paxton (Eds.), *Ionosphere Dynamics and Applications* (pp. 281–299). chapter 12. https://doi.org/10.1002/9781119815617
Lühr, H., Häusler, K., & Stolle, C. (2007). Longitudinal variation of F region electron density and thermospheric zonal wind caused by atmospheric tides. *Geophysical Research Letters*, *34*(16), L16102. https://doi.org/10.1029/2007GL030639
Lühr, H., & Xiong, C. (2010). The IRI 2007 model overestimates electron density during the 23/24 solar minimum. *Geophysical Research Letters*, *37*(23), L23101. https://doi.org/10.1029/2010GL045430
Ma, R., Xu, J., Wang, W., & Yuan, W. (2009). Seasonal and latitudinal differences of the saturation effect between ionospheric NmF2 and solar activity indices. *Journal of Geophysical Research*, *114*(A10), A10303. https://doi.org/10.1029/2009JA014353
Maeda, K.-I. (1969). Mid-latitude electron density profile as revealed by rocket experiments. *Journal of Geomagnetism and Geoelectricity*, *21*(2), 557–567. https://doi.org/10.5636/jgg.21.557
Maeda, K.-I. (1971). Study on electron density profile in the lower ionosphere. *Journal of Geomagnetism and Geoelectricity*, *23*(2), 133–159. https://doi.org/10.5636/jgg.23.133
Magdaleno, S., Altadill, D., Herraiz, M., Blanch, E., & de la Morena, B. (2011). Ionospheric peak height behavior for low middle and high latitudes: A potential empirical model for quiet conditions. Comparison with the IRI-2007 model. *Journal of Atmospheric and Solar-Terrestrial Physics*, *73*(13), 1810–1817. https://doi.org/10.1016/j.jastp.2011.04.019
Mahajan, K. K., Kohli, R., Pandey, V. K., & Sethi, N. K. (1990). Information about the E-region valley from incoherent scatter measurements. *Advances in Space Research*, *10*(8), 17–20. https://doi.org/10.1016/0273-1177(90)90179-4
Marew, H., Nigussie, M., Hui, D., & Damitie, B. (2019). A method of estimating equatorial plasma vertical drift velocity and its evaluation using C/NOFS observations. *Radio Science*, *54*, 590–601. https://doi.org/10.1029/2019RS006800
Matuura, N., Kotaki, M., Miyazaki, S., Sagawa, E., & Iwamoto, I. (1981). ISS—B experimental results on global distribution of ionospheric parameters and thunderstorm activity. *Acta Astronautica*, *8*(5–6), 527–548. https://doi.org/10.1016/0094-5765(81)90104-1
McKinnell, L. A., & Friedrich, M. (2007). A neural network-based ionospheric model for the auroral zone. *Journal of Atmospheric and Solar-Terrestrial Physics*, *69*(12), 1459–1470. https://doi.org/10.1016/j.jastp.2007.05.003
McKinnell, L. A., Friedrich, M., & Steiner, R. J. (2004). A new approach to modeling the daytime lower ionosphere at auroral latitudes. *Advances in Space Research*, *34*(9), 1943–1948. https://doi.org/10.1016/j.asr.2004.05.005
McNamara, L. F., Retterer, J. M., Baker, C. R., Bishop, G. J., Cooke, D. L., Roth, C. J., & Welsh, J. A. (2010). Longitudinal structure in the CHAMP electron densities and their implications for global ionospheric modeling. *Radio Science*, *45*(2), RS2001. https://doi.org/10.1029/2009RS004251
Mechtley, E. A., & Bilitza, D. (1974). *Models of D-region electron concentrations*. Institut fuer Physikalische Weltraumforschung, Report IPW-WB1, Freiburg, Federal Republic of Germany.
Mechtley, E. A., Bowhill, S. A., & Smith, L. G. (1972). Changes of lower ionosphere electron concentrations with solar activity. *Journal of Atmospheric and Terrestrial Physics*, *34*(11), 1899–1907. https://doi.org/10.1016/0021-9169(72)90065-7
Mendillo, M. (2006). Storms in the ionosphere: Patterns and processes for total electron content. *Reviews of Geophysics*, *44*(4), RG4001. https://doi.org/10.1029/2005RG000193
Mengist, C. K., Yadav, S., Kotulak, K., Bahar, A., Zhang, S.-R., & Seo, K.-H. (2020). Validation of International Reference Ionosphere model (IRI-2016) for F-region peak electron density height (hmF2): Comparison with incoherent scatter radar (ISR) and ionosonde measurements at Millstone Hill. *Advances in Space Research*, *65*(12), 2773–2781. https://doi.org/10.1016/j.asr.2020.03.017
Menvielle, M., & Berthelier, A. (1991). The K-derived planetary indices: Description and availability. *Reviews of Geophysics*, *3*(29), 415–432. https://doi.org/10.1029/91RG00994

Mertens, C. J., Xu, X., Bilitza, D., Mlynczak, M. G., & Russell, III, J. M. (2013a). Empirical STORM-E model: I. Theoretical and observational basis. *Advances in Space Research*, *51*(4), 554–574. https://doi.org/10.1016/j.asr.2012.09.009

Mertens, C. J., Xu, X., Bilitza, D., Mlynczak, M. G., & Russell, III, J. M. (2013b). Empirical STORM-E model: II. Geomagnetic corrections to nighttime ionospheric E-region electron densities. *Advances in Space Research*, *51*(4), 575–598. https://doi.org/10.1016/j.asr.2012.09.009

Migoya-Orué, Y. O., Nava, B., Radicella, S., & Alazo-Cuartas, K. (2015). GNSS derived TEC data ingestion into IRI 2012. *Advances in Space Research*, *55*(8), 1994–2002. https://doi.org/10.1016/j.asr.2014.12.033

Migoya-Orué, Y. O., Radicella, S. M., & Nava, B. (2013). Comparison of topside electron density computed by ionospheric models and plasma density observed by DMSP satellites. *Advances in Space Research*, *52*(10), 1710–1716. https://doi.org/10.1016/j.asr.2013.01.032

Miller, K. L., Torr, D. G., & Richards, P. G. (1986). Meridional winds in the thermosphere derived from measurement of F2 layer height. *Journal of Geophysical Research*, *91*(A4), 4531–4535. https://doi.org/10.1029/JA091iA04p04531

Mosert de Gonzales, M., & Radicella, S. M. (1990). On a characteristic point at the base of F2 layer in the ionosphere. *Advances in Space Research*, *10*(11), 17–25. https://doi.org/10.1016/0273-1177(90)90300-O

Moses, M., Bilitza, D., Kumar Panda, S., & Ochonugor, B. J. (2021). Assessment of IRI-2016 hmF2 model predictions with COSMIC observations over the African region. *Advances in Space Research*, *68*(5), 2115–2123. https://doi.org/10.1016/j.asr.2020.10.029

Muggleton, L. M. (1975). A method of predicting foE at any time and place. *Telecommunication Journal*, *42*, 413–418.

Nava, B., Coïsson, P., & Radicella, S. M. (2008). A new version of the NeQuick ionosphere electron density model. *Journal of Atmospheric and Solar-Terrestrial Physics*, *70*(15), 1856–1862. https://doi.org/10.1016/j.jastp.2008.01.015

Nicolls, M. J., Rodrigues, F. S., & Bust, G. S. (2012). Global observations of E region plasma density morphology and variability. *Journal of Geophysical Research*, *117*(A1), A01305. https://doi.org/10.1029/2011JA017069

Nsumei, P. A., Huang, X., Reinisch, B. W., Song, P., Vasyliunas, V. M., Green, J. L., et al. (2003). Electron density distribution over the northern polar region deduced from IMAGE/RPI sounding. *Journal of Geophysical Research*, *108*(A2). https://doi.org/10.1029/2002JA009616

Oliver, M. A., & Webster, R. (1990). Kriging: A method of interpolation for geographical information systems. *International Journal of Geographical Information Systems*, *4*(3), 313–332. https://doi.org/10.1080/02693799008941549

Ossakow, S. L. (1981). Spread-F theories—A review. *Journal of Atmospheric and Terrestrial Physics*, *43*(5–6), 437–452. https://doi.org/10.1016/0021-9169(81)90107-0

Oyama, K. I., Balan, N., Watanabe, S., Takahashi, T., Isoda, F., Bailey, G. J., & Oya, H. (1996). Morning overshoot of T-e enhanced by downward plasma drift in the equatorial topside ionosphere. *Journal of Geomagnetism and Geoelectricity*, *48*(7), 959–966. https://doi.org/10.5636/jgg.48.959

Oyeyemi, E. O., Adewale, A. O., Adeloye, A. B., & Olugbon, B. (2013). An evaluation of the IRI-2007 storm time model at low latitude stations. *Advances in Space Research*, *52*(10), 1737–1747. https://doi.org/10.1016/j.asr.2013.04.027

Oyeyemi, E. O., McKinnell, L. A., & Poole, A. W. V. (2007). Neural network-based prediction techniques for global modeling of M(3000)F2 ionospheric parameter. *Advances in Space Research*, *39*(5), 643–650. https://doi.org/10.1016/j.asr.2006.09.038

Ozhogin, P., Tu, J., Song, P., & Reinisch, B. W. (2012). Field-aligned distribution of the plasmaspheric electron density: An empirical model derived from the IMAGE RPI measurements. *Journal of Geophysical Research*, *117*(A6). https://doi.org/10.1029/2011JA017330

Paxton, L. J., Morrison, D., Zhang, Y., Kil, H., Wolven, B., Ogorzalek, B. S., et al. (2002). Validation of remote sensing products produced by the special sensor ultraviolet scanning imager (SSUSI): A far-UV imaging spectrograph on DMSP F16. In A. M. Larar & M. G. Mlynczak (Eds.), *SPIE Optical Spectroscopic Techniques and Instrumentation for Atmospheric and Space Research IV* (Vol. *4485*, pp. 338–348).

Perna, L., & Pezzopane, M. (2016). foF2 vs solar indices for the Rome station: Looking for the best general relation which is able to describe the anomalous minimum between cycles 23 and 24. *Journal of Atmospheric and Solar-Terrestrial Physics*, *148*, 13–21. https://doi.org/10.1016/j.jastp.2016.08.003

Perna, L., Pezzopane, M., Ezquer, R., Cabrera, M., & Baskaradas, J. A. (2017). NmF2 trends at low and mid latitudes for the recent solar minima and comparison with IRI-2012 model. *Advances in Space Research*, *60*(2), 363–374. https://doi.org/10.1016/j.asr.2016.09.025

Pezzopane, M., Pietrella, M., Pignatelli, A., Zolesi, B., & Cander, L. R. (2011). Assimilation of autoscaled data and regional and local ionospheric models as input sources for real-time 3-D International Reference Ionosphere modeling. *Radio Science*, *46*(5), RS5009. https://doi.org/10.1029/2011RS004697

Pezzopane, M., Pietrella, M., Pignatelli, A., Zolesi, B., & Cander, L. R. (2013). Testing the three-dimensional IRI-SIRMUP-P mapping of the ionosphere for disturbed periods. *Advances in Space Research*, *52*(10), 1726–1736. https://doi.org/10.1016/j.asr.2012.11.028

Pezzopane, M., & Pignalberi, A. (2019). The ESA Swarm mission to help ionospheric modeling: A new NeQuick topside formulation for mid-latitude regions. *Scientific Reports*, *9*(1), 12253. https://doi.org/10.1038/s41598-019-48440-6

Pezzopane, M., Zuccheretti, E., Abadi, P., de Abreu, A. J., de Jesus, R., Fagundes, P. R., et al. (2013). Low-latitude equinoctial spread-F occurrence at different longitude sectors under low solar activity. *Annales Geophysicae*, *31*(2), 153–162. https://doi.org/10.5194/angeo-31-153-2013

Picone, J. M., Hedin, A. E., Drob, D. P., & Aikin, A. C. (2002). NRLMSISE-00 empirical model of the atmosphere: Statistical comparisons and scientific issues. *Journal of Geophysical Research*, *107*(A12). SIA 15-1–SIA 15-16. https://doi.org/10.1029/2002JA009430

Pierrard, V., & Voiculescu, M. (2011). The 3D model of the plasmasphere coupled to the ionosphere. *Geophysical Research Letters*, *38*(12), L12104. https://doi.org/10.1029/2011GL047767

Pietrella, M., Pezzopane, M., Fagundes, P. R., de Jesus, R., Supnithi, P., Klinnagm, S., et al. (2017). Equinoctial spread-F occurrence at low latitudes in different longitude sectors under moderate and high solar activity. *Journal of Atmospheric and Solar-Terrestrial Physics*, *164*, 149–162. https://doi.org/10.1016/j.jastp.2017.07.007

Pietrella, M., Pignalberi, A., Pezzopane, M., Azzarone, A., & Rizzi, R. (2018). A comparative study of ionospheric IRIEup and ISP assimilative models during some intense and severe geomagnetic storms. *Advances in Space Research*, *61*(10), 2569–2584. https://doi.org/10.1016/j.asr.2018.02.026

Pignalberi, A., Aksonova, K. D., Zhang, S. R., Truhlik, V., Gurram, P., & Pavlou, C. (2021). Climatological study of the ion temperature in the ionosphere as recorded by Millstone Hill incoherent scatter radar and comparison with the IRI model. *Advances in Space Research*, *68*(5), 2186–2203. https://doi.org/10.1016/j.asr.2020.10.025

Pignalberi, A., Giannattasio, F., Truhlik, V., Coco, I., Pezzopane, M., Consolini, G., et al. (2021). On the electron temperature in the topside ionosphere as seen by Swarm satellites, incoherent scatter radars, and the International reference Ionosphere model. *Remote Sensing*, *13*(20), 4077. https://doi.org/10.3390/rs13204077

Pignalberi, A., Habarulema, J. B., Pezzopane, M., & Rizzi, R. (2019). On the development of a method for updating an empirical climatological ionospheric model by means of assimilated vTEC measurements from a GNSS receiver network. *Space Weather*, *17*(7), 1131–1164. https://doi.org/10.1029/2019SW002185

Pignalberi, A., Pezzopane, M., & Nava, B. (2022). Optimizing the NeQuick topside scale height parameters through COSMIC/FORMOSAT-3 radio occultation data. *IEEE Geoscience and Remote Sensing Letters*, *19*, 1–5. https://doi.org/10.1109/LGRS.2021.3096657

Pignalberi, A., Pezzopane, M., Rizzi, R., & Galkin, I. (2018a). Correction to: Effective solar indices for ionospheric modeling: A review and a proposal for a real-time regional IRI. *Surveys in Geophysics*, *39*(1), 169. https://doi.org/10.1007/s10712-017-9453-z

Pignalberi, A., Pezzopane, M., Rizzi, R., & Galkin, I. (2018b). Effective solar indices for ionospheric modeling: A review and a proposal for a real-time regional IRI. *Surveys in Geophysics*, *39*(1), 125–167. https://doi.org/10.1007/s10712-017-9438-y

Pignalberi, A., Pezzopane, M., Themens, D. R., Haralambous, H., Nava, B., & Coïsson, P. (2020). On the analytical description of the topside ionosphere by NeQuick: Modeling the scale height through COSMIC/FORMOSAT-3 selected data. *IEEE Journal of Selected Topics in Applied Earth Observations and Remote Sensing*, *13*, 1867–1878. https://doi.org/10.1109/JSTARS.2020.2986683

Pignalberi, A., Pezzopane, M., Tozzi, R., De Michelis, P., & Coco, I. (2016). Comparison between IRI and preliminary Swarm Langmuir probe measurements during the St. Patrick storm period. *Earth Planets and Space*, *68*(1), 93. https://doi.org/10.1186/s40623-016-0466-5

Pignalberi, A., Pietrella, M., & Pezzopane, M. (2021). Towards a real-time description of the ionosphere: A comparison between International Reference Ionosphere (IRI) and IRI real-time assimilative mapping (IRTAM) models. *Atmosphere*, *12*(8), 1003. https://doi.org/10.3390/atmos12081003

Priyadarshi, S. (2015). A review of ionospheric scintillation models. *Surveys in Geophysics*, *36*(2), 295–324. https://doi.org/10.1007/s10712-015-9319-1

Prölss, G. (2004). *Physics of the Earth's space environment: An introduction*. Springer-Verlag Berlin Heidelberg.

Radicella, S. M., & Leitinger, R. (2001). The evolution of the DGR approach to model electron density profiles. *Advances in Space Research*, *27*(1), 35–40. https://doi.org/10.1016/S0273-1177(00)00138-1

Ramakrishnan, S., & Rawer, K. (1972). Model electron density profiles obtained by empirical procedures. In S. A. Bowhill, J. D. Jaffe, & M. J. Rycroft (Eds.), *Space Research XII* (pp. 1253–1259). Akademie.

Rana, G., Bardhan, A., Sharma, D. K., Yadav, M. K., Aggarwal, M., Dudeja, J., et al. (2019). Variations of ion density and temperature as measured by ROCSAT-1 satellite over the Indian Region and comparison with IRI-2016 model. *Annales Geophysicae*, *62*(6), PA677. https://doi.org/10.4401/ag-8131

Ratcliffe, J. A. (1972). *An introduction to the ionosphere and magnetosphere*. Cambridge University Press.

Rawer, K. (1963). Propagation of decameter waves (HF band). In B. Landmark (Ed.), *Meteorological and astronomical influences on radio wave propagation* (pp. 221–250). Academic Press.

Rawer, K. (1984). Modelling of neutral and ionized atmospheres. In *Encyclopedia of physics, XLIX/7* (pp. 223–533). Springer.

Rawer, K., & Bilitza, D. (1989). Electron density profile description in the international reference ionosphere. *Journal of Atmospheric and Terrestrial Physics*, *51*(9–10), 781–790. https://doi.org/10.1016/0021-9169(89)90035-4

Rawer, K., & Bilitza, D. (1990). International reference ionosphere-plasma densities: Status 1988. *Advances in Space Research*, *10*(8), 5–14. https://doi.org/10.1016/0273-1177(90)90177-2

Rawer, K., Bilitza, D., & Ramakrishnan, S. (1978). *International reference ionosphere 78. Special Report*. International Union of Radio Science (URSI).

Rawer, K., Bilitza, D., Ramakrishnan, S., & Sheikh, N. (1978). Intentions and build-up of the International reference Ionosphere. In *Operational modelling of the aerospace propagation environment*. *AGARD Conference Proceedings No. 238* (pp. 6-1–6-9).

Rawer, K., Lincoln, J. V., & Conkright, R. O. (1981). International reference ionosphere—IRI 79. *World Data Center A for Solar-Terrestrial Physics, Report UAG-82*. Retrieved from https://repository.library.noaa.gov/view/noaa/1319

Rawer, K., Ramakrishnan, S., & Bilitza, D. (1975). *Preliminary reference profiles for electron and ion densities and temperatures proposed for the International Reference Ionosphere. Scientific Report W.B. 2*. Institut für physikalische Weltraumforschung.

Reddybattula, K. D., & Panda, S. K. (2019). Performance analysis of quiet and disturbed time ionospheric TEC responses from GPS-based observations, IGS-GIM, IRI-2016 and SPIM/IRI-Plas 2017 models over the low latitude Indian region. *Advances in Space Research*, *64*(10), 2026–2045. https://doi.org/10.1016/j.asr.2019.03.034

Reinisch, B. W., & Galkin, I. A. (2011). Global ionospheric radio observatory (GIRO). *Earth Planets and Space*, *63*(4), 377–381. https://doi.org/10.5047/eps.2011.03.001

Reinisch, B. W., Galkin, I. A., Khmyrov, G. M., Kozlov, A. V., Bibl, K., Lisysyan, I. A., et al. (2009). The new digisonde for research and monitoring applications. *Radio Science*, *44*(1), RS0A24. https://doi.org/10.1029/2008RS004115

Reinisch, B. W., & Huang, X. (1983). Automatic calculation of electron density profiles from digital ionograms. Processing of bottomside ionograms. *Radio Science*, *18*(3), 477–492. https://doi.org/10.1029/RS018i003p00477

Reinisch, B. W., & Huang, X. (1996). Low latitude digisonde measurements and comparison with IRI. *Advances in Space Research*, *18*(6), 5–12. https://doi.org/10.1016/0273-1177(95)00892-6

Reinisch, B. W., & Huang, X. (1998). Finding better B0 and B1 parameters for the IRI F2-profile function. *Advances in Space Research*, *22*(6), 741–747. https://doi.org/10.1016/S0273-1177(98)00092-1

Reinisch, B. W., & Huang, X. (2000). Redefining the F1 layer profile. *Advances in Space Research*, *25*(1), 81–88. https://doi.org/10.1016/S0273-1177(99)00901-1

Reinisch, B. W., Huang, X., Song, P., Sales, G. S., Fung, S. F., Green, J. L., et al. (2001). Plasma density distribution along the magnetospheric field: RPI observations from IMAGE. *Geophysical Research Letters*, *28*(24), 4521–4524. https://doi.org/10.1029/2001GL013684

Richards, P. G. (1991). An improved algorithm for determining neutral winds from the height of the F2 peak electron density. *Journal of Geophysical Research*, *96*(A10), 17839–17846. https://doi.org/10.1029/91JA01467

Richards, P. G. (2001). Seasonal and solar cycle variations of the ionospheric peak electron density: Comparison of measurement and models. *Journal of Geophysical Research*, *106*(A7), 12803–12809. https://doi.org/10.1029/2000JA000365

Richards, P. G. (2002). Ion and neutral density variations during ionospheric storms in September 1974: Comparison of measurement and models. *Journal of Geophysical Research*, *107*(A11), 1361. https://doi.org/10.1029/2002JA009278

Richards, P. G. (2004). On the increases in nitric oxide density at midlatitudes during ionospheric storms. *Journal of Geophysical Research*, *109*(A6), A06304. https://doi.org/10.1029/2003JA010110

Richards, P. G., Bilitza, D., & Voglozin, D. (2010). Ion density calculator (IDC): A new efficient model of ionospheric ion densities. *Radio Science*, *45*(5), RS5007. https://doi.org/10.1029/2009RS004332

Richards, P. G., Fennelly, J. A., & Torr, D. G. (1994). EUVAC: A solar EUV flux model for aeronomic calculations. *Journal of Geophysical Research*, *99*(A5), 8981. https://doi.org/10.1029/94JA00518

Richards, P. G., & Torr, D. G. (1983). A simple theoretical model for calculating and parameterizing the ionospheric photoelectron flux. *Journal of Geophysical Research*, *88*(A3), 2155. https://doi.org/10.1029/JA088iA03p02155

Rishbeth, H., & Garriott, O. (1969). *Introduction to ionospheric physics*. *International geophysics series* (Vol. 14). Academic Press.

Rush, M. C., Fox, M., Bilitza, D., Davies, K., McNamara, L., Stewart, F. G., & PoKempner, M. (1989). Ionospheric mapping – An update of foF2 coefficients. *Telecommunication Journal*, *56*, 179–182.

Rush, M. C., PoKempner, M., Anderson, D. N., Perry, J., Steward, F. G., & Reasoner, R. (1984). Maps of foF2 derived from observations and theoretical data. *Radio Science*, *19*(4), 1083–1097. https://doi.org/10.1029/RS019i004p01083

Rush, M. C., PoKempner, M., Anderson, D. N., Steward, F. G., & Perry, J. (1983). Improving ionospheric maps using theoretically derived values of foF2. *Radio Science*, *18*(1), 95–107. https://doi.org/10.1029/RS018i001p00095

Rycroft, M. J., & Jones, J. R. (1987). A suggested model for the IRI plasmaspheric distribution. *Advances in Space Research*, *7*(6), 13–22. https://doi.org/10.1016/0273-1177(87)90266-3

Scherliess, L., & Fejer, B. (1999). Radar and satellite global equatorial F region vertical drift model. *Journal of Geophysical Research*, *104*(A4), 6829–6842. https://doi.org/10.1029/1999JA900025

Scherliess, L., Thompson, D. C., & Schunk, R. W. (2008). Longitudinal variability of low-latitude total electron content: Tidal influences. *Journal of Geophysical Research*, *113*(A1), A01311. https://doi.org/10.1029/2007JA012480

Schmidt, M., Bilitza, D., Shum, C. K., & Zeilhofer, C. (2008). Regional 4-D modeling of the ionospheric electron density. *Advances in Space Research*, *42*(4), 782–790. https://doi.org/10.1016/j.asr.2007.02.050

Schunk, R., & Nagy, A. (2009). *Ionospheres: Physics, plasma physics, and chemistry*. *Cambridge Atmospheric and Space Science Series* (2nd ed.). Cambridge University Press. https://doi.org/10.1017/CBO9780511635342

Scotto, C., Mosert de Gonzalez, M., Radicella, S. M., & Zolesi, B. (1997). On the prediction of F1 ledge and critical frequency. *Advances in Space Research*, *20*(9), 1773–1775. https://doi.org/10.1016/S0273-1177(97)00589-9

Scotto, C., Radicella, S. M., & Zolesi, B. (1998). An improved probability function to predict the F1 layer occurrence and L condition. *Radio Science*, *33*(6), 1763–1765. https://doi.org/10.1029/98RS02637

Serafimov, K. B., Serafimova, M. K., Ramanamurty, Y. V., & Rawer, K. (1985). A note on the use of absorption measurements for improving the IRI electron density distribution in the lower ionosphere. *Advances in Space Research*, *5*(10), 99–102. https://doi.org/10.1016/0273-1177(85)90189-9

Sethi, N. K., Dabas, R. S., Bhawre, P., & Sarkar, S. K. (2009). Bottomside profile shape parameters during low solar activity and comparison with IRI-2007 model. *Journal of Atmospheric and Solar-Terrestrial Physics*, *71*(17–18), 1935–1942. https://doi.org/10.1016/j.jastp.2009.08.003

Shaikh, M. M., Nava, B., & Haralambous, H. (2018). On the use of topside RO-derived electron density for model validation. *Journal of Geophysical Research: Space Physics*, *123*(5), 3943–3954. https://doi.org/10.1029/2017JA025132

Sheik, N. M., Neske, E., Rawer, K., & Rebstock, C. (1978). Comparison of peak electron densities of the F2—Layer derived from in situ measurements with CCIR predictions. *Telecommunication Journal*, *45*, 225–227.

Shi, J. K., Wang, G. J., Reinisch, B. W., Shang, S. P., Wang, X., Zherebotsov, G., & Potekhin, A. (2011). Relationship between strong range spread F and ionospheric scintillations observed in Hainan from 2003 to 2007. *Journal of Geophysical Research*, *116*(A8). https://doi.org/10.1029/2011JA016806

Shim, J. S., Kuznetsova, M., Rastätter, L., Hesse, M., Bilitza, D., Butala, M., et al. (2012). CEDAR Electrodynamics Thermosphere Ionosphere (ETI) Challenge for systematic assessment of ionosphere/thermosphere models: Electron density, neutral density, NmF2, and hmF2 using space based observations. *Space Weather*, *10*(10), S10004. https://doi.org/10.1029/2012SW000851

Shim, J. S., Kuznetsova, M., Rastätter, L., Hesse, M., Bilitza, D., Codrescu, M., et al. (2011). CEDAR electrodynamics thermosphere ionosphere 1 (ETI) challenge for systematic assessment of ionosphere/thermosphere models 1: NmF2, hmF2, and vertical drift using ground based observations. *Space Weather*, *9*(12), S12003. https://doi.org/10.1029/2011SW000727

Shim, J. S., Rastätter, L., Kuznetsova, M., Bilitza, D., Codrescu, M., Coster, A. J., et al. (2017). CEDAR-GEM challenge for systematic assessment of ionosphere/thermosphere models in predicting TEC during the 2006 December storm event. *Space Weather*, *15*(10), 1238–1256. https://doi.org/10.1002/2017SW001649

Shim, J. S., Tsagouri, I., Goncharenko, L., Rastaetter, L., Kuznetsova, M., Bilitza, D., et al. (2018). Validation of ionospheric specifications during geomagnetic storms: TEC and foF2 during the 2013 March storm event. *Space Weather*, *16*(11), 1686–1701. https://doi.org/10.1029/2018SW002034

Shimazaki, T. (1955). World-wide daily variations in the height of the electron density of the ionospheric F2-layer. *Journal of the Radio Research Laboratories*, *2*, 85–97.

Shubin, V. N. (2015). Global median model of the F2-layer peak height based on ionospheric radio-occultation and ground based Digisonde observations. *Advances in Space Research*, *56*(5), 916–928. https://doi.org/10.1016/j.asr.2015.05.029

Shubin, V. N., & Deminov, M. G. (2019). Global dynamic model of critical frequency of the ionospheric F2 layer. *Geomagnetism and Aeronomy*, *59*(4), 429–440. https://doi.org/10.1134/S0016793219040157

Shubin, V. N., Karpachev, A. T., & Tsybulya, K. G. (2013). Global model of the F2 layer peak height for low solar activity based on GPS radio occultation data. *Journal of Atmospheric and Solar-Terrestrial Physics*, *104*, 106–115. https://doi.org/10.1016/j.jastp.2013.08.024

Siebert, M., & Meyer, J. (1996). Geomagnetic activity indices. In W. Dieminger, G. K. Hartman, & R. Leitinger (Eds.), *The upper atmosphere* (pp. 887–911). Springer.

Singer, W., Bremer, J., & Taubenheim, J. (1984). Improvement of the solar-cycle variation of IRI lower ionosphere models by means of radio wave propagation data. *Advances in Space Research*, *4*(l), 79–88. https://doi.org/10.1016/0273-1177(84)90476-9

Siskind, D. E., Zawdie, K. A., Sassi, F., Drob, D. P., & Friedrich, M. (2018). An intercomparison of VLF and sounding rocket techniques for measuring the daytime *D* region ionosphere: Theoretical implications. *Journal of Geophysical Research: Space Physics*, *123*(10), 8688–8697. https://doi.org/10.1029/2018JA025807

Smirnova, N. V., & Danilov, A. D. (1994). Rocket data on the D-region positive ion composition. *Journal of Atmospheric and Terrestrial Physics*, *56*(8), 887–892. https://doi.org/10.1016/0021-9169(94)90150-3

Smith, E. K. (1976). *World maps of sporadic E (foEs > 7 MHz) for use in prediction of VHF oblique-incidence propagation*. OT Special Publication 76-10, United States Department of Commerce, Office of Telecommunications.

Solomon, S. C., Woods, T. N., Didkovsky, L. V., Emmert, J. T., & Qian, L. (2010). Anomalously low solar extreme-ultraviolet irradiance and thermospheric density during solar minimum. *Geophysical Research Letters*, *37*(16), L16103. https://doi.org/10.1029/2010GL044468

Spenner, K., & Plugge, R. (1979). Empirical model of global electron temperature distribution between 300 and 700 km based on data from AEROS-A. *Journal of Geophysics*, *46*(1), 43–56.

Spiro, R. W., Reiff, P. H., & Maher, L. J., Jr. (1982). Precipitating electron energy flux and auroral zone conductances - An empirical model. *Journal of Geophysical Research*, *87*(A10), 8215–8227. https://doi.org/10.1029/JA087iA10p08215

Ssessanga, N., Kim, Y. H., Kim, E., & Kim, J. (2015). Regional optimization of the IRI-2012 output (TEC, foF2) by using derived GPS-TEC. *Journal of the Korean Physical Society*, *66*(10), 1599–1610. https://doi.org/10.3938/jkps.66.1599

Stolle, C., Liu, H., Truhlik, V., Lühr, H., & Richards, P. G. (2011). Solar flux variation of the electron temperature morning overshoot in the equatorial F region. *Journal of Geophysical Research*, *116*(A4), A04308. https://doi.org/10.1029/2010JA016235

Stolle, C., Lühr, H., & Fejer, B. G. (2008). Relation between the occurrence rate of ESF and the equatorial vertical plasma drift velocity at sunset derived from global observations. *Annales Geophysicae*, *26*(12), 3979–3988. https://doi.org/10.5194/angeo-26-3979-2008

Strickland, D. J., Bishop, J., Evans, J. S., Majeed, T., Shen, P. M., Cox, R. J., et al. (1999). Atmospheric ultraviolet radiance integrated code (AURIC): Theory, software architecture, inputs, and selected results. *Journal of Quantitative Spectroscopy & Radiative Transfer*, *62*(6), 689–742. https://doi.org/10.1016/S0022-4073(98)00098-3

Szuszczewicz, E. P., Wilkinson, P., Swider, W., Pulinets, S., Abdu, M. A., Roelof, E., et al. (1993). Measurements and empirical model comparisons of F-region characteristics and auroral boundaries during the solstitial SUNDIAL campaign of 1987. *Annales Geophysicae*, *11*, 601–613.

Tapping, K. F. (2013). The 10.7 cm solar radio flux (F10.7). *Space Weather*, *11*(7), 394–406. https://doi.org/10.1002/swe.20064

Tariku, Y. A. (2019). Mid latitude ionospheric TEC modeling and the IRI model validation during the recent high solar activity (2013–2015). *Advances in Space Research*, *63*(12), 4025–4038. https://doi.org/10.1016/j.asr.2019.03.010

Thammavongsy, P., Supnithi, P., Phakphisut, W., Hozumi, K., & Tsugawa, T. (2020). Spread-F prediction model for the equatorial Chumphon station, Thailand. *Advances in Space Research*, *65*(1), 152–162. https://doi.org/10.1016/j.asr.2019.09.040

Themens, D. R., & Jayachandran, P. T. (2016). Solar activity variability in the IRI at high latitudes: Comparisons with GPS total electron content. *Journal of Geophysical Research: Space Physics*, *121*(4), 3793–3807. https://doi.org/10.1002/2016JA022664

Themens, D. R., Jayachandran, P. T., Bilitza, D., Erickson, P. J., Häggström, I., Lyashenko, M. V., et al. (2018). Topside electron density representations for middle and high latitudes: A topside parameterization for E-CHAIM based on the NeQuick. *Journal of Geophysical Research: Space Physics*, *123*(2), 1603–1617. https://doi.org/10.1002/2017JA024817

Themens, D. R., Jayachandran, P. T., Galkin, I., & Hall, C. (2017). The empirical Canadian high arctic ionospheric model (E-CHAIM): NmF2 and hmF2. *Journal of Geophysical Research: Space Physics*, *122*(8), 9015–9031. https://doi.org/10.1002/2017JA024398

Themens, D. R., Jayachandran, P. T., McCaffrey, A. M., Reid, B., & Varney, R. H. (2019). A bottomside parameterization for the Empirical Canadian High Arctic Ionospheric Model. *Radio Science*, *54*(5), 397–414. https://doi.org/10.1029/2018RS006748

Themens, D. R., Jayachandran, P. T., Nicolls, M. J., & MacDougall, J. W. (2014). A top to bottom evaluation of IRI 2007 within the polar cap. *Journal of Geophysical Research: Space Physics*, *119*(8), 6689–6703. https://doi.org/10.1002/2014JA020052

Themens, D. R., Reid, B., Jayachandran, P. T., Larson, B., Koustov, A. V., Elvidge, S., et al. (2021). E-CHAIM as a model of total electron content: Performance and diagnostics. *Space Weather*, *19*(11), e2021SW002872. https://doi.org/10.1029/2021SW002872

Tikhonov, A. N., & Arsenin, V. Y. (1977). *Solutions of ill-posed problems*. John Wiley.

Titheridge, J. E. (1990). Aeronomical calculations of valley size in the ionosphere. *Advances in Space Research*, *10*(8), 21–24. https://doi.org/10.1016/0273-1177(90)90180-8

Titheridge, J. E. (2000). Modelling the peak of the ionospheric E-layer. *Journal of Atmospheric and Solar-Terrestrial Physics*, *62*(2), 93–114. https://doi.org/10.1016/S1364-6826(99)00102-9

Torkar, K. M., & Friedrich, M. (1983). Tests of an ion-chemical model of the D and lower E region. *Journal of Atmospheric and Terrestrial Physics*, *45*(6), 369–385. https://doi.org/10.1016/S0021-9169(83)81097-6

Třísková, L., Truhlik, V., & Šmilauer, J. (2002). On possible improvements of outer ionosphere ion composition model in IRI. *Advances in Space Research*, *29*(6), 849–858. https://doi.org/10.1016/S0273-1177(02)00041-8

Třísková, L., Truhlik, V., & Šmilauer, J. (2003). An empirical model of ion composition in the outer ionosphere. *Advances in Space Research*, *31*(3), 653–663. https://doi.org/10.1016/S0273-1177(03)00040-1

Truhlik, V., Bilitza, D., Kotov, D., Shulha, M., & Třísková, L. (2021). A global empirical model of the ion temperature in the ionosphere for the international reference ionosphere. *Atmosphere*, *12*(8), 1081. https://doi.org/10.3390/atmos12081081

Truhlik, V., Bilitza, D., & Třísková, L. (2009). Latitudinal variation of the topside electron temperature at different levels of solar activity. *Advances in Space Research*, *44*(6), 693–700. https://doi.org/10.1016/j.asr.2009.04.029

Truhlik, V., Bilitza, D., & Třísková, L. (2012). A new global empirical model of the electron temperature with inclusion of the solar activity variations for IRI. *Earth Planets and Space*, *64*(6), 531–543. https://doi.org/10.5047/eps.2011.10.016

Truhlik, V., Bilitza, D., & Třisková, L. (2015). Towards better description of solar activity variations in IRI ion composition model. *Advances in Space Research*, *55*(8), 2099–2105. https://doi.org/10.1016/j.asr.2014.07.033

Truhlik, V., Třísková, L., & Smilauer, J. (2001). Improved electron temperature model and comparison with satellite data. *Advances in Space Research*, *27*(1), 101–109. https://doi.org/10.1016/S0273-1177(00)00144-7

Truhlik, V., Třísková, L., & Smilauer, J. (2003). Response of outer ionosphere electron temperature and density to changes in solar activity. *Advances in Space Research*, *31*(3), 697–700. https://doi.org/10.1016/S0273-1177(03)00045-0

Truhlik, V., Třísková, L., Smilauer, J., & Afonin, V. (2000). Global empirical models of electron temperatures in the outer ionosphere for period of high solar activity based on data of three Intercosmos satellites. *Advances in Space Research*, *25*(1), 163–172. https://doi.org/10.1016/S0273-1177(99)00914-X

Wallis, D. D., & Budzinski, E. E. (1981). Empirical models of height integrated conductivities. *Journal of Geophysical Research*, *86*(A1), 125–137. https://doi.org/10.1029/JA086iA01p00125

Wang, S., Huang, S., Fang, H., & Wang, Y. (2016). Evaluation and correction of the IRI2016 topside ionospheric electron density model. *Advances in Space Research*, *58*(7), 1229–1241. https://doi.org/10.1016/j.asr.2016.06.020

Wenjing, L., Limberger, M., Schmidt, M., Dettmering, D., Hugentobler, U., Bilitza, D., et al. (2015). Regional modeling of ionospheric peak parameters using GNSS data: An update for IRI. *Advances in Space Research*, *55*(8), 1981–1993. https://doi.org/10.1016/j.asr.2014.12.006

Wu, X., Hu, H., Gong, X., Zhang, X., & Wang, X. (2009). Analysis of inversion errors of ionospheric radio occultation. *GPS Solutions*, *13*(3), 231–239. https://doi.org/10.1007/s10291-008-0116-x

Xu, W., Marshall, R. A., Bortnik, J., & Bonnell, J. W. (2021). An electron density model of the D- and E-region ionosphere for transionospheric VLF propagation. *Journal of Geophysical Research: Space Physics*, *126*(7), e2021JA029288. https://doi.org/10.1029/2021JA029288

Yang, T.-Y., Park, J., Kwak, Y.-S., Oyama, K.-I., Minow, J. I., & Lee, J.-J. (2020). Morning overshoot of electron temperature as observed by the Swarm constellation and the International Space Station. *Journal of Geophysical Research: Space Physics*, *125*(2), e2019JA027299. https://doi.org/10.1029/2019JA027299

Yue, X., Schreiner, W. S., Kuo, Y.-H., Hunt, D. C., Wang, W., Solomon, S. C., et al. (2012). Global 3-D ionospheric electron density reanalysis based on multi-source data assimilation. *Journal of Geophysical Research*, *117*(A9), A09325. https://doi.org/10.1029/2012JA017968

Yue, X., Schreiner, W. S., Lei, J., Sokolovskiy, S. V., Rocken, C., Hunt, D. C., & Kuo, Y.-H. (2010). Error analysis of Abel retrieved electron density profiles from radio occultation measurements. *Annales Geophysicae*, *28*(1), 217–222. https://doi.org/10.5194/angeo-28-217-2010

Zhang, M.-L., Liu, C., Wan, W., Liu, L., & Ning, B. (2009). A global model of the ionospheric F2 peak height based on EOF analysis. *Annales Geophysicae*, *27*(8), 3203–3212. https://doi.org/10.5194/angeo-27-3203-2009

Zhang, M.-L., Wan, W., Liu, L., & Shi, J. K. (2008). Variability of the behavior of the bottomside (B0, B1) parameters obtained from the ground-based ionograms at China's low latitude station. *Advances in Space Research*, *42*(4), 695–702. https://doi.org/10.1016/j.asr.2007.07.022

Zhang, S.-R., Holt, J. M., van Eyken, A. P., McCready, M., Amory-Mazaudier, C., Fukao, S., & Sulzer, M. (2005). Ionospheric local model and climatology from long-term databases of multiple incoherent scatter radars. *Geophysical Research Letters*, *32*(20), L20102. https://doi.org/10.1029/2005GL023603

Zhang, Y., & Paxton, L. J. (2008). An empirical Kp-dependent global auroral model based on TIMED/GUVI data. *Journal of Atmospheric and Solar-Terrestrial Physics*, *70*(8–9), 1231–1242. https://doi.org/10.1016/j.jastp.2008.03.008

Zhang, Y., Paxton, L. J., Bilitza, D., & Doe, R. (2010). Near real-time assimilation of auroral peak E-region density and equatorward boundary in IRI. *Advances in Space Research*, *46*(8), 1055–1063. https://doi.org/10.1016/j.asr.2010.06.029

Zhelavskaya, I. S., Shprits, Y. Y., & Spasojevic, M. (2017). Empirical modeling of the plasmasphere dynamics using neural networks. *Journal of Geophysical Research: Space Physics*, *122*(11), 11227–11244. https://doi.org/10.1002/2017JA024406

Zolesi, B., & Cander, L. (2014). *Ionospheric prediction and forecasting*. Springer.